University of Alberta

PLUMES IN STRATIFIED ENVIRONMENTS

by

Joseph Kojo Ansong

A thesis submitted to the Faculty of Graduate Studies and Research
in partial fulfillment of the requirements for the degree of
Doctor of Philosophy

in

Applied Mathematics

Department of Mathematical and Statistical Sciences

Fall 2009
Edmonton, Alberta

Examining Committee

Prof. Bruce R. Sutherland, Physics and of Earth and Atmospheric Sciences

Prof. Bryant Moodie, Mathematical and Statistical Sciences

Prof. Gerhard Reuter, Earth and Atmospheric Sciences

Prof. Paul Myers, Earth and Atmospheric Sciences

Prof. Richard Craster, Mathematical and Statistical Sciences

Prof. Colm-Cille P. Caulfield, Mathematics, University of Cambridge

To the memory of my father, John Kwesi Ansong, and my son, Simon Ansong.

Also dedicated to my mother, Akua Ansong, my lovely wife, Christiana Ansong, and our newly arrived baby boy, Isaac Ansong.

ABSTRACT

This research presents the results of two interrelated sets of experiments examining the dynamics of plumes and fountains in two-layer and continuously stratified environments.

The first study examines the evolution of an axisymmetric turbulent fountain in a two-layer stratified environment. Interacting with the interface, the fountain is observed to exhibit three regimes of flow. It may penetrate the interface but nonetheless return to the source where it spreads as a radially propagating gravity current; the return flow may be trapped at the interface where it spreads as a radially propagating intrusion or it may do both. These regimes have been classified using empirically determined regime parameters which govern the relative initial momentum of the fountain and the relative density difference of the fountain and the ambient fluid. The maximum vertical distance travelled by the fountain in a two-layer fluid has been theoretically determined by extending the theory developed for fountains in a homogeneous environment. The theory compares favourably with experimental measurements. We have also developed a theory to analyse the initial speeds of the resulting radial currents. We found that the currents exhibited two different regimes of flow.

The second study presents experimental results of the generation of internal gravity waves by a turbulent buoyant plume impinging upon the interface between a uniform density layer of fluid and a linearly stratified layer. The wave field is observed and its properties measured non-intrusively using axisymmetric Schlieren. In particular, we determine the fraction of the energy flux

associated with the plume at the neutral buoyancy level that is extracted by the waves. On average, this was found to be approximately 4 per cent. Within the limits of the experimental parameters, the maximum vertical displacement amplitude of waves were found to depend linearly upon the maximum penetration height of the plume beyond the neutral level. The frequency of the waves was found to lie in a narrow range relative to the buoyancy frequency. The results are used to interpret the generation of waves in the atmosphere by convective storms impinging upon the tropopause via the mechanical oscillator effect.

If we must be burdened for many more years with obnoxious effluents, while we fight to rid our civilization of them let us be philosophical. To the town sparrow Nature consists of houses, trees, houses, trees: let us think of it as chimneys, streets, chimneys, streets; and from time to time forget the bronchitis and rotting of curtains by pollution, and think while we can of the delightful mechanisms of dispersion employed by Nature. In perhaps another generation plumes will be invisible, but with their radioactivity possibly as dangerous as our smoke.

R.S. SCORER

If only you had paid attention to my commands, your peace would have been like a river, your righteousness like the waves of the sea.

Isaiah 48:18

ACKNOWLEDGEMENT

I would like to extend my sincere gratitude to my supervisor, Professor Bruce R. Sutherland, for his encouragement, patience, advice and constant support during these years of my research. Bruce has been extremely helpful when the going gets tough and he was always unfazed by the obstacles that came along. This research would not have been possible without his enormous intellectual contribution and intuitive thought.

I would also like to express my thanks to Professor Colm P. Caulfield for reading the manuscript and making valuable suggestions concerning additions to the thesis and about technical definitions. I am also grateful to all the members of my committee (Prof. Bryant Moodie, Prof. Gerhard Reuter, Prof. Paul Myers and Prof. Richard Craster) for reviewing the draft of this thesis and providing good comments.

I am grateful to all my colleagues in Bruce's group for their friendship, support and positive criticisms. Thanks to James Munroe, Heather Clark, Hayley Dossier, Kate Gregory, Amber Holdsworth, Justine McMillan, Joshua Nault and Geoff Brown. I've enjoyed shearing an office with James in the physics department and he has been very helpful with his programming skills. I've also enjoyed the friendship of Matthew Emmett as my office mate in the mathematics department. Thanks Matt.

My parents have always supported and encouraged me in my travels away from home in search of knowledge and experience in other parts of the world. I am grateful to them. Though my son and my dad passed away in the course of this research, they will always occupy a special place in my heart. I am indebted to my wife, Christy, for putting up with my constant travels away from home. I am grateful for her support.

Above all, I'm grateful to my Lord and saviour Jesus Christ for his guidance, divine protection and for keeping me healthy all these years. To him be the glory forever and ever; Amen!!

Table of Contents

List of Tables

List of Figures

List of Symbols

Chapter 1

Introduction and motivation

Jets and plumes fall under a class of flows termed as free boundary flows and refer to continuous flows from a localized source which occupy a narrow region of their environment. They are said to be "free" because the flow is not confined by surfaces but is free to spread into and also mix with fluid from the ambient. Such flows are prevalent in life and in nature; examples include smoke rising from a chimney or a cigarette, plumes from a volcanic eruption and effluent released into a water body such as a lake or ocean. They are classified according to their source parameters, the geometry of the source as well as their environmental condition. They are further classified based upon the presence or absence of buoyancy at the source, the Reynolds number of the flow, the strength of the fluxes at the source, the sign of the initial buoyancy flux and the dynamics of the ambient fluid. Figure 1.1 shows a simple illustration of some of these classifications with emphasis on the class of flows related to this study. For instance both laminar and turbulent plumes could have plane or axisymmetric sources but in figure 1.1 only turbulent plumes are further classified since we focus on turbulent plumes in this study. In the following we give a brief description of each class of flow together with a brief review of the literature associated with that class.

1.1 Classification of jets and plumes

Jets

Jets are a type of free boundary flows in which the flow is purely driven by a continuous localized source of momentum from a fluid of one density to another of the same density. Thus, there is no density difference between the jet fluid and the environment fluid. An example includes the injection of fresh water through a pipe into an extensive body of fresh water. Experiments show that above a Reynolds number of about 2000, jets are turbulent (Fischer *et al.* (1979); Lee & Chu (2003)). The Reynolds number is defined by $R_e = w_0 D/\nu$ with w_0 and D the source velocity and diameter, respectively, and ν is the kinematic viscosity of the fluid.

Detailed experiments on turbulent jets were carried out by Albertson *et al.* (1950), initial studies on laminar jets was undertaken by Schlichting (1968) while Mollendorf & Gebhart (1973) considered the effect of adding buoyancy to axisymmetric laminar jets. One of the detailed theoretical studies of plane and axisymmetric turbulent jets can be found in Rajaratnam (1976).

Thermals

Thermals are a class of buoyant flows which result when there is an instantaneous release of a buoyant element from a localized source. After release the buoyant element becomes detached from the source and freely moves upward or downward as a blob of fluid under the action of buoyancy forces. Theoretical and experimental studies on thermals have been undertaken by Morton *et al.* (1956), Scorer (1957, 1959), Caulfield & Woods (1998); Lee & Chu (2003).

Plumes

Plumes arise as a result of the continuous release of buoyancy from a localized source generating a flow driven by the density differences between the plume and the ambient fluids. They are further classified as laminar or turbulent. In

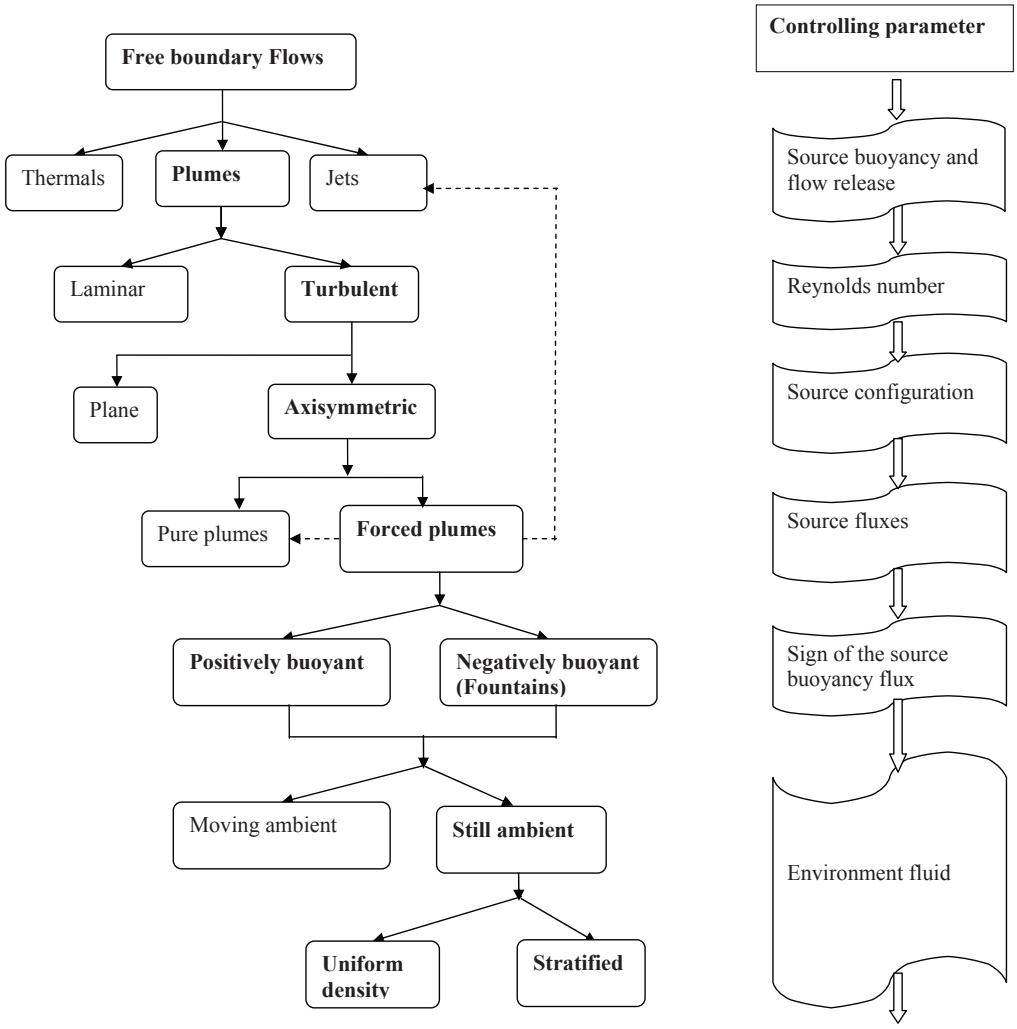

Figure 1.1: Schematic classification of some free boundary flows. The dashed arrow is used to show that jets and pure plumes are special cases of forced plumes. The parameter determining the class of flow is described on the right.

a laminar plume (occurring at low Reynolds numbers), rising heated air from a concentrated source of energy imparts heat to the surrounding fluid through diffusion thereby causing the ambient fluid to rise (Gebhart (1961); Linden (2000)). In a turbulent plume, the fluid in the environment mixes with the plume fluid through the process of entrainment. In either case, some of the ambient fluid becomes part of the plume fluid resulting in an increase in the volume of the plume fluid as it rises. For a plume coming from a point source, the continuous increase in the volume of fluid causes the plume to assume a conical shape.

Laminar plumes have been studied by several investigators. At some distance from a point or line source, all laminar plumes become unstable and subsequently become turbulent. Some of the most comprehensive theoretical and experimental studies on laminar plumes are by Gebhart *et al.* (1970) and Mollendorf & Gebhart (1973). They first simplify the conservation equations of mass, momentum and energy using the boundary layer and Boussinesq approximations. The governing partial differential equations are further transformed into ordinary differential equations using appropriately defined similarity variables and stream functions. They then obtain boundary conditions for the system of equations based on physical considerations and solve the problem numerically as a boundary value problem for different values of the Prantdl number which appears as an unknown parameter in the equations. Gebhart & Pera (1971) have extended this approach to cover the case of laminar plumes arising from the effects of both thermal and mass diffusion. Detailed analyses may be found in Gebhart (1961).

The transition from laminar to turbulent flow has been discussed by Jaluria (1980) (Chapter 8). Most practical flows are turbulent in nature and so have received greater attention in the literature. A review of some of the literature on turbulent plumes is given in Section 1.2.

Plumes can further be categorized based upon the configuration of the source. The source could be a line in which case the plume is referred to as a plane or a line plume or it could be round and the plume is said to be an ax-

isymmetric or a round plume. An example of a plane plume is air rising from a heated long horizontal wire while a classic example of an axisymmetric plume is smoke rising from a cigarette. Far away from the source line plumes become round in nature and so axisymmetric plumes have consequently received greater attention in the literature.

Forced plumes

Plumes coming from a source with an excess of momentum flux are referred to as forced plumes (Morton (1959*a*); Hunt & Kaye (2001, 2005)) or buoyant jets (Rodi (1982)). Plumes with non-zero values of the source volume flux (Q_0), momentum flux (M_0) and buoyancy flux (F_0) can be classified based upon the source parameter (Morton (1959*a*); Hunt & Kaye (2001, 2005))

$$\Gamma_0 = \frac{5Q_0^2F_0}{4\alpha\pi^{1/2}M_0^{5/2}},$$

where α is the entrainment coefficient (also see equation 2.84). Plumes are called pure plumes when the momentum and volume fluxes are in balance such that $\Gamma_0 = 1$. Lazy plumes arise from a source with a deficit of momentum flux compared to a pure plume with the same source buoyancy and volume fluxes such that $\Gamma_0 > 1$. The plume is forced if $\Gamma_0 < 1$. In the case where the initial momentum and buoyancy fluxes are in the same direction (with buoyancy aiding the flow), the plume is referred to as a positively buoyant plume. The plume in this case is initially dominated by the source momentum while buoyancy forces dominate at a distance far from the source. An example includes the continuous jet of smoke rising from a chimney. If the initial momentum and buoyancy fluxes are in opposite direction (with buoyancy opposing the flow), the plume is called a negatively buoyant plume or a fountain. Water fountains are typical examples of this category.

In all cases discussed above, the fluid in the environment could be still or moving at some horizontal speed. The ambient fluid could also have a uniform density or it could be stably stratified. If the fluid in the environment

is moving at a uniform horizontal speed, the plume in such an environment will be curved toward the direction as the mean flow. These are referred to as bent-over plumes (Turner (1973)) or plumes in a co-flow (Lee & Chu (2003)).

1.2 Turbulent plumes: Literature review

Studies on turbulent buoyant plumes in a uniform environment were first carried out by Zeldovich (1937) and Schmidt (1941) (see Morton *et al.* (1956)). Rouse *et al.* (1952) did an analytical and experimental study of both plane and axisymmetric turbulent plumes and obtained explicit expressions for the change in the vertical velocity and density with height. The experiments were conducted using heat sources consisting of gas burners and measurements were taken of the radial spread in vertical velocity and density at each height. Their results indicated a Gaussian distribution of these flow quantities and constitute one of the benchmark results for comparison with other theoretical and experimental studies of turbulent plumes (Turner (1973)). They observed that even though the plumes were produced with a heat source, essentially the same flow pattern can be produced in liquid instead of a gas since it is the gravitational rather than the thermal aspects of the flow which are fundamental to the phenomenon. Their theoretical analysis employed the idea of turbulent diffusion instead of turbulent entrainment.

Priestley & Ball (1955) presented a theoretical model of round turbulent plumes in both uniform and linearly stratified environments. Their model was based on the integrated forms of the conservation equations of kinetic energy, vertical momentum and heat. They employed a closure assumption in which the covariance of the velocity fluctuations depended on the square of the mean velocity.

Morton *et al.* (1956) conducted theoretical and experimental studies of turbulent plane and axisymmetric pure plumes as well as thermals in uniform and stably stratified environments. Their model was based on the integrated forms of the conservation equations of mass, vertical momentum and heat.

They introduced the assumption of turbulent entrainment of the ambient fluid into the plume in order to close the system of equations. This assumption is referred to as the entrainment hypothesis and will be discussed in Chapter 2. In their laboratory experiments the plumes were generated using liquid instead of gas. Salt solution was injected into an ambient of fresh water to study the evolution of the plumes in uniform environments.

A detailed theoretical analyses of the similarities and differences between the models of Priestley & Ball (1955) and Morton *et al.* (1956) have been presented in Morton (1971). This showed that the use of the flux equations for kinetic energy and vertical momentum is not equivalent to the use of flux equations for vertical momentum and mass and that the latter is preferable.

Following the study by Morton *et al.* (1956) on pure plumes, Morton (1959*b*) presented an elegant theoretical study of forced plumes in uniform and stably stratified environments in which pure plumes and jets were obtained as special cases (also see Morton (1959*a*); Morton & Middleton (1973)). Morton (1959*b*) showed that this general case of a turbulent plume from a source of finite size with both momentum and buoyancy can be related to the flow from a virtual point source of buoyancy and momentum only. The entrainment hypothesis was employed to solve different cases of positively buoyant plumes and fountains.

An alternative approach for solving the problem of turbulent forced plumes was presented by Abraham (1963). He employed the spreading assumption in which the plume is assumed to widen at a prescribed rate. The use of a constant entrainment coefficient by Morton (1959*b*) to model the whole region of the upward flow of a fountain was criticized by Abraham (1963) since this resulted in an infinite width of the fountain at the maximum height. The comparison of the theory of Abraham (1963) to those of previous models is discussed in Section 2.4.

All previous theoretical developments of turbulent plumes mentioned above considered the case of Boussinesq plumes in which the density difference between the plume fluid and the ambient was considered small. Crapper &

Baines (1977, 1978) and Rooney & Linden (1996) have examined the case of non-Boussinesq forced plumes. In particular, Crapper & Baines (1977) suggested that $|\Delta\rho|/\rho_a \approx 0.05$ should be the upper bound of applicability of the Boussinesq approximation, where $\Delta\rho$ is the density difference between the plume and the ambient and ρ_a is the ambient density. Rooney & Linden (1996) found that for a non-Boussinesq plume it is the flux of weight deficiency that is conserved with height in an unstratified fluid and not the buoyancy flux (also see Linden (2000), page 309).

Previous treatments have also examined only cases in which the source fluxes were steady and the ambient density stratification was linear. Recent developments have examined the case of turbulent plumes in non-uniformly stratified ambients (Caulfield & Woods (1998)) and plumes and jets in which the fluxes at the source are time-dependent (Scase *et al.* (2006*a*,*b*)). A good review of recent theoretical and experimental work on turbulent plumes can be found in Kaye (2008).

1.3 Motivation

Turbulent buoyant plumes in both homogeneous and stably stratified ambient fluids have received considerable attention, in part owing to their environmental impact in such areas as the disposal of sewage in the ocean and in lakes, volcanic eruptions into the atmosphere and emissions from chimneys and flares. The dynamics of plumes and fountains in enclosed spaces have been studied in order to improve the efficiency through which rooms are heated and cooled (Lin & Linden (2005)).

Despite the fact that turbulent buoyant plumes have been studied over the past fifty years, certain aspects of their dynamics are not well understood and form part of the motivation for this study. For example the behaviour of a fountain in a two-layer environment have never been examined. The dynamics of fountains in such an ambient fluid can be used to get a better understanding of the behaviour of pollutants released into the atmosphere in the presence of

atmospheric inversions. Secondly, the internal gravity waves that are generated as a result of the evolution of turbulent plumes in a continuously stratified environment have never been studied. They may be used to study stratospheric waves generated as a result of the vertical development of thunderstorms close to the tropopause. This research examines these aspects of turbulent plumes in stratified environments.

1.3.1 Dispersion of pollutants in the atmosphere

Positive and negatively buoyant plumes have been examined theoretically and experimentally as they evolve in homogeneous and in linearly stratified environments (Priestley & Ball (1955); Morton (1959*b*); Turner (1966); Abraham (1963); Fischer *et al.* (1979); List (1982); Rodi (1982); Bloomfield & Kerr (1998, 2000)). Most of this effort was directed at quantifying the width of the fountain, the initial and final heights (or penetration depths) and the entrainment into the fountain.

Fountains in a two-layer stably stratified environment have received relatively little attention despite their fundamental nature and their potential practical significance. A ventilated room can naturally form a two layer-stratification and it is of interest to know how cold air injected from below mixes in this environment. Jets and fountains in two-layer ambient have also been reported in the situation of refueling compensated fuel tanks on naval vessels (Friedman & Katz (2000)). The thermocline in lakes and oceans and atmospheric inversions can be modelled approximately as the interface of a two-layer fluid (Mellor (1996)), and plumes and fountains can result from the release of effluent into these environments (Rawn *et al.* (1960), Noutsopoulos & Nanou (1986)).

In particular, this research is motivated in part as the first stage of a program to understand the evolution of pollutants from flares that disperse in the presence of an atmospheric inversion. Atmospheric inversions, known for their strong vertical stability, can trap air pollutants below or within them near

ground level and so have adverse effects on human health. Hazardous industrial materials that are released into the atmosphere usually form clouds that are heavier than the atmosphere (Britter (1989)). Both Morton (1959*a*) and Scorer (1959) have applied available mathematical concepts of plume theory to study the dispersion of pollutants in the atmosphere but ignored the effects of an inversion.

1.3.2 Generation of internal gravity waves in the atmosphere

Internal gravity waves have been studied over the years in part because of their effect upon the circulation patterns in the ocean and atmosphere. For example, the momentum transported by convectively generated gravity waves in the tropics have been suggested to drive the quasi-biennial oscillation (Dunkerton (1997)). The waves are also known to affect the global momentum budget in the middle and upper atmosphere as well as in the troposphere through wave drag. Their inclusion in General Circulation Models (GCMs) is necessary for a greater understanding of circulations in the atmosphere and for that matter accurate predictions of global weather patterns (McLandress (1998)). By necessity, GCMs use coarse grids with long time periods and so to include the effects of relatively small and fast internal gravity waves in their models, researchers attempt to parameterize their effects.

Various sources of gravity wave generation have long been identified. These include flow over topography, geostrophic adjustment and deep convection (Fovell *et al.* (1992)). It is now appreciated that the last of these is also significant, particularly in the tropics, but the detailed mechanism for wave generation by convection is not well understood.

Three main ways of generating internal gravity waves by deep convection have been identified in the literature. They include the mechanical oscillator effect (Pierce & Coroniti (1966), Clark *et al.* (1986), Fovell *et al.* (1992)), the obstacle effect (Clark *et al.* (1986)) and the deep heating effect (Alexander &

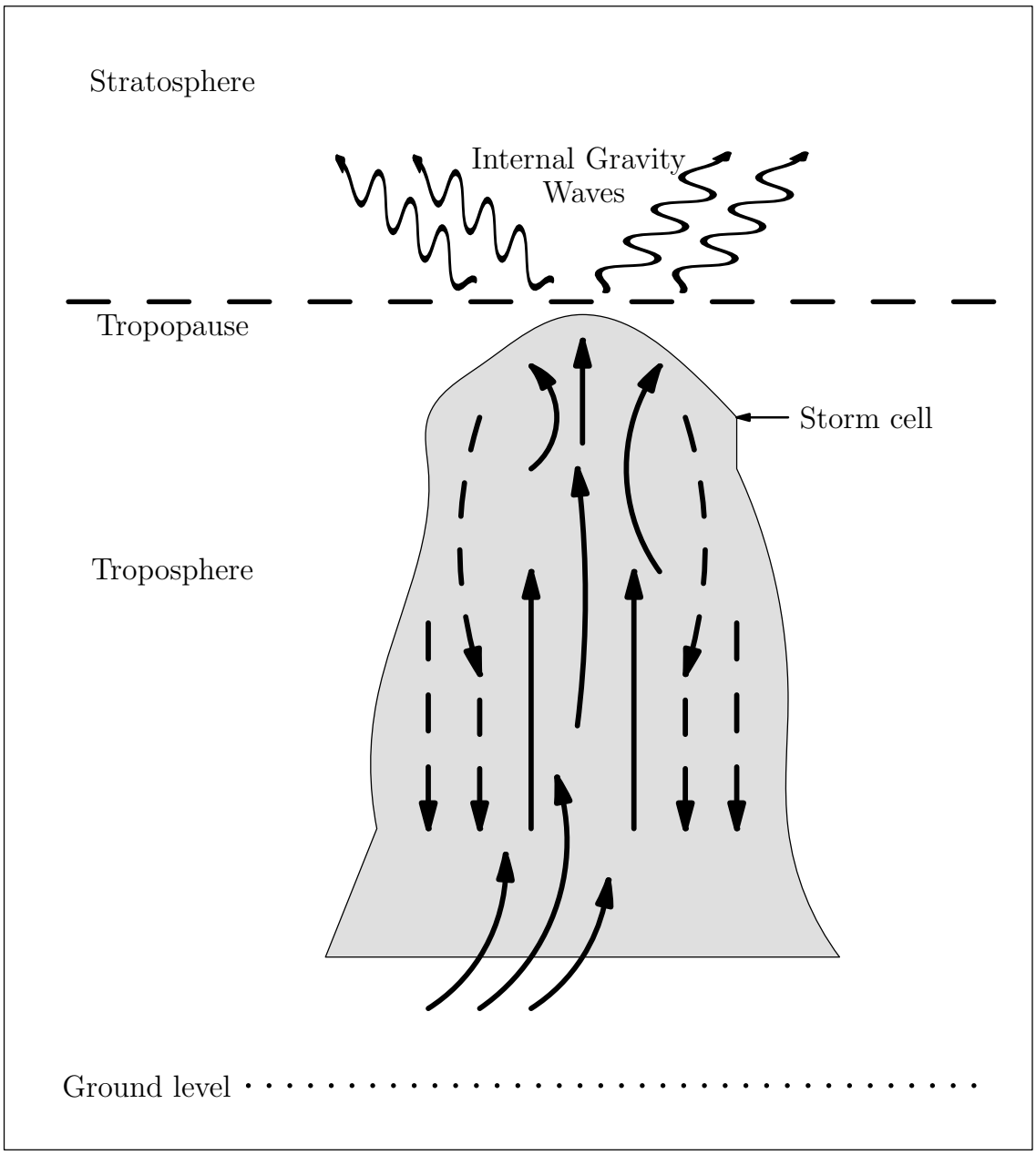

Figure 1.2: Schematic illustration of the mechanical oscillator mechanism in a thunderstorm cell.

Barnet (2007); Pandya & Alexander (1999)). In the mechanical oscillator effect, the vertical oscillations of updrafts and downdrafts are believed to excite internal gravity waves in the stable layer above the troposphere similar to the way in which the waves may be generated by an oscillating rigid body (see figure 1.2). In the obstacle effect, updrafts act as an obstacle to a mean horizontal flow at the cloud tops and this excites gravity waves in the stable layer above. To avoid any confusion with internal gravity wave generation by flow over topography, this mechanism has also been called "quasi-stationary forcing" (Fovell *et al.* (1992)). In the deep heating effect, thermal forcing by latent heat release within a convective system acts as gravity wave source (Alexander & Barnet (2007); Pandya & Alexander (1999)). The initial studies of Clark *et al.* (1986) concluded that the obstacle effect was the most important wave generation mechanism. However, the studies by Fovell *et al.* (1992) and later Kumar (2007) show that parcel oscillations within convective updrafts and downdrafts are also responsible for generating the gravity waves. An extensive review by Fritts & Alexander (2003) concluded that all three mechanisms may be important with one mechanism or another serving to explain a set of observations depending upon the environmental conditions.

In a recent study by Kumar (2007), it was pointed out that among convective generation processes, the least understood is the mechanical oscillator effect. Using VHS radar measurements and wavelet analyses, Kumar (2007) carried out a study that showed the observational evidence of the role of the mechanical oscillator effect. The study also mentioned the lack of adequate information to parameterize the full spectrum of convective gravity waves from the various numerical modeling and observational studies and suggested a collaboration among theories, models and observations.

In this study, we report upon laboratory experiments designed to isolate the dynamics of the mechanical oscillator effect acting within a convective storm. Specifically we examine properties of axisymmetric waves emanating from a plume impinging upon a stratified fluid. The waves are visualized and their characteristics and amplitudes are measured using an axisymmetric Synthetic

Schlieren method that measures the amplitudes of axisymmetric disturbances (Onu *et al.* (2003)).

In the numerical simulations of stratospheric gravity waves using a mechanical oscillator cloud model, Fovell *et al.* (1992) observed a fan-like distribution of gravity waves in the stable layer. These investigators pointed out that this aspect of the cloud models is what the single-frequency mechanical oscillator models are not able to mimic.

The study by Pfister *et al.* (1993*a*) traced a transient mesoscale stratospheric gravity wave to a tropical cyclone. The wave generated was studied by using aircraft overflight measurements and satellite imagery, as well as supplementary data of a pilots commentary for the visual description of the overshooting convective turrets. A mechanistic modelling of the gravity wave using a large scale mechanical oscillator model succeeded, to a large degree, in reproducing the observed wave. They stated that the mechanical oscillator model in their case is the growth and decay of an ensemble of updrafts over a few hours that raises and lowers isentropic surfaces on about a 100 km horizontal scale. An alternative approach using the obstacle effect overpredicted the vertical wavelength of the gravity waves.

Other studies investigating gravity wave generation by deep convection via the mechanical oscillator effect include Lane *et al.* (2001) and Song *et al.* (2003). They have employed both two and three-dimensional numerical simulations to study waves generated via deep convection and their propagation into the stratosphere. Unlike previous numerical studies which involved two-dimensional steady sources, Lane *et al.* (2001) have considered the case of three-dimensional transient sources in their simulations.

1.3.3 Generation of internal gravity waves in the ocean

Although the experiments presented in this study are performed with application to the atmosphere as the focus, the results may also be applied to oceanic deep convection. A combination of thermodynamic effects such as rapid cool-

ing, evaporation and freezing may cause surface waters to become denser than deep waters thereby causing parcels of water to sink with entrainment of ambient fluid. These convective plumes have been observed to mix vigorously with their surroundings as they sink with velocities of $2 - 10\,\mathrm{cm/s}$, with vertical scales of $1 - 2\,\mathrm{km}$, and with horizontal scales of the order of $1\,\mathrm{km}$ and occur on time-scales of several hours to days (Paluszkiewcz & Garwood (1994)). A study in the Mediterranean region shows that convection seems to occur in the same place roughly the same time every year (Send & Marshall (1995)). In addition, most of the observations of these convective plumes appear to occur in the Greenland Sea and the Mediterranean region (MEDOC Group (1970); Schott *et al.* (1993)). Upon impacting the stable layer below the mixed layer, deep convective plumes could cause the generation of internal gravity waves which transport momentum from the mixed layer to the deep ocean thereby locally affecting mixing in the deep ocean. Due to the infrequent nature of occurrence of these oceanic plumes, their contribution to the global energy budget associated with internal gravity waves in the ocean is unlikely to be important but the phenomenon is nonetheless interesting to examine.

1.4 Thesis overview

Chapter 2 presents a detailed theoretical derivation of the equations governing the motion of turbulent plumes in uniform and linearly stratified environments. The Eulerian integral solution approach is presented for turbulent plumes in general while the Lagrangian approach is provided for the case of fountains in uniform environments. A method of extending the Lagrangian theory to the case of fountains in two-layer ambient fluids is also provided. An alternative method of calculating the maximum penetration height of a fountain in a two-layer ambient is given in Appendix A.1. The return flow of a fountain in uniform and two-layer environments often gives rise to a radial flow at the source or at the density interface. Similar radial flows are observed in the case of plumes in linearly stratified environments. The theory for predicting

the initial speeds of such radial flows is presented in Chapter 2. This chapter also provides an overview of the axisymmetric internal gravity waves which arise as a result of the evolution of plumes in stratified environments. The detailed derivation of their governing equations and polarization relations are presented in Appendix C.

Chapter 3 presents an experimental study of an axisymmetric turbulent fountain in a two-layer stratified environment. The qualitative observations and quantitative analyses of the experiment are presented in this chapter. The material presented in Chapter 3, in part, is a reprint of the material as it appears in the *Journal of Fluid Mechanics*, Vol. 595, pp. 115-139 (cover article).

Chapter 4 presents the experimental results of the generation of internal gravity waves by a turbulent buoyant plume evolving in a stratified environment. The qualitative observations and quantitative analyses of the experiment are presented in this chapter. The extension of the results to geophysical circumstances is also presented. The materials presented in Chapter 4, in part, have been accepted for publication in the *Journal of Fluid Mechanics*.

Chapter 5 presents a summary and conclusions of this research. We also discuss possible future extensions of this research in this chapter.

Chapter 2

Theory

2.1 Introduction

In this chapter, we derive the governing equations for the flow of a turbulent plume in both uniform and linearly stratified environments. Detailed analysis of the plume equations using the Eulerian Integral Method is presented in Sections 2.2 to 2.5. An alternative approach known as the Lagrangian approach is given for fountains in a uniform ambient fluid in Section 2.6 together with an extension of the theory to the case of fountains in two-layer environments. The theory for predicting the initial speeds of radial currents from fountains and plumes is presented in Section 2.7. The representation of axisymmetric internal gravity waves which arise as a result of the evolution of plumes in stratified environments is presented in Section 2.8. The detailed derivations of the governing equations of axisymmetric internal gravity waves together with the relevant polarization relations are given in Appendix C.

2.2 Governing equations

The equations governing the motion of axisymmetric flow of an inviscid incompressible fluid with no swirl in cylindrical coordinates $(r, \overline{\theta}, z)$ are given by

(Loitsyanskii (1966); Schlichting (1968))

$$\rho_T\left(\frac{\partial v_T}{\partial t}+v_T\frac{\partial v_T}{\partial r}+w_T\frac{\partial v_T}{\partial z}\right) = -\frac{\partial p_T}{\partial r}, \quad (2.1)$$

$$\rho_T\left(\frac{\partial w_T}{\partial t}+v_T\frac{\partial w_T}{\partial r}+w_T\frac{\partial w_T}{\partial z}\right) = -g\rho_T-\frac{\partial p_T}{\partial z}, \quad (2.2)$$

$$\frac{\partial(rv_T)}{\partial r}+\frac{\partial(rw_T)}{\partial z} = 0, \quad (2.3)$$

$$\frac{\partial \rho_T}{\partial t}+v_T\frac{\partial \rho_T}{\partial r}+w_T\frac{\partial \rho_T}{\partial z} = 0, \quad (2.4)$$

where v_T and w_T are the components of velocities in the radial, r, and vertical, z, directions respectively, ρ_T is the density, p_T is the pressure, g is the gravitational acceleration and t is time. Equations (2.1)-(2.4) are respectively the radial momentum, vertical momentum, continuity and density equations. The last two equations are obtained from the equation of mass conservation, $D\rho_T/Dt = -\rho_T\nabla\cdot\mathbf{u}$. For an incompressible fluid, $D\rho_T/Dt = 0$ and so $\nabla\cdot\mathbf{u}=0$; where $\mathbf{u}=(v_T,0,w_T)$ is the velocity field.

One of the convenient ways of mathematically treating turbulent flows is to separate the flow into a mean motion and a fluctuating motion. Each variable, f_T, is then written as the sum of a time-averaged part, f, and a fluctuating part, f':

$$f_T = f + f'.$$

Substituting each decomposed variable into (2.1)-(2.4) and taking the mean of each term results in the Reynolds-averaged equations:

$$\rho\left(v\frac{\partial v}{\partial r}+w\frac{\partial v}{\partial z}\right) = -\frac{\partial p}{\partial r}-\rho\left(\frac{\partial \overline{v'^2}}{\partial r}+\frac{\partial(\overline{v'w'})}{\partial z}+\frac{\overline{v'^2}}{r}\right), \quad (2.5)$$

$$\rho\left(v\frac{\partial w}{\partial r}+w\frac{\partial w}{\partial z}\right) = -g\rho-\frac{\partial p}{\partial z}-\rho\left(\frac{\partial(\overline{v'w'})}{\partial r}+\frac{\partial \overline{w'^2}}{\partial z}+\frac{\overline{v'w'}}{r}\right), \quad (2.6)$$

$$\frac{\partial(rv)}{\partial r} + \frac{\partial(rw)}{\partial z} = 0, \tag{2.7}$$

$$w\frac{\partial \rho}{\partial z} + v\frac{\partial \rho}{\partial r} = -\frac{1}{r}\frac{\partial}{\partial r}(r\overline{\rho' v'}) - \frac{\partial(\overline{\rho' w'})}{\partial z}. \tag{2.8}$$

The mathematical rules of operating on mean time-averages used to arrive at equations (2.5)-(2.8) may be found in Schlichting (1968).

If the flow is steady, or statistically steady, equations (2.5)-(2.8) reduce to

$$\rho\left(v\frac{\partial v}{\partial r} + w\frac{\partial v}{\partial z}\right) = -\frac{\partial p}{\partial r}, \tag{2.9}$$

$$\rho\left(v\frac{\partial w}{\partial r} + w\frac{\partial w}{\partial z}\right) = -g\rho - \frac{\partial p}{\partial z}, \tag{2.10}$$

$$\frac{\partial(rv)}{\partial r} + \frac{\partial(rw)}{\partial z} = 0, \tag{2.11}$$

$$w\frac{\partial \rho}{\partial z} + v\frac{\partial \rho}{\partial r} = 0. \tag{2.12}$$

Given that the density difference between the plume and the ambient is $\Delta\rho = \rho_a(z) - \rho(r,z)$, where $\rho_a(z)$ is the density in the ambient, then using the continuity equation (2.7) and letting $\rho = \rho_a - \Delta\rho$, equation (2.8) may be written as

$$\frac{\partial(rw\Delta\rho)}{\partial z} + \frac{\partial(rv\Delta\rho)}{\partial r} = rw\frac{\mathrm{d}\rho_a}{\mathrm{d}z} + \frac{\partial}{\partial r}(r\overline{\rho' v'}) + \frac{\partial}{\partial z}(r\overline{\rho' w'}). \tag{2.13}$$

Equation (2.13) is more convenient since it explicitly shows the ambient density profile (the first term on the right hand side of (2.13)). If the buoyancy in the plume is driven by temperature differences, $\Delta T = T(r,z) - T_a(z)$, where $T(r,z)$ is the temperature in the plume and $T_a(z)$ is the ambient temperature, then $\Delta\rho$ may be replaced by ΔT (this is consistent with using a simplified equation of state) to get an equation similar to (2.13) (see for example Batchelor (1954); Morton (1967, 1971); Shabbir & George (1994)). The buoyancy in the experiments reported here are caused by density differences so equation (2.13) will be used in the following derivations.

The governing equations are simplified by using the Boussinesq approxi-

mation (that is, for small density differences, the density can be replaced by a constant reference density except where it is multiplied by the acceleration due to gravity term) and the boundary-layer approximations:

1. the velocities in the axial direction are far greater than those in the radial direction; $v \ll w$.

2. the gradients of velocity in the radial direction are larger than those in the axial direction; $\frac{\partial}{\partial z} \ll \frac{\partial}{\partial r}$.

Using the above approximations, equation (2.5) reduces to (also see Tennekes & Lumley (1972))

$$0 = -\frac{\partial p}{\partial r} - \rho \frac{\partial \overline{v'^2}}{\partial r}. \tag{2.14}$$

Integrating (2.14) radially from r to infinity (where infinity in this case refers to the region well outside the plume), we get

$$\begin{aligned} \int_r^\infty \frac{\partial p}{\partial r'} \mathrm{d}r' &= -\int_r^\infty \rho \frac{\partial \overline{v'^2}}{\partial r'} \mathrm{d}r', \\ \implies p_\infty - p &= \rho \overline{v'^2}, \end{aligned} \tag{2.15}$$

where p_∞ is the pressure in the environment and we have assumed that $\overline{v'^2}$ goes to zero as r goes to infinity. Differentiating (2.15) with respect to z and substituting into (2.6), we get

$$\rho \left(v \frac{\partial w}{\partial r} + w \frac{\partial w}{\partial z} \right) = -g\rho - \frac{\mathrm{d}p_\infty}{\mathrm{d}z} - \rho \left(\frac{\partial (\overline{v'w'})}{\partial r} + \frac{\overline{v'w'}}{r} - \frac{\partial}{\partial z} [\overline{v'^2} - \overline{w'^2}] \right). \tag{2.16}$$

The last term is smaller than the rest since $\overline{v'^2} \sim \overline{w'^2}$ (Rajaratnam (1976); Lee & Chu (2003)) so it can be neglected. Moreover,

$$\frac{\partial (\overline{v'w'})}{\partial r} + \frac{\overline{v'w'}}{r} = \frac{1}{r} \frac{\partial}{\partial r} (r \overline{v'w'}),$$

and so (2.16) becomes

$$\rho\left(v\frac{\partial w}{\partial r}+w\frac{\partial w}{\partial z}\right)=-g\rho-\frac{\mathrm{d}p_\infty}{\mathrm{d}z}-\rho\frac{1}{r}\frac{\partial}{\partial r}(r\overline{v'w'}). \tag{2.17}$$

In the ambient where there is no flow, we have the hydrostatic pressure distribution:

$$\frac{\mathrm{d}p_\infty}{\mathrm{d}z}=-\rho_a(z)g. \tag{2.18}$$

Employing the Boussinesq approximation, we replace the density by a reference density, $\rho_{00}=\rho_a(0)$, in all terms except $g\rho$. Equation (2.17) becomes

$$v\frac{\partial w}{\partial r}+w\frac{\partial w}{\partial z}=g'-\frac{1}{r}\frac{\partial}{\partial r}(r\overline{v'w'}), \tag{2.19}$$

where $g'=\frac{(\rho_a-\rho)}{\rho_{00}}g$ is the reduced gravity.

The governing equations for the plume flow then become

$$v\frac{\partial w}{\partial r}+w\frac{\partial w}{\partial z}=g'-\frac{1}{r}\frac{\partial}{\partial r}(r\overline{v'w'}), \tag{2.20}$$

$$\frac{\partial(rv)}{\partial r}+\frac{\partial(rw)}{\partial z}=0, \tag{2.21}$$

$$\frac{\partial(rw\Delta\rho)}{\partial z}+\frac{\partial(rv\Delta\rho)}{\partial r}=rw\frac{\mathrm{d}\rho_a}{\mathrm{d}z}+\frac{\partial}{\partial r}(r\overline{\rho'v'}). \tag{2.22}$$

In principle, given appropriate boundary conditions, equations (2.20)-(2.22) can be solved for the parameters v, w and $\Delta\rho$ if the covariances $\overline{v'w'}$ and $\overline{\rho'v'}$ can be written in terms of the mean flow variables.

Boundary conditions can be specified by taking advantage of the symmetry in the flow. At the axis, $r=0$, the covariances as well as the derivatives with respect to r go to zero. Away from the axis, $r\to\infty$, the covariances and all the mean flow variables go to zero (this is because a finite disturbance concentrated around the axis of the plume cannot result in a finite disturbance at an infinite radial distance (Morton (1971))).

Writing the covariances in terms of the mean variables (the closure problem) has not been successful, for the most part, in solving the problem (Morton (1971)). A complete solution to the problem is difficult since it requires matching an inner solution inside the plume to an outer solution of the ambient. However, the governing equations specified here are valid within the plume while much is unknown about the flow induced in the environment. Because of this difficulty, a common approach is to solve for only the inner solution and make an assumption regarding the inflow of the ambient fluid into the plume. A recent theoretical development has presented solutions for a two-fluid model (see Scase *et al.* (2007)).

One method often used to solve these system of equations is the Eulerian integral method (Turner (1973)) which is discussed next. The Lagrangian method is described in Section 2.6.

2.3 Eulerian integral solution approach

The Eulerian integral solution approach to solving (2.20)-(2.22) involves integrating the equations across the whole width of the buoyant plume. The integration procedure results in the cancelation of the terms with the fluctuating quantities and this greatly reduces the difficulty in solving the system of plume equations. Once profile shapes are specified for the velocity and density, the integration can readily be carried out to convert the system of partial differential equations to a system of ordinary differential equations (ODEs). An assumption regarding the entrainment of ambient fluid into the plume results in a closure of the system of ODEs. The plume equations often cited in the literature are the final ODEs without detailed explanation about their derivation. In the following, we carry out the above solution procedure to obtain the final plume equations.

Integrating the vertical momentum equation (2.20)

Using the continuity equation, we rewrite equation (2.20) as

$$\frac{\partial(rvw)}{\partial r} + \frac{\partial(rw^2)}{\partial z} = rg' - \frac{\partial(r\overline{v'w'})}{\partial r}. \tag{2.23}$$

Multiplying (2.23) by 2π and integrating from $r = 0$ to infinity, we get

$$\frac{\mathrm{d}}{\mathrm{d}z}\int_0^\infty 2\pi rw^2 \mathrm{d}r + [rvw]_0^\infty = \int_0^\infty 2\pi rg' \mathrm{d}r - [r\overline{v'w'}]_0^\infty,$$

so that

$$\frac{\mathrm{d}}{\mathrm{d}z}\int_0^\infty 2\pi rw^2 \mathrm{d}r = \int_0^\infty 2\pi rg' \mathrm{d}r, \tag{2.24}$$

since vw and $\overline{v'w'} \to 0$ as $r \to \infty$. Equation (2.24) states that, in a linearly stratified environment, the momentum flux (the integral on the left-hand-side) increases with height while the buoyancy (the integral on the right-hand-side) is positive. It then decreases to zero in the region of negative buoyancy (eg near a plume top). In a fountain, the buoyancy is always negative so the momentum flux decreases to zero at the fountain top.

Integrating the continuity equation (2.21)

Multiplying equation (2.21) by 2π and integrating from $r = 0$ to infinity, we get

$$\begin{aligned} \int_0^\infty 2\pi \frac{\partial(rw)}{\partial z}\mathrm{d}r &= -\int_0^\infty 2\pi \frac{\partial(rv)}{\partial r}\mathrm{d}r, \\ \Longrightarrow \frac{\mathrm{d}}{\mathrm{d}z}\int_0^\infty 2\pi rw \mathrm{d}r &= -2\pi \left[rv\right]_0^\infty. \end{aligned} \tag{2.25}$$

Now as r goes to infinity, v goes to zero, but the product rv remains finite (Morton (1971); Lee & Chu (2003)). The product is a measure of the entrainment of ambient fluid into the plume (see figure 2.1). We define the flow rate of entrainment by $Q_E = 2\pi b v_e$ where b is the characteristic radius of the plume

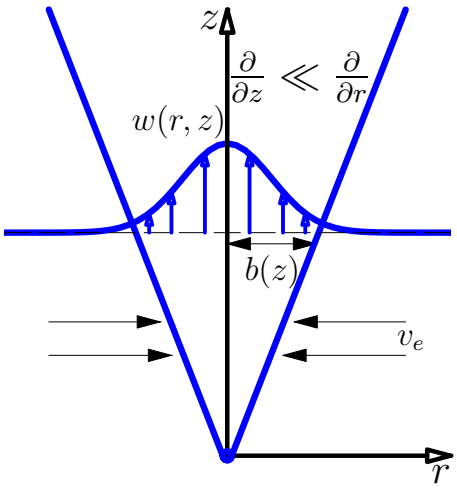

Figure 2.1: Schematic of plume flow

and v_e is the entrainment velocity. Morton *et al.* (1956) defined the radius of the plume to be the actual radius from the centerline to the plume edge for top-hat profiles while the radius is defined, at each height, as the distance from the plume centerline to a point at which the velocity and buoyancy amplitudes are e^{-1} of those on the axis. The implications of these definitions have recently been addressed in Scase *et al.* (2007). So equation (2.25) may be written as

$$\frac{\mathrm{d}}{\mathrm{d}z}\int_0^\infty 2\pi r w \mathrm{d}r = Q_E. \tag{2.26}$$

Equation (2.26) states that the volume flux in the plume (the integral on the left-hand-side) increases with height due to the entrainment of ambient fluid.

Integrating the density equation (2.22)

Integrating equation (2.22) from $r = 0$ to infinity, we have

$$\frac{\mathrm{d}}{\mathrm{d}z}\int_0^\infty rw\Delta\rho \mathrm{d}r + [rv\Delta\rho]_0^\infty = \frac{\mathrm{d}\rho_a}{\mathrm{d}z}\int_0^\infty rw\mathrm{d}r + \left[r\overline{\rho' v'}\right]_0^\infty. \tag{2.27}$$

Now as r goes to infinity rv is bounded but $\Delta\rho$ goes to zero while $\overline{\rho' v'}$ also goes to zero at infinity. So equation (2.27) reduces to

$$\frac{\mathrm{d}}{\mathrm{d}z}\int_0^\infty 2\pi r w g' \mathrm{d}r = 2\pi \frac{g}{\rho_{00}} \frac{\mathrm{d}\rho_a}{\mathrm{d}z} \int_0^\infty r w \mathrm{d}r. \tag{2.28}$$

This equation is obtained by multiplying through by the constant ratio $2\pi g/\rho_{00}$. Equation (2.28) states that in a stably stratified environment the buoyancy flux decreases with height due to the entrainment of ambient fluid into the plume and the rate of decrease is proportional to the ambient density gradient.

Thus the integrated equations governing the plume flow are respectively given by (2.26), (2.24) and (2.28):

$$\begin{aligned}
\frac{\mathrm{d}}{\mathrm{d}z}\int_0^\infty 2\pi r w \mathrm{d}r &= 2\pi b v_e, & (2.29)\\
\frac{\mathrm{d}}{\mathrm{d}z}\int_0^\infty 2\pi r w^2 \mathrm{d}r &= \int_0^\infty 2\pi r g' \mathrm{d}r, & (2.30)\\
\frac{\mathrm{d}}{\mathrm{d}z}\int_0^\infty 2\pi r w g' \mathrm{d}r &= 2\pi \frac{g}{\rho_{00}} \frac{\mathrm{d}\rho_a}{\mathrm{d}z} \int_0^\infty r w \mathrm{d}r. & (2.31)
\end{aligned}$$

Performing the integrations above require specifying shape functions for the velocity and reduced gravity. The two approximations often used to represent these profiles are the Gaussian and Top-hat profiles.

2.3.1 Gaussian profile

Here, the profiles of velocity and density across any horizontal section of the developed plume is assumed to be Gaussian in shape such that

$$w(z,r) = w_m(z) e^{-\left(\frac{r}{b}\right)^2}, \tag{2.32}$$

$$g'(z,r) = g'_m(z) e^{-\left(\frac{r}{\lambda b}\right)^2}, \tag{2.33}$$

where b characterizes the radius scale in the velocity profile while λb characterizes the radius scale in the density profile. The use of the different length scales has been justified in the literature based upon the experimental results

of Rouse *et al.* (1952). Substituting (2.32) and (2.33) into (2.29)-(2.31), we get

$$\frac{\mathrm{d}}{\mathrm{d}z}\left(\pi b^2 w_m\right) = 2\pi b v_e, \tag{2.34}$$

$$\frac{\mathrm{d}}{\mathrm{d}z}\left(\frac{1}{2}\pi b^2 w_m^2\right) = \pi g'_m \lambda^2 b^2, \tag{2.35}$$

$$\frac{\mathrm{d}}{\mathrm{d}z}\left(\pi b^2 w_m g'_m \frac{\lambda^2}{1+\lambda^2}\right) = \pi b^2 w_m \frac{g}{\rho_{00}}\frac{\mathrm{d}\rho_a}{\mathrm{d}z}. \tag{2.36}$$

The final information required to close the above system of equations is an assumption about the velocity of entrainment of ambient fluid, v_e, into the plume. This is referred to as the entrainment hypothesis which is discussed below.

2.3.2 Entrainment hypothesis

The entrainment hypothesis stipulates that the velocity of entrainment of ambient fluid into the plume is proportional to the axial velocity of the plume so that

$$v_e = \alpha w(z), \tag{2.37}$$

where α is called the entrainment coefficient. This hypothesis is attributed to Morton *et al.* (1956) and has been used successfully to model plumes with different steady source conditions. The hypothesis has previously been employed by Batchelor (1954) to study turbulent plumes in uniform and stratified environments. Batchelor (1954) stated that the idea behind this hypothesis is that the turbulent velocity fluctuations within the plume will be proportional to the mean vertical velocity, and the inflow velocity will in turn be proportional to the turbulent velocity.

The entrainment coefficient was initially thought to be a universal constant for plume flows but subsequent theoretical and experimental studies have shown that this is not the case. Its value depends on the choice of the

velocity profile. Reviews of the literature show that $\alpha = 0.076$ (for a jet), $\alpha = 0.12$ (for a Top-hat plume) and $\alpha = 0.085$ (for a fountain) (Fischer *et al.* (1979); List (1982); Bloomfield & Kerr (2000)).

Substituting (2.37) into (2.34), the continuity equation governing a Gaussian plume is

$$\frac{\mathrm{d}}{\mathrm{d}z}\left(\pi b^2 w_m\right) = 2\pi b\alpha w. \tag{2.38}$$

If $\lambda = 1$ in (2.35) and (2.36) (assuming equal spread in the profiles of velocity and density) and after dividing through by the π's in the above equations, the results of Morton *et al.* (1956) (their equation 7) is obtained.

2.3.3 Top-hat profile

Here, the profiles of velocity and density are assumed to take one value within the plume and zero outside:

$$w(r,z) = \begin{cases} \overline{w}(z), & r < b \\ 0, & r > b \end{cases}, \quad g'(r,z) = \begin{cases} \overline{g'}(z), & r < b \\ 0, & r > b \end{cases},$$

where we have assumed equal spread for velocity and density ($\lambda \approx 1$) for top-hat profiles (Morton (1959*b*)). An equivalent integral definition of the top-hat profile is given in Turner (1973). Substituting these profiles into (2.29)-(2.31) and using the entrainment hypothesis results in the following governing equations for the top-hat plume

$$\frac{\mathrm{d}}{\mathrm{d}z}\left(\pi b^2 \overline{w}\right) = 2\pi b\alpha\overline{w}, \tag{2.39}$$

$$\frac{\mathrm{d}}{\mathrm{d}z}\left(\pi b^2 \overline{w}^2\right) = \pi b^2 g'(z), \tag{2.40}$$

$$\frac{\mathrm{d}}{\mathrm{d}z}\left(\pi b^2 \overline{w} g'\right) = \pi b^2 \overline{w}\frac{g}{\rho_{00}}\frac{\mathrm{d}\rho_a}{\mathrm{d}z}. \tag{2.41}$$

Dividing through by π, these equations are equivalent to the equations obtained by Morton *et al.* (1956) (their equation 3). It is convenient to analyze

these equations by recasting them in terms of the fluxes of momentum M, volume Q, and buoyancy, F, defined as $M = \pi b^2 \overline{w}^2$, $Q = \pi b \overline{w}^2$ and $F = \pi b \overline{w}^2 g'$ to get

$$\frac{\mathrm{d}Q}{\mathrm{d}z} = 2\alpha\pi^{1/2}\sqrt{M}, \tag{2.42}$$

$$\frac{\mathrm{d}M}{\mathrm{d}z} = FQ/M, \tag{2.43}$$

$$\frac{\mathrm{d}F}{\mathrm{d}z} = -QN^2, \tag{2.44}$$

where N is the buoyancy frequency related to the ambient stratification and defined by

$$N^2 = -\frac{g}{\rho_{00}}\frac{\mathrm{d}\rho_a}{\mathrm{d}z}. \tag{2.45}$$

2.3.4 Gaussian versus top-hat profiles

The similarity of the profiles of velocity and density away from the source is one of the main assumptions used in the Eulerian integral approach. This is a necessary step since the shape of the radial profiles cannot be obtained from the integrated equations and have to be assumed. The particular choice of a profile is a matter of convenience and little physical significance is often attached to this choice (Morton (1971); Turner (1973)). The simple top-hat profile will be used in this study.

Equivalent relations between these two profiles may be found by using the conservation of mass and momentum equations. For instance, letting subscripts g and t represent Gaussian and top-hat variables, we get by respectively equating the left hand sides of (2.34) and (2.35) to those of (2.39) and (2.40) (also see Henderson-Sellers (1981)):

$$b_g^2 w_g = b_t^2 w_t, \qquad \frac{1}{2} b_g^2 w_g^2 = b_t^2 w_t^2.$$

From the two equations above we get

$$w_t = \frac{w_g}{2}, \qquad b_t = \sqrt{2} b_g. \tag{2.46}$$

These relations mean that at each height the axial velocity of a top-hat plume is half that of the Gaussian plume and its width is a factor of $\sqrt{2}$ wider. Similarly equating the right hand sides of the conservation of mass equations give

$$b_g \alpha_g w_g = b_t \alpha_t w_t, \quad \Longrightarrow \alpha_t = \sqrt{2} \alpha_g. \tag{2.47}$$

2.4 Solutions to the governing equations

The governing ODEs derived above can be solved numerically given any steady source conditions and ambient linear stratification. However, under special circumstances, exact analytic solutions may be found. Examples include plumes and jets from point sources in uniform ambient fluids.

2.4.1 Uniform environment

In a uniform ambient fluid ($N = 0$), the right hand side of equation (2.44) goes to zero resulting in

$$F = F_0 \quad \text{(constant)} \tag{2.48}$$

where F_0 is the buoyancy flux at the source. Thus, the buoyancy flux remains constant with height in a uniform ambient fluid.

Pure plume

If the initial momentum flux is zero (with the plume rising from a point source under the influence of only buoyancy forces), then the ODEs are easily solved to get, for a top-hat plume (Morton *et al.* (1956)),

$$b = \left(\frac{6\alpha}{5}\right) z, \tag{2.49}$$

$$w = \left(\frac{5}{6\alpha}\right)\left(\frac{9}{10}\alpha F_0\right)^{1/3} z^{-1/3}, \tag{2.50}$$

$$g' = \left(\frac{5F_0}{6\alpha}\right)\left(\frac{9}{10}\alpha F_0\right)^{-1/3} z^{-5/3}. \tag{2.51}$$

Similar similarity solutions had previously been obtained by Zeldovich (1937). As expected, the solution indicates that the plume spreads linearly with height. The axial velocity decreases as $z^{-1/3}$ while the density difference also decreases as $z^{-5/3}$. However, under these ideal conditions, the plume will continue to rise indefinitely. Under real environmental conditions, the presence of winds and other currents will usually result in the enhanced dispersion of the plume. Away from the source, the solution from the point source pure plume may be used to predict, for example, the time-averaged properties of smoke rising from a cigarette. They cannot predict source conditions because of the singularity at the source.

Jet

In the absence of a density difference between the source and the ambient fluids (zero buoyancy flux), the governing equations for a top-hat plume in a uniform ambient reduce to

$$\begin{aligned} \frac{\mathrm{d}Q}{\mathrm{d}z} &= 2\alpha\pi^{1/2}\sqrt{M}, \\ \frac{\mathrm{d}M}{\mathrm{d}z} &= 0, \end{aligned} \tag{2.52}$$

which can be solved to get

$$b = 2\alpha\pi^{-1}z, \quad w = \frac{\sqrt{\pi}}{2\alpha}M_0^{1/2}z^{-1}. \tag{2.53}$$

Thus, in the case of a jet from a point source, it is the momentum flux that is conserved with height (see equation 2.52). The solution in this case also predicts a linear spread of the jet fluid even though the angle of spread in this case is larger and the axial velocity decreases faster as z^{-1}. The controlling parameter in this case is the initial momentum flux unlike the pure plume case where the dynamics are controlled by the initial buoyancy flux.

Forced plumes

In most practical environmental circumstances, plumes are usually issued from an area source with both momentum and buoyancy. The name "forced plumes" was introduced by Morton (1959*b*) to describe these intermediate cases. They are sometimes referred to as "buoyant jets" because they exhibit both jet and pure plume dynamics in the flow field. In the following we discuss both positively buoyant plumes and fountains. Further discussion on fountains is presented in Section 2.6 under the Lagrangian approach.

Positively buoyant plumes

Positively buoyant jets initially behave like a jet (where the flow is mainly controlled by the initial momentum flux) and then transition to a pure plume far from the source (the flow being controlled by the initial buoyancy flux). The length scale separating jet-like and plume-like behaviour is given by (Morton (1959*b*); Fischer *et al.* (1979))

$$L_m = M_0^{3/4}/F_0^{1/2}. \tag{2.54}$$

The asymptotic behaviour of the forced plume in this case may be determined in terms of the variable

$$\zeta = \frac{z}{L_m}. \tag{2.55}$$

(1) $\zeta \to 0$ means that $z \to 0$ with L_m fixed or z is fixed and $L_m \to \infty$. The latter limit occurs as $F_0 \to 0$, which is the case for a jet. This means that close to the source the forced plume acts like a jet and is dominated by the source momentum flux.

(2) $\zeta \to \infty$ means that $z \to \infty$ with L_m fixed or z is fixed with $L_m \to 0$. The latter limit occurs as $M_0 \to 0$, which is the case for a pure plume. Thus, far away from the source the forced plume acts like a pure plume and is dominated by the source buoyancy flux.

The experiments of Papanicolaou & List (1988) show that the flow is jet-like for $\zeta < 1$ and plume-like for $\zeta > 5$.

Fountains

Fountains or negatively buoyant plumes are formed either when dense fluid is continuously discharged upward into a less dense fluid or when less dense fluid is injected downward into a more dense environment. In either case, the buoyancy opposes the momentum of the flow until the fountain reaches a height where the vertical velocity goes to zero. The fountain then reverses direction and falls back upon the source.

Theoretical treatment of this flow was first undertaken by Priestley & Ball (1955); Morton (1959*a*) and Abraham (1963). Initial experimental studies were undertaken by Turner (1966) by injecting heavy salt solution upward into fresh ambient water. On dimensional grounds, Turner (1966) obtained

the following expression for the maximum height

$$z_{\max} = C_f M_0^{3/4} F_0^{-1/2}, \tag{2.56}$$

where the empirically-determined constant $C_f = 2.46$.

Priestley & Ball (1955) and Morton (1959*b*) solved the governing equations to get relations for the maximum penetration height though they used different closure assumptions.

Abraham (1963) divided the problem into four zones: a zone of flow establishment where the fountain initially acts like a jet; a zone of established flow where the flow is considered to be fully established and permits the assumption of self-similarity; a zone of positive entrainment where the fountain entrains fluid from the environment; and a zone of negative entrainment (close to the maximum height) where the fountain does not entrain fluid from the ambient but begins to return toward the source. The latter two zones were merged via the continuity of volume flux, and the spreading hypothesis was used in the zone of positive entrainment to solve the resulting equations for the maximum penetration height.

All three theoretical treatments above obtained an expression similar to (2.56) for the maximum rise height though with different constants, C_f. Abraham (1967) compared the three solutions to the experimental results of Turner (1966) and found that the solution of Morton (1959*b*) predicted 84% of the experimental maximum heights, that of Priestley & Ball (1955) predicted 110% while his formula predicted 111% (that is, $C_f = 2.74$). Abraham (1967) argued that the assumption of Morton (1959*b*) that the vertical flux of a tracer carried by the fountain remained constant from the source to the maximum height was not appropriate because of the detrainment of fountain fluid close to the maximum height.

To compare to experimental findings of fountains, it is important to use the appropriate theory especially in the case of fountains in two-layer stratified environments. A theory which underestimates the penetration height

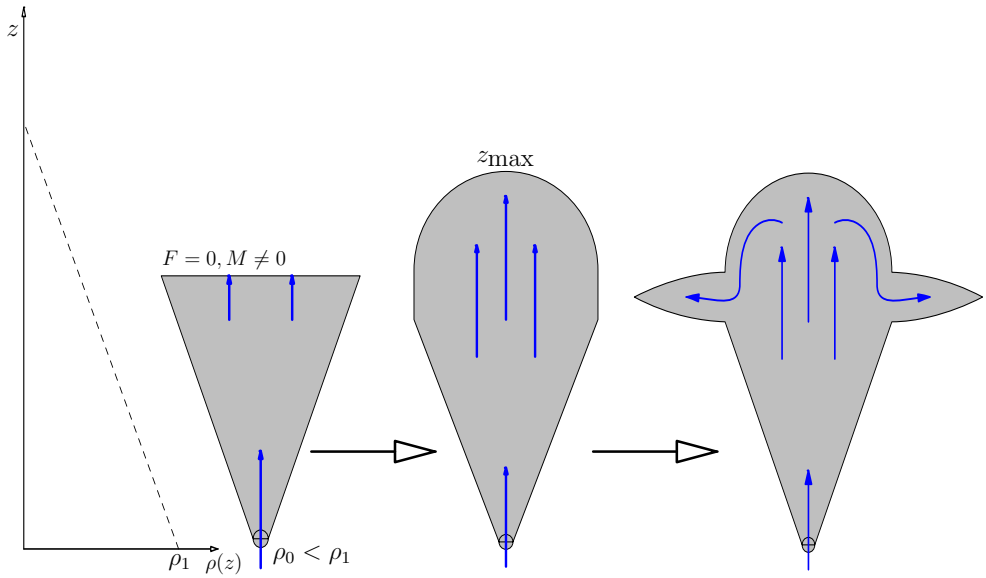

Figure 2.2: Schematic of plume in a linearly stratified environment

could make it difficult to determine theoretically the behaviour of the fountain beyond the density interface.

An alternative approach is the Lagrangian method in which a marked material volume issuing from a plume source is followed in time. The solutions are much simpler to obtain and interpret and they give very good agreement with the Eulerian integral method. This theory will be discussed in Section 2.6.

2.4.2 Plumes in linearly stratified environments

In a linearly stratified ambient, a plume evolves upward with initial density which is less than the density of the ambient at the source level (figure 2.2). As the plume evolves, it is constantly entraining relatively dense fluid at low levels which is then advected upwards. Due to the fact that the density of the environment is decreasing with height, the plume reaches a level where its density becomes equal to the density of the environment. The buoyancy flux of the plume then vanishes at this height. This height is referred to as the neutral buoyancy level. However, the plume still has some momentum at this level

and so it overshoots this height to the maximum penetration height, $z_{\max}$. The fluid above the neutral buoyancy level is heavier than the surrounding fluid and so it falls upon itself like a fountain and begins to spread radially as an intrusive gravity current. As a result of the continuous release of fluid from the source, the fluid above the neutral level forms a dome-like shape whose boundary is constantly fluctuating about a quasi-steady-state height.

The governing ODEs (2.42-2.44) may be solved numerically for the mean properties of the plume at each height. The level of neutral buoyancy is obtained at the height where the buoyancy flux first vanishes and the maximum penetration height is obtained at the height where the momentum flux goes to zero. For point source pure plumes and point source forced plumes in linearly stratified environments, analytic expressions for the maximum penetration height has recently be presented by Scase *et al.* (2006*b*).

2.5 Plume energetics

A good prediction of the energy extracted from convective elements at a density interface require the knowledge of the kinetic energy of the convective elements when they reach the interface. Turner (1972) discussed this problem for axisymmetric and plane plumes as well as for buoyant thermals by considering both top-hat and Gaussian profiles of the flow quantities. For round plumes in neutral surroundings, it was found that the fraction of the rate of working by buoyancy forces that is actually realized as the mean flow kinetic energy flux was $\frac{3}{8}$ for top-hat profiles and $\frac{1}{2}$ for Gaussian profiles. In the following, we derive the equation governing the energy balance in a plume and use the approach of Turner (1972) to obtain an expression for calculating the energy flux of a plume at any height, z, from the virtual origin.

Multiplying equation (2.20) through by $r\rho w$, we get

$$\rho w^2 \frac{\partial (rw)}{\partial z} + \rho r v w \frac{\partial w}{\partial r} = \rho r g' w - \rho w \frac{\partial (r\overline{w'v'})}{\partial r}. \tag{2.57}$$

Adding the expression $\frac{\rho w^2}{2}\frac{\partial(rw)}{\partial z} + \frac{\rho w^2}{2}\frac{\partial(rv)}{\partial r}$ (which is zero from the continuity equation) to the left hand side of (2.57), we get

$$\frac{3\rho w^2}{2}\frac{\partial(rw)}{\partial z} + \rho rvw\frac{\partial w}{\partial r} + \frac{\rho w^2}{2}\frac{\partial(rv)}{\partial r} = \rho rg'w - \rho w\frac{\partial(r\overline{w'v'})}{\partial r}. \tag{2.58}$$

This formula is rearranged using the relations

$$\frac{3}{2}\rho w^2\frac{\partial(rw)}{\partial z} = \frac{\partial}{\partial z}\left(\frac{1}{2}\rho rw^3\right) - \frac{w^3}{2}\frac{\partial(r\rho)}{\partial z}, \tag{2.59}$$

and

$$\frac{\partial}{\partial r}\left(\frac{1}{2}\rho rvw^2\right) = \rho rvw\frac{\partial w}{\partial r} + \frac{w^2}{2}\frac{\partial(\rho rv)}{\partial r}. \tag{2.60}$$

Also from (2.12) and the continuity equation for incompressible fluid (2.7) we get

$$\frac{\partial(\rho rv)}{\partial r} + \frac{\partial(\rho rw)}{\partial z} = 0. \tag{2.61}$$

Thus, (2.60) becomes

$$\frac{\partial}{\partial r}\left(\frac{1}{2}\rho rvw^2\right) = \rho rvw\frac{\partial w}{\partial r} - \frac{w^3}{2}\frac{\partial(r\rho)}{\partial z} - \frac{\rho w^2}{2}\frac{\partial(rw)}{\partial z}, \tag{2.62}$$

which, using (2.7), gives

$$\rho rvw\frac{\partial w}{\partial r} = \frac{\partial}{\partial r}\left(\frac{1}{2}\rho rvw^2\right) + \frac{w^3}{2}\frac{\partial(r\rho)}{\partial z} - \frac{\rho w^2}{2}\frac{\partial(rv)}{\partial r}. \tag{2.63}$$

From (2.59) and (2.63), the left hand side of (2.58) simplifies to the expression

$$\frac{\partial}{\partial z}\left(\frac{1}{2}\rho rw^3\right) + \frac{\partial}{\partial r}\left(\frac{1}{2}\rho rvw^2\right),$$

and so equation (2.58) finally becomes

$$\frac{\partial}{\partial z}\left(\frac{1}{2}\rho r w^3\right) + \frac{\partial}{\partial r}\left(\frac{1}{2}\rho r v w^2\right) = \rho r g' w - \rho w \frac{\partial(r\overline{w'v'})}{\partial r}. \tag{2.64}$$

Multiplying through by 2π and integrating from $r = 0$ to $r \to \infty$, we get

$$\frac{\mathrm{d}}{\mathrm{d}z}\int_0^\infty (\rho w)\frac{w^2}{2}(2\pi r)\mathrm{d}r = \int_0^\infty \rho w g'(2\pi r)\mathrm{d}r - \int_0^\infty 2\pi\rho w \frac{\partial(r\overline{w'v'})}{\partial r}\mathrm{d}r. \tag{2.65}$$

The second term on the left-hand-side vanishes because $vw \to 0$ as $r \to \infty$. Using the boundary condition that $\overline{w'v'} \to 0$ as $r \to \infty$, the last term of equation (2.65) may be integrated to give

$$\frac{\mathrm{d}}{\mathrm{d}z}\int_0^\infty (\rho w)\frac{w^2}{2}(2\pi r)\mathrm{d}r = \int_0^\infty \rho g' w(2\pi r)\mathrm{d}r - \int_0^\infty \tau_s \frac{\partial w}{\partial r}(2\pi r)\mathrm{d}r, \tag{2.66}$$

where the quantity $\tau_s = -\rho\overline{w'v'}$ is the turbulent shear stress or Reynolds stress. Equation (2.66) states that the rate of change of the kinetic energy flux in the plume is due to work owing to buoyancy forces and production by turbulence in shear. In a jet, the first term on the right-hand-side of (2.66) vanishes and the change of the kinetic energy flux is just equal to the rate of energy production by turbulence (Rajaratnam (1976)).

2.5.1 Energy ratios

The horizontally-integrated flux of kinetic energy, F_k, across the horizontal plane of a buoyant plume at height z and the rate of working due to buoyancy forces, W_p, are given respectively by (Turner (1972))

$$F_k = \pi\rho_{00}\int_0^\infty w^3 r\mathrm{d}r, \tag{2.67}$$

$$W_p = 2\pi\rho_{00}\int_0^\infty w g' r\mathrm{d}r, \tag{2.68}$$

where ρ_{00} is a reference density. Note that the equations above are respectively the left-hand-side and the first term on the right-hand-side of equation (2.66)

when ρ is replaced by ρ_{00} (for a Boussinesq plume). Assuming top-hat profiles, equation (2.67) may be evaluated to get

$$F_k = \frac{1}{2}\rho_{00}\pi\overline{w}^3 b^2, \tag{2.69}$$

where $\overline{w}$ is the average vertical velocity at height z and b is the plume radius. For top-hat profiles, the ratio of the divergence of the kinetic energy flux to the rate of working owing to buoyancy forces is given by (Turner (1972))

$$\frac{\partial F_k/\partial z}{W_p} = \frac{3}{8}. \tag{2.70}$$

Thus the vertically integrated rate of working of the plume, F_{plume}, from the virtual origin to a height $z = H$ is

$$F_{\text{plume}} = \frac{4}{3}\rho_{00}\pi\overline{w}_i^3 b_i^2, \tag{2.71}$$

assuming W_p is zero at the virtual origin. Here $\overline{w}_i$ and b_i are the average vertical velocity and radius of the plume at $z = H$. In the case of a plume in a linearly stratified environment, equation (2.71) is also used to estimate the rate of working of the plume at its neutral buoyancy level with $\overline{w}_i$ and b_i replaced by the vertical velocity w_n and radius b_n of the plume at the level of neutral buoyancy, z_n.

2.6 Lagrangian approach

2.6.1 Introduction

The conventional and most widely used approach to solving problems of turbulent buoyant jets is by using the conservation equations of turbulent flow of an incompressible fluid and employing the Boussinesq and boundary layer approximations (see Section 2.2). The resulting equations are typically solved by using the Eulerian integral method (Turner (1973)). Here a form is first

assumed for the velocity and concentration profiles of the plume. This could either be the Gaussian profile or the top-hat profile. The equations are then integrated over the plume cross-section and the assumed profiles are substituted. The result is three ordinary differential equations (ODEs) which may be solved numerically or, in special circumstances, analytically. However, an assumption has to be made to close the system of ODEs. This could either be the entrainment assumption introduced by Morton *et al.* (1956), or the spreading assumption introduced by Abraham (1963).

In the case of fountains, when the fountain reverses direction from the maximum height, the rising upward flow then entrains fluid from the downflow and vice versa and also continues to entrain fluid from the environment until the fountain collapses at the level of the source. It is difficult to ascertain the amount of the mixed fluid entrained into the fountain, and the theoretical approach mentioned above treats the problem as if only the ambient fluid is entrained.

An alternative approach is the Lagrangian method in which a marked material volume issuing from a plume source is followed in time (Middleton (1975); Baines & Chu (1996); Lee & Chu (2003)). The solutions are much simpler to obtain and interpret and they give very good agreement with the Eulerian integral method.

Here, we give a brief review of the Lagrangian method for a fountain from a point source of flow in a uniform ambient. We will also extend this to the case of fountains in two-layer stratified environments. Specifically, we derive an equation for predicting the maximum penetration height of a fountain from a point source in a two-layer environment. Detailed derivations of the Lagrangian equations as well as those for a fountain from an area source are given in Appendix A.1.

2.6.2 Fountains from a point source

Newton's law is applied to a material volume such that the rate of change of the vertical momentum of the plume element is equal to the buoyancy force:

$$\frac{dM}{dt} = -F_0, \tag{2.72}$$

where M and $F_0 > 0$ are the momentum and buoyancy fluxes respectively. Explicitly, assuming a top-hat-shaped plume of radius r and mean vertical velocity w, $M = \pi r^2 w^2$ and $F_0 = \pi r_0^2 w_0 g'$, in which $g' = (\rho - \rho_a)g/\rho_0$ is the reduced gravity, r_0 is the source radius, w_0 is the average vertical velocity at the source, ρ_a is the ambient density, ρ is the density of the fountain at a given height and ρ_0 is the initial density of the fountain. We apply the spreading hypothesis which assumes that $\mathrm{d}r/\mathrm{d}z = \beta$, where $\beta \approx 0.17$ is an empirically determined constant spreading coefficient (Baines & Chu (1996); Lee & Chu (2003)). The buoyancy flux F_0 is constant in a uniform ambient. Thus we get the following relations for the radius, b, height, z, volume flux, $Q = \pi r^2 w$, and momentum flux, M, of the fountain as a function of time, t:

$$b = \left(\frac{4\beta}{3\sqrt{\pi}}\right)^{1/2} \frac{M_0^{3/4}}{F_0^{1/2}} \left[1 - \left(1 - \frac{F_0 t}{M_0}\right)^{3/2}\right]^{1/2}, \tag{2.73}$$

$$z = \left(\frac{4}{3\beta\sqrt{\pi}}\right)^{1/2} \frac{M_0^{3/4}}{F_0^{1/2}} \left[1 - \left(1 - \frac{F_0 t}{M_0}\right)^{3/2}\right]^{1/2}, \tag{2.74}$$

$$Q = M_0^{1/2} \left(\frac{4\beta\sqrt{\pi}}{3}\right) \frac{M_0^{3/4}}{F_0^{1/2}} \left(1 - \frac{F_0 t}{M_0}\right)^{1/2} \left[1 - \left(1 - \frac{F_0 t}{M_0}\right)^{3/2}\right]^{1/2} \tag{2.75}$$

$$M = M_0 - F_0 t, \tag{2.76}$$

in which $M_0 = \pi r_0^2 w_0^2$ is the momentum flux per unit mass at the source. Equations (2.73)-(2.76) were derived assuming a point source of flow; nevertheless, they could also be derived for any given source radius as shown in Appendix A.1. At the maximum height the momentum flux goes to zero, so

that from (2.76) we get the time taken to reach the maximum height as

$$t_{\max} = \frac{M_0}{F_0}. \tag{2.77}$$

Substituting equation (2.77) into (2.74) we get the maximum penetration height of the fountain:

$$z_{\max} = C_f \frac{M_0^{3/4}}{F_0^{1/2}}, \tag{2.78}$$

where $C_f = \left(\frac{4}{3\beta\sqrt{\pi}}\right)^{1/2} \approx 2.10$. The formula (2.78) is the same as (2.56) obtained by Turner (1966) through dimensional considerations.

Equation (2.78) may be rewritten in terms of the source Froude number, $\mathrm{Fr}_o = w_0/\sqrt{g' r_0}$, such that

$$z_{max} = C r_0 \mathrm{Fr}_o, \tag{2.79}$$

in which $C = \sqrt{8/(3\beta)} \approx 3.96$. As expected, equation (2.75) predicts that the volume flux decreases toward zero at the maximum height indicating a negative entrainment at the region where the fountain fluid begins to fall toward the source. This also means that there is a critical time when the volume flux is maximum. This critical time, t_c, can be explicitly calculated by differentiating equation (2.75) with respect to t and setting the resulting expression to zero to get

$$t_c = \frac{M_0}{F_0}\left[1 - \left(\frac{2}{5}\right)^{2/3}\right]. \tag{2.80}$$

Substituting t_c into (2.75) gives the maximum volume flux:

$$Q_{\max} = M_0^{1/2}\sqrt{\pi}\left(\frac{4\beta}{3\sqrt{\pi}}\right)^{1/2} \frac{M_0^{3/4}}{F_0^{1/2}} \left(\frac{3}{5}\right)^{1/2} \left(\frac{2}{5}\right)^{1/3}. \tag{2.81}$$

Before reaching the maximum height, conservation of buoyancy flux implies that the density of the fountain can be calculated at each height once the volume flux is known. $Q_0 g'_0 = Qg'$, hence

$$\rho = \rho_a - \frac{Q_0}{Q}(\rho_a - \rho_0). \tag{2.82}$$

However, since the volume flux reduces to zero at the maximum height, Q in equation (2.82) must be replaced by $Q_{\max}$ to calculate the density at the maximum height. This is because the density will remain unchanged from t_c to $t_{\max}$ due to the negative entrainment in this region.

Upon reaching the maximum height, the fountain reverses direction interacting with the incident flow. The interaction between these two opposing fluids inhibits the rise of the incident flow to the initial height and so it settles at a quasi steady-state height, z_{ss}. The theory above can not be used to predict the final height. However, experimental measurements show that $z_{ss} \approx 0.70 z_{\max}$ (Turner (1966)).

The return flow continues to fall while entraining fluid from the environment and the upward flow until it reaches the level of the source where it redirects from a vertical flow to a radial current. Before this work there were no experimental studies on these radial currents. However, it has been observed that the height of the radial currents is proportional to the maximum height (Baines *et al.* (1990)).

2.6.3 Fountains in two-layer fluid

In a two-layer fluid, the reverse flow of a fountain can either return to the level of the source or it can become trapped at the density interface. In the following, we discuss a theoretical procedure which may be used to predict the maximum penetration height of a turbulent fountain in two-layer stratified ambient.

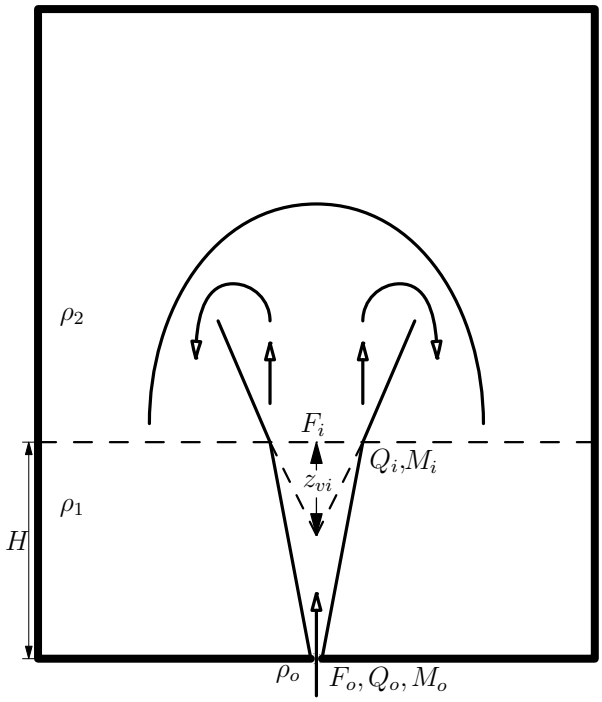

Figure 2.3: Schematic of a fountain in a two-layer ambient.

The maximum height in a two-layer ambient: Method 1

To obtain the maximum height in a two-layer ambient, we first calculate the centerline fluxes of the upward moving fluid at the interface using (2.73)-(2.76) (see figure 2.3). Then we calculate the buoyancy flux, F_i, of the fountain above the interface, using the approach of Noutsopoulos & Nanou (1986). Noutsopoulos & Nanou (1986) obtained the nominal value of the buoyancy flux above the interface as

$$F_i \;=\; \frac{1}{\rho_0}\int_A g(\rho_2-\rho)w\,\mathrm{d}A = g\frac{(\rho_1-\rho_0)}{\rho_0}Q_0 - g\frac{(\rho_1-\rho_2)}{\rho_0}Q_i.$$

This can be written as

$$F_i \;=\; F_0\left[1-\tilde{\varepsilon}\frac{Q_i}{Q_0}\right], \tag{2.83}$$

where $Q_i = \pi b_i^2 w_i$ is the volume flux, b_i is the radius and w_i is the velocity of the fountain at the interface, and $\tilde{\varepsilon} = (\rho_1-\rho_2)/(\rho_1-\rho_0)$. Finally, using F_i,

we calculate the depth of the virtual origin below the interface, z_{vi}, following the method of Morton (1959*b*). Morton (1959*b*) predicted the virtual origin from the source for a negatively buoyant forced plume to occur at

$$z_v = 10^{1/2}\gamma^{3/2}L_{Mo}\int_{1/\gamma}^{1}(1-\tau^5)^{-1/2}\tau^3\mathrm{d}t, \tag{2.84}$$

where

$$L_{Mo} = \frac{1}{(2^{3/2}\alpha^{1/2}\pi^{1/4}\lambda)}\frac{M_0^{3/4}}{|F_0|^{1/2}}, \quad \Gamma_0 = \frac{5\lambda^2}{4\alpha\pi^{1/2}}\frac{|F_0|Q_0^2}{M_0^{5/2}} \quad \text{and} \quad \gamma = (1-\Gamma_0)^{1/5}.$$

The entrainment constant is $\alpha = 0.085$ for fountains (Bloomfield & Kerr (2000)) and $\lambda = 1$ for top-hat profiles. This approach results in the following formula for the maximum height

$$z_{\max,2} = H + Cb_i\mathrm{Fr}_i - z_{vi}, \tag{2.85}$$

where $\mathrm{Fr}_i = w_i/\sqrt{g(\rho_2-\rho_i)b_i/\rho_0}$ is the Froude number at the interface, ρ_i is the density of the fountain at the interface, H is the distance of the source from the interface and C is the same as in (2.79).

The second and third terms in equation (2.85) estimate the maximum height of the fountain from the interface. If the fountain penetrates little beyond the interface, the second term may be less than z_{vi}. The best estimate for the maximum height in such a case should be $z_{max,2} \approx H$. The buoyancy flux above the interface may also be obtained as $F_i = g(\rho_2-\rho_i)Q_i/\rho_0$.

The procedure above assumes that the density difference between the layers is small and considers the fountain from the interface as one moving in a one-layer environment. The constant spreading assumption may therefore be used in this instance since the spreading rate of the fountain in the top layer as depicted in figure 2.3 is exaggerated only to illustrate the theoretical procedure. Our experiments show that the fountain penetrates the interface without a noticeable change in structure (see Section 3.2.2). An alternative method

of calculating $z_{max,2}$ without making a virtual origin correction is given in Appendix A.1.

In Chapter 3, we will also test the theoretical solution of Abraham (1963) who obtained the following approximate analytic solution for the penetration of a turbulent buoyant jet moving into an environment consisting of two layers of different densities:

$$z_{max,2} = \left(\frac{2}{5}\right)^{1/6} \left(\frac{3}{2} - \delta\tilde{F}\right)^{1/2} H, \tag{2.86}$$

in which $\tilde{F} = w_i^2/((\rho_i - \rho_2)gH/\rho_0)$ and the empirical constant $\delta \approx 0.8$ (Abraham (1963)). This derivation assumed Gaussian profiles of the flow quantities unlike the top-hat approach considered in this study. Similar to the one-layer case, the interaction of the incident and reverse flows inhibits the incident flow from reaching the maximum height and thus settles at a quasi steady-state height, $z_{ss,2}$. Unlike the one-layer case, the return flow may intrude on the interface or continue to the level of the source. Our experiments show that the ratio of the steady-state height to the maximum height depends on whether the return flow went back to the source or collapsed at the interface (see Section 3.3.2 where we have also compared our results with those of Bloomfield & Kerr (1998)).

The most significant factors governing these flow regimes are the relative density differences between the two layers and fountain and the maximum height relative to the height, H, of the layer at the source. Explicitly, the relative density differences are characterized by

$$\theta = \left|\frac{\rho_2 - \rho_1}{\rho_2 - \rho_0}\right|, \tag{2.87}$$

and the relative maximum height is characterized by z_{max}/H. In the case of a uniform ambient, $\rho_1 = \rho_2$ and hence $\theta = 0$. In this circumstance the fountain is always more dense than the ambient and must return to the source. The same circumstance is expected if $z_{max} < H$ since the fountain does not reach

the position of the interface.

If the source and ambient have the same density, $\rho_0 = \rho_1$ and hence $\theta = 1$. In this case the flow does not act like a fountain until impacting the second layer. Given that the jet penetrates the interface ($z_{max} > H$), the resulting fountain will be expected to return to spread along the interface since the fountain entrains less dense fluid from beyond the interface and therefore becomes lighter than the ambient fluid at the source. No experiments were conducted for this case, but the interested reader may refer to the studies by Shy (1995), Friedman & Katz (2000) and Lin & Linden (2005).

Irrespective of the regime that occurs, the flow goes on to spread as a radial gravity current either at the level of the source or at the interface.

2.7 Spreading velocities

In Sections (2.7.1)-(2.7.3), we derive a theory to analyse the velocities of the radially spreading gravity currents at the source and of the interfacial intrusions. We consider only the radial velocities at the width of the fountain where the return flow redirects from a vertical to a horizontal flow.

There are three cases to be considered. We first consider the theory for the spreading velocities of the currents at the source in the one-layer case and then extend it to examine source-spreading of fountains in two-layer fluids. The velocities of radial intrusions at the interface of a two-layer fluid is considered as a third case.

In Section (2.7.4) we derive a theory to analyse the initial velocities of the radial currents of plumes in linearly stratified environments.

2.7.1 Case 1: one-layer source-spreading

Figure 2.4a is a schematic showing the spreading of the currents at the source from a fountain in a one-layer environment. Baines *et al.* (1990) modelled the return flow of a turbulent fountain as an annular plane plume and obtained a

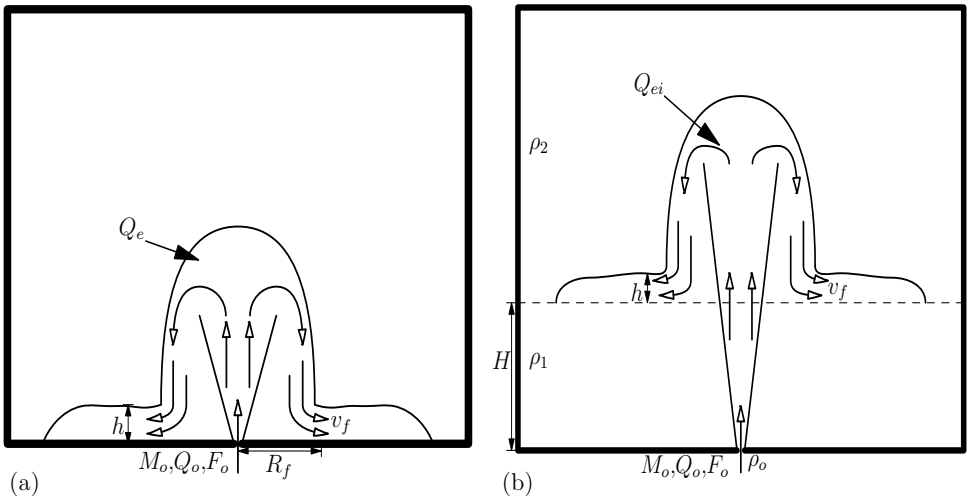

Figure 2.4: Schematics of (a) one-layer surface spreading currents, and (b) a model of the interfacial spreading currents.

formula for the total lateral entrainment into the reverse flow as

$$Q_e = B\frac{(z_{max} - z_v)}{r_o}Q_o, \tag{2.88}$$

where $B \approx 0.25$ was obtained empirically from experiments and z_v is the distance of the virtual origin below the source ($z_v \approx 0.8\,\text{cm}$ for our experiments). Thus, the total volume flux at the level of the source, just as the flow begins to spread outward is given by

$$Q_T = Q_e + Q_o. \tag{2.89}$$

If v_f is the initial spreading velocity at a radial distance $\mathcal{R}_f$, where $\mathcal{R}_f$ is the radius of the return flow at the source, and h is the corresponding height of the spreading layer just as the currents enter the ambient, then

$$Q_T = 2\pi\mathcal{R}_f h v_f. \tag{2.90}$$

Defining $g'_T = g(\rho_1 - \rho_s)/\rho_s$ to be the reduced gravity and ρ_s to be the initial density of the spreading layer at $r = \mathcal{R}_f$, dimensional analysis gives, for a

buoyancy-driven flow, a relationship of the form $v_f \propto \sqrt{g'_T h}$. Using (2.90) we get

$$v_f \propto \left(\frac{Q_T g'_T}{\mathcal{R}_f}\right)^{1/3}. \tag{2.91}$$

Mizushina *et al.* (1982) show that the radius of the whole fountain is approximately constant and is about 22% of the quasi-steady state height, z_{ss}. Just before the return flow begins to spread into the ambient, conservation of buoyancy flux in the fountain requires that at the level of the source

$$g'_T(Q_e + Q_o) \;=\; g'_e Q_e + g'_o Q_o.$$

By definition the reduced gravity of the environment, g'_e, is zero, hence

$$g'_T Q_T = F_o. \tag{2.92}$$

Thus, from (2.91) and (2.92) we get

$$v_f \;\propto\; \left(\frac{F_o}{\mathcal{R}_f}\right)^{1/3} \propto \left(\frac{F_o}{z_{ss}}\right)^{1/3}. \tag{2.93}$$

This formula may also be obtained via scaling analysis. By balancing the driving buoyancy force which scales as $g'_T \rho_s \mathcal{R} h^2$, and the retarding inertia force which scales as $\rho_s h \mathcal{R}^3/t^2$, Chen (1980) obtained the position of the front, $\mathcal{R}$, as a function of time, t, as $\mathcal{R}(t) = cF_o^{1/4} t^{3/4}$ where $c = 0.84$ was obtained as an experimental constant. Thus the velocity, V, is given by

$$V \;=\; \frac{\mathrm{d}\mathcal{R}}{\mathrm{d}t} = 0.59\left(\frac{F_o}{\mathcal{R}}\right)^{1/3}, \tag{2.94}$$

where the global volume conservation relation, $Q_T t = \pi \mathcal{R}^2 h$, has been employed. The same power law behaviour was also obtained by Britter (1979) by solving the governing equations of motion and obtained the experimental constant $c = 0.75$.

The scaling relationships above assume that the flow is a pure gravity current, its motion being dominated by buoyancy forces. In the presence of substantial radial momentum at the point where the flow enters the environment, dimensional analysis shows that at small times compared with the characteristic time scale $t_{MF} = M_{\mathcal{R}}/F_{\mathcal{R}}$ (in which $M_{\mathcal{R}}$ is the radial component of momentum flux per unit mass and $F_{\mathcal{R}}$ is the radial buoyancy flux per unit mass), the flow is dominated by momentum such that $\mathcal{R}(t) \sim M_{\mathcal{R}}^{1/4} t^{1/2}$ (Chen (1980)), so that

$$V \sim M_{\mathcal{R}}^{1/2}/\mathcal{R}. \tag{2.95}$$

The recent study by Kotsovinos (2000) for contant-flux axisymmetric intrusions into a linearly stratified ambient revealed a contant-velocity regime where $\mathcal{R} \sim t$. Kotsovinos (2000) argued that the additional force driving the flow in such cases is the initial radial momentum flux ($\rho_s M_{\mathcal{R}}$). Thus, balancing the kinematic momentum flux and the rate of change of the inertia force which scales as $\rho_s h\mathcal{R}^3/t^2$, gives $\mathcal{R}(t) \sim (M_{\mathcal{R}}/Q_T)t$, so that

$$V \sim M_{\mathcal{R}}/Q_T. \tag{2.96}$$

In theory, the relations in equations (2.93) and (2.94) correspond to larger times within the inertia-buoyancy regime when the flow is purely driven by buoyancy.

The radial component of momentum is unknown *a priori*. However, due to the loss in momentum by moving from a vertical flow to a radial current, we assume that the initial radial momentum flux, $M_{\mathcal{R}}$, is proportional to the momentum flux of the return flow at the level of the source, M_{ret}, defined as

$$M_{ret} = \pi(\mathcal{R}_f^2 - r_o^2)w_{ret}^2, \tag{2.97}$$

where w_{ret} is the velocity of the return flow at the level of the source. The results of Bloomfield & Kerr (2000) show that the reverse flow of the fountain

moving back toward the source first accelerates to some height before settling to an almost constant velocity close to the source. Their results also suggest that at the source, the velocity of the return flow is such that

$$w_{ret} \propto M_o^{-1/4} F_o^{1/2}. \tag{2.98}$$

In summary, if the radial momentum of the initial flow is substantial, then three regimes are theoretically possible. These are the radial-jet regime where $\mathcal{R} \sim t^{1/2}$, the constant-velocity regime where $\mathcal{R} \sim t$ and the inertia-buoyancy regime where $\mathcal{R} \sim t^{3/4}$. Thus, from (2.95), (2.96) and (2.93), and replacing $M_{\mathcal{R}}$ by M_{ret}, we get the following relations which may be used to predict the initial velocity of the spreading currents just as the flow begins to spread into the ambient:

$$V_{t \ll t_{MF}} \propto (M_{ret}^{1/2}/z_{ss}), \tag{2.99}$$

$$V_{t \approx t_{MF}} \propto (M_{ret}/Q_T), \tag{2.100}$$

$$V_{t \gg t_{MF}} \propto (F_o/z_{ss})^{1/3}. \tag{2.101}$$

However not all three regimes are necessarily present in a single experiment; the presence of a particular regime largely depends on the competing effects of the radial components of momentum and buoyancy in the flow (Chen (1980), Kotsovinos (2000)).

2.7.2 Case 2: two-layer surface-spreading

We consider the case where the return flow in the two-layer case returns to spread at the source as an axisymmetric current. In this case, there are two buoyancy fluxes involved in the system: the initial buoyancy flux, F_o, and the buoyancy flux after the fountain penetrates the density interface, F_i. The total volume flux of the spreading layer is given by the sum of the volume fluxes at

the source and the interface, and the flux entrained from the environment:

$$Q_{st} = Q_e + Q_o + Q_i,$$

where z_{max} in equation (2.88) is now replaced by $z_{max,2}$. The spreading layer will consist of a mixture of the source fluid and the fluid from the bottom and top layers. This mixture of fluid determines the reduced gravity of the spreading layer such that $g'_{ret}(Q_e + Q_o + Q_i) = g'_e Q_e + g'_o Q_o + g'_{bi} Q_i$ in which $g_{bi} = g(\rho_2 - \rho_i)/\rho_0$. This can be written as

$$g'_{ret} Q_{st} \quad = \quad F_o + F_i, \tag{2.102}$$

where $g'_{ret} = g(\rho_{st} - \rho_1)/\rho_{st}$ is the reduced gravity and ρ_{st} is the initial density of the spreading layer. Following the analyses in the one-layer case, we get the spreading velocity for a buoyancy-driven flow as

$$V_{t \gg t_{MF}} \propto \left(\frac{g'_{ret} Q_{st}}{z_{ss,2}} \right)^{1/3} \propto \left(\frac{F_o + F_i}{z_{ss,2}} \right)^{1/3}, \tag{2.103}$$

where $z_{ss,2}$ is the steady-state height in the two-layer case.

We assume that the velocity and momentum of the return flow at the level of the source are proportional to the corresponding velocity and momentum in the one-layer case where the ambient fluid is the first layer fluid. As such, if the initial radial momentum flux is substantial, then equations (2.99) and (2.100) may still be applied. By replacing $M_{\mathcal{R}}$ with M_{ret}, this argument results in the velocity relations for the radial-jet and constant-velocity regimes respectively as

$$V_{t \ll t_{MF}} \quad \propto \quad (M_{ret}^{1/2} / z_{ss,2}), \tag{2.104}$$

$$V_{t \approx t_{MF}} \quad \propto \quad (M_{ret} / Q_{st}). \tag{2.105}$$

2.7.3 Case 3: two-layer interfacial-spreading

Figure 2.4*b* is a schematic showing the radial spreading of gravity currents at the interface from a fountain in a two-layer environment. Experiments on axisymmetric intrusions into two-layer ambients from a source of constant volume flux are limited in the literature. Lister & Kerr (1989) have considered the case of the spreading of highly viscous fluid into a two-layer environment. They employed both scaling analysis and lubrication theory to analyse their results. Timothy (1977) considered the general case of a stratified flow into a stratified ambient and treated the two-layer case as a special circumstance. Most of his results were derived by extending the Bernoulli and hydrostatic equations for two-dimensional rectilinear flows to axisymmetric flows.

We show in Appendix B that by balancing the horizontal driving buoyancy force and the retarding inertia force for a buoyancy-driven flow, we obtain the relation for the radial velocity of the intrusion as

$$V \propto \left(\frac{\varepsilon g'_{in} Q_{in}}{\mathcal{R}}\right)^{1/3}, \tag{2.106}$$

where $\varepsilon = (\rho_2 - \rho_{in})/(\rho_2 - \rho_1)$. The reduced gravity of the intrusion in this case depends upon the parameter ε. If the density of the intrusion is equal to the density of the first layer fluid ($\rho_{in} = \rho_1$), then the one-layer relation (2.94) is retrieved from (2.106).

To model the case of the intrusions, we consider the fountain beyond the interface as though it is a one-layer system with the source conditions replaced by the conditions at the interface (see figure 2.4b). The volume flux entrained from the environment into the return flow is now given by:

$$Q_{ei} = B\frac{(z_{\max,2} - H - z_v)}{b_i} Q_i,$$

and the total volume flux into the spreading layer is given by the sum of the fluxes at the source and the interface, and the flux entrained from the

environment:

$$Q_{in} \;=\; Q_{ei} + Q_o + Q_i.$$

This mixture of fluid determines the reduced gravity of the interfacial intrusions. Assuming the conservation of buoyancy relation $\varepsilon g'_{in} Q_{in} = F_o + F_i$, we get the same proportionality relationship as in (2.103) although the proportionality constant is different:

$$V_{t \gg t_{MF}} \;\propto\; \left(\frac{F_o + F_i}{\mathcal{R}_f}\right)^{1/3} \propto \left(\frac{F_o + F_i}{z_{ss,2}}\right)^{1/3}. \tag{2.107}$$

In the presence of a substantial radial component of momentum, equations (2.99) and (2.100) may be applied with the initial source conditions replaced by the conditions at the interface. This gives the velocity formulas for the radial-jet and constant-velocity regimes respectively as

$$V_{t \ll t_{MF}} \;\propto\; M_{ret,i}^{1/2}/z_{ss,2}, \tag{2.108}$$

$$V_{t \approx t_{MF}} \;\propto\; M_{ret,i}/Q_{in}, \tag{2.109}$$

where $M_{ret,i}$ is the vertical momentum of the return flow at the interface and defined as $M_{ret,i} = \pi(\mathcal{R}_f^2 - b_i^2) w_{ret,i}^2$ with $w_{ret,i} \propto M_i^{-1/4} F_i^{1/2}$, where $w_{ret,i}$ is the velocity of the return flow at the interface.

2.7.4 Intrusion speeds in linearly stratified ambient

Upon reaching its neutral buoyancy level, a plume in a stratified fluid first overshoots this level and then falls back to spread radially as an intrusive gravity current. Such radial currents undergo different spreading regimes as they propagate outward (Chen (1980), Zatsepin & Shapiro (1982), Ivey & Blake (1985), Didden & Maxworthy (1982), Lister & Kerr (1989), Lemkert & Imberger (1993), Kotsovinos (2000)).

The relationship between the radius of the current, $\mathcal{R}(t)$, and time, t, is

predicted to be a power law of the form $\mathcal{R}(t) \sim t^{\kappa}$, where κ depends on the particular regime of flow. Four main regimes have been identified in the literature: a regime dominated by the radial momentum flux such that $\mathcal{R}(t) \sim t^{1/2}$, a constant velocity regime (Kotsovinos (2000)), the inertia-buoyancy regime where $\mathcal{R}(t) \sim t^{\kappa}$ (with $\kappa = 1/2$ by Ivey & Blake (1985), $\kappa = 2/3$ by Chen (1980), $\kappa = 3/4$ by Didden & Maxworthy (1982) and Kotsovinos (2000)), and finally the inertia-viscous regime where $\mathcal{R}(t) \sim t^{1/2}$. The reasons for the discrepancies in the inertia-buoyancy regime have been addressed in Kotsovinos (2000).

In this study, we measure the initial speeds of the radial currents that spread at the neutral buoyancy level and compare them with theory. We will focus on the first three regimes since we are interested only in the initial speeds. Explicitly, if $V = \mathrm{d}\mathcal{R}/\mathrm{d}t$ is the velocity of the intruding fluid, $M_{\mathcal{R}}$ the radial momentum flux and $Q_{\mathcal{R}}$ the radial volume flux, then compared to the time scale $t_{MF} = M_{\mathcal{R}}/F_{\mathcal{R}}$, we get

$$V \propto M_{\mathcal{R}}^{1/2}/\mathcal{R}, \quad t \ll t_{MF} \tag{2.110}$$

$$V \propto M_{\mathcal{R}}/Q_{\mathcal{R}}, \quad t \approx t_{MF} \tag{2.111}$$

$$V \propto \left(\frac{NQ_{\mathcal{R}}}{\mathcal{R}}\right)^{1/2}, \quad t \gg t_{MF} \tag{2.112}$$

where the proportionality constant in (2.112) has been found to be around 0.36 (Kotsovinos (2000)). Not all three regimes are necessarily present in a single experiment; the presence of a particular regime largely depends on the competing effects of the radial components of momentum and buoyancy in the flow (Chen (1980), Kotsovinos (2000), Ansong *et al.* (2008)).

The radial component of momentum is unknown *a priori*. However, owing to the loss in momentum by moving from a vertical flow to a radial current, we assume that the radial momentum and volume fluxes are proportional to the momentum and volume fluxes of the plume at the neutral buoyancy level (M_{n} and Q_{n} respectively). Thus, from (2.110)-(2.112) and replacing $M_{\mathcal{R}}$ and $Q_{\mathcal{R}}$ by M_n and Q_n, we obtain the expressions which may be used to predict the

initial velocity of the axisymmetric currents. The development of the theory above is similar to the approach used in Kotsovinos (2000) and Ansong *et al.* (2008).

2.8 Representation of axisymmetric internal gravity waves

The equations governing the motion of small amplitude axisymmetric internal gravity waves in an inviscid and incompressible fluid with no background flow can be reduced to a single equation in terms of the stream function $\psi(r, z, t)$ (see Appendix C):

$$\frac{\partial^2}{\partial t^2}\left[\frac{\partial^2 \psi}{\partial z^2} + \frac{\partial}{\partial r}\left(\frac{1}{r}\frac{\partial (r\psi)}{\partial r}\right)\right] + N^2 \frac{\partial}{\partial r}\left(\frac{1}{r}\frac{\partial (r\psi)}{\partial r}\right) = 0 \tag{2.113}$$

where the radial and vertical velocities are respectively defined by

$$u = -\frac{\partial \psi}{\partial z}, \quad w = \frac{1}{r}\frac{\partial (r\psi)}{\partial r}, \tag{2.114}$$

and r and z are the radial and vertical coordinates respectively. Seeking solutions of (2.113) that are periodic in z and t, we find for given vertical wavenumber, k_z, and frequency, ω, that the streamfunction satisfies

$$\psi(r, z, t) = \frac{1}{2} A_\psi J_1(kr) e^{i(k_z z - \omega t)} + cc \tag{2.115}$$

in which cc denotes the complex conjugate, J_1 is the Bessel function of the first kind and order one, and the radial wavenumber k is defined via the dispersion relation

$$\omega^2 = N^2 \frac{k^2}{k_z^2 + k^2}. \tag{2.116}$$

Field	Structure		Relation to vertical displacement	
Vertical displacement	ξ	$= \frac{1}{2}A_\xi J_0(kr)e^{i(k_z z-\omega t)} + cc$		
Streamfunction	ψ	$= \frac{1}{2}A_\psi J_1(kr)e^{i(k_z z-\omega t)} + cc$	A_ψ	$= -i\frac{\omega}{k}A_\xi$
Vertical velocity	w	$= \frac{1}{2}A_w J_0(kr)e^{i(k_z z-\omega t)} + cc$	A_w	$= -i\omega A_\xi$
Radial velocity	u	$= \frac{1}{2}A_u J_1(kr)e^{i(k_z z-\omega t)} + cc$	A_u	$= -\frac{k_z\omega}{k}A_\xi$
Pressure	p	$= \frac{1}{2}A_p J_0(kr)e^{i(k_z z-\omega t)} + cc$	A_p	$= i\rho_0\frac{\omega^2 k_z}{k^2}A_\xi$
N_t^2	N_t^2	$= \frac{1}{2}A_{N_t^2} J_0(kr)e^{i(k_z z-\omega t)} + cc$	$A_{N_t^2}$	$= -k_z\omega N^2 A_\xi$

Table 2.1: Polarization relations and representation of basic state fields for small-amplitude axisymmetric internal gravity waves in the (r, z) plane in stationary, linearly stratified Boussinesq fluid with no background flow. The table also shows the streamfunction and the time derivative of the perturbation squared buoyancy frequency (N_t^2). Each field b is characterized by the phase and magnitude of its complex amplitude, A_b, and the corresponding Bessel functions of the first kind are order zero (J_0) or one (J_1).

From equation (2.114) and the implicit definition of the vertical displacement, $w = \frac{\partial \xi}{\partial t}$, the vertical displacement field is represented by

$$\xi = \frac{1}{2}A_\xi J_0(kr)e^{i(k_z z-\omega t)} + cc,$$

where A_ξ is the amplitude of the vertical displacement field and J_0 is the Bessel function of the first kind and order zero. Table 2.1 shows the representation of other basic state fields in terms of Bessel functions for small-amplitude axisymmetric internal gravity waves.

In practice we Fourier-Bessel decompose the signal from horizontal time series for $0 \le r \le R$ and $T_1 \le t \le T_2$, and represent:

$$\xi(r, z, t) = \sum_n \sum_m \frac{1}{2}A_{\xi nm} J_0(k_n r)e^{i(k_z z-\omega_m t)} + cc, \tag{2.117}$$

where $A_{\xi nm}$ is the amplitude of the component of vertical displacement field with frequency $\omega_m = m\omega_0$ with $\omega_0 = 2\pi/(T_2 - T_1)$, radial 'wavenumber' $k_n = \alpha_n/R$ and α_n are the zeros of J_0. k_z is found in terms of k_n and ω_m using (2.116). We only include terms in the sum over m for which $\omega_m \le N$. Since the waves are assumed axisymmetric, we compute the time-averaged

total vertical energy flux, $F_{\text{wave}} = \int\int \langle wp \rangle \mathrm{d}A$, using Bessel series and get (see Appendix D)

$$F_{\text{wave}} = \frac{1}{4}\pi R^2 \rho_{00} N^3 \sum_n \sum_m \cos\Theta_m \sin 2\Theta_m \frac{|A_{\xi nm}|^2 J_1^2(\alpha_n)}{k_n}, \tag{2.118}$$

where p is pressure and Θ_m is the angle of propagation of each wave beam with respect to the vertical satisfying

$$\Theta_m = \cos^{-1}\left(\frac{\omega_m}{N}\right). \tag{2.119}$$

Chapter 3

Fountains impinging on a density interface: Experimental results

3.1 Introduction

This chapter presents an experimental study of an axisymmetric fountain impinging on a density interface in a two-layer stably-stratified environment. As in homogeneous environments, the fountain comes to rest at a maximum height and then reverses direction interacting with the incident flow. In a two-layer fluid, however, the reverse flow can either return to the level of the source or it can become trapped at the density interface. In either case the return flow then goes on to spread radially outward. We wish to develop a better understanding of the flow through measurements of maximum penetration height, quasi steady-state height and radial spreading rate.

There are few experimental studies on fountains in a two-layer environment. Kapoor & Jaluria (1993) considered a two-dimensional fountain in a two-layer thermally stratified ambient. They provided empirical formulas for the penetration depths in terms of a defined Richardson number.

Some have considered a jet directed into a two-layer ambient with the initial

density of the jet being the same as the density of the ambient at the source (Shy (1995); Friedman & Katz (2000) and Lin & Linden (2005)). Those jets only become negatively buoyant in the second layer.

Noutsopoulos & Nanou (1986), studied the upward discharge of a buoyant plume into a two-layer stratified ambient and used a stratification parameter that depended on the density differences in the flow to analyse their results.

One outstanding question concerns whether the reverse flow has a significant effect on the axial velocity and density. By measuring temperatures in a heated turbulent air jet discharged downward into an air environment, Seban *et al.* (1978) showed that the centerline temperatures and the penetration depth can be well predicted by theories which consider the downward flow alone. Mizushina *et al.* (1982) did a similar study of fountains by discharging cold water upward into an environment of heated water and found that the reverse flow had an effect on the axial velocity measurements. They attributed the difference in their result with those of Seban *et al.* (1978) to the enclosure used by Seban *et al.* (1978) in their experiments.

These experimental results have served only modestly to improve our understanding of the dynamics of the reverse flow. A theoretical study aimed at incorporating the reverse flow was first undertaken by McDougall (1981) who developed a set of entrainment equations quantifying the mixing that occurs in the whole fountain. The ideas developed in the model of McDougall (1981) have been built upon by Bloomfield & Kerr (2000) by considering an alternative formulation for the entrainment between the upflow and the downflow. Their results for the width of the whole fountain, the centerline velocity and temperature compared favourably with the experiments of Mizushina *et al.* (1982).

An important requirement for studying the dispersion of dense gases in the atmosphere is a knowledge of the distribution of the density as a function of space and time (Britter (1989)) and how fast the spreading pollutants are moving from a particular location. The usual approach to obtaining information on fluid densities in experiments is by extracting samples from the flow. This

is quite difficult and has led to the introduction of a relatively new approach of laser-induced fluorescence (LIF). This is however limited to unstratified environments due to problems with refractive index fluctuations (Daviero *et al.* (2001)). In this study, we do not take measurements of the densities of the spreading currents but we focus on taking measurements of the initial speeds of the radial currents as they spread from the area of impingement.

In Section 3.2, we describe the set-up of the laboratory experiments and the techniques used to visualize the experiments, and we present their qualitative analyses. In Section 3.3, quantitative results from the experiments are presented. We analyse the classification of the regimes of flow and compare the measured maximum penetration height and spreading velocities to theoretical predictions. In Section 3.4, we summarize the results.

3.2 Experimental set-up and analyses

3.2.1 Experimental set-up

Experiments were performed in an acrylic tank measuring 39.5 cm long by 39.5 cm wide by 39.5 cm high (see figure 3.1). The experiments were conducted by injecting less dense fluid downward into more dense ambient fluid, however, the direction of motion is immaterial to the equations governing their dynamics since the fluid is considered to be Boussinesq. A control experiment was conducted in a one-layer homogeneous environment and 48 experiments were conducted in two-layer fluid. In all experiments, the total depth of fluid within the tank was $H_T = 38\,\text{cm}$. The tank was filled to a depth of $H_T - H$ with fluid of density ρ_2, where $H = 0$ in the case of the one-layer experiment and $H = 5\,\text{cm}$ or $10\,\text{cm}$ in two-layer experiments. In two-layer experiments, a layer of fluid with density ρ_1 was added through a sponge float until the total depth was H_T. The variations in density were created using sodium chloride solutions. The typical interface thickness between the two layers was 1 cm, sufficiently small to be considered negligible. After the one or two-layer fluid

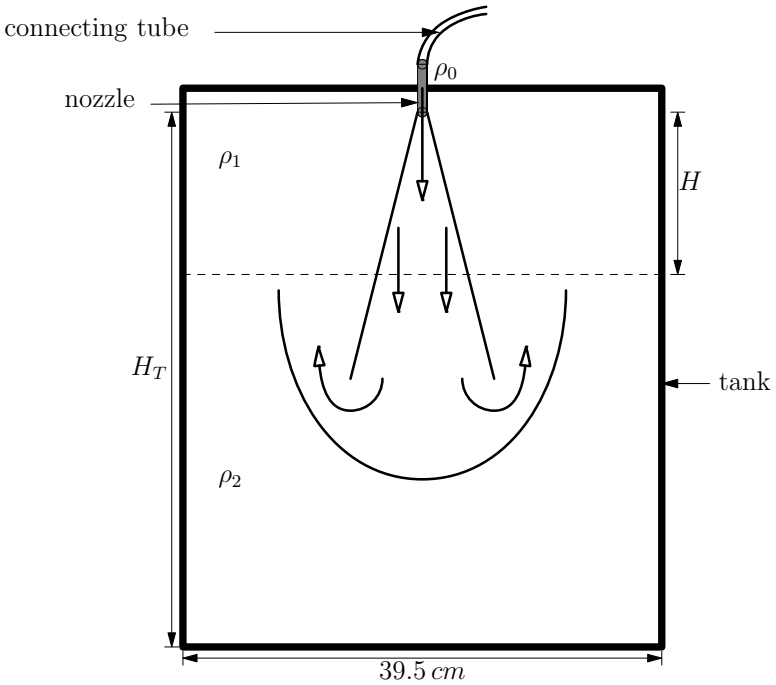

Figure 3.1: Experimental set-up and definition of parameters.

in the tank was established, a constant-head reservoir of fresh water of density ρ_o was dyed with a blue food colouring and then allowed to drain into the tank through a round nozzle of radius 0.2 cm. To ensure the flow turbulently leaves the nozzle, the nozzle was specially designed and fitted with a mesh having openings of extent 0.05 cm. The flow was assumed to leave at a uniform velocity across the diameter of the nozzle. The flow rates for the experiments were recorded using a flow meter connected to a plastic tubing, and by measuring the total volume released during an experiment. Flow rates ranged from 2.82 to 3.35 cm^3/s, and the Reynolds number of the experiments, defined as $R_e = w_0 D/\nu$, ranged from 896 to 1066, where ν is the kinematic viscosity of water.

Experiments were recorded using a digital camera situated 250 cm from the front of the tank. The camera was situated at a level parallel to the mid-depth of the tank and the entire tank was in its field of view. A fluorescent lighting apparatus was also placed about 10 cm behind the tank to illuminate

the system.

Using "DigImage" software, the maximum penetration depth of the fountain ($z_{\max}$), the quasi steady-state depth ($z_{\rm ss}$) and the initial velocity (w_o) were determined by taking vertical time-series constructed from vertical slices through the nozzle. The temporal resolution was as small as 1/30 s and the spatial resolution was about 0.1 cm.

Horizontal time series were used to determine the velocity of the resulting spreading currents. They were taken at a position immediately below the nozzle. Most time series are symmetrical about the position of the nozzle and only one side is used for the calculation of the velocities. Asymmetry in the time series may arise due to instabilities in the flow causing the front of the fountain at the maximum depth to tilt to one side. These experiments were excluded from the analyses.

3.2.2 Qualitative results

We present in this section the qualitative results of the laboratory experiments before giving detailed analyses of them. The snapshots from the experiments are flipped upside down for conceptual convenience and for consistency with the theory. We will first describe the results of the one-layer experiment before proceeding to the two-layer case.

One-layer experiment

Figures 3.2a-d show snapshots of the one-layer experiment which were taken 1, 3, 5, and 8 seconds, respectively, after the experiment started. The density difference between the fountain and the ambient fluid was $|\rho_o - \rho_1| = 0.0242\,\mathrm{g/cm^3}$ and the initial velocity was $w_o = 24.3\,\mathrm{cm/s}$. We observe the characteristic widening of the fountain as it entrains fluid from the surrounding homogeneous fluid. It reaches its maximum height at $t \sim 1\,\mathrm{s}$ (figure 3.2a), at which time the top of the fountain forms a pointed shape before collapsing back toward the source. The front then broadens and spreads outward as it returns

downward forming a curtain around the incident upward flow (figure 3.2b). The interaction of the return flow with the main upflow inhibits the rise of fluid from the source and causes the fountain to settle at a quasi-steady state height which is moderately below the maximum height. When the return flow reaches the level of the source it begins to spread radially outward (figure 3.2c). The spreading layer then propagates radially away from the source (figure 3.2d). The experiment is stopped before the spreading layer reaches the side walls of the tank.

Figure 3.3a shows the horizontal time series taken from this experiment, illustrating the spreading of the surface flow on both sides of the nozzle (situated at $x = 0\,\mathrm{cm}$). The parabolic nature of the time-series indicates the change in speed of the current as it moves away from the source.

Figure 3.3b shows the vertical time series taken for this experiment, and illustrates the positions of the maximum height, z_{max}, and the steady-state height, z_{ss}. The value of the ratio z_{ss}/z_{max} was found to be 0.74 for this experiment, comparable to the average value of 0.7 obtained by Turner (1966) in his experiments. The height of the spreading layer was observed to be almost constant as it spreads into the ambient (not shown), and was observed to be proportional to z_{max} (Baines *et al.* (1990)).

Two-layer experiments

In the presence of a two-layer ambient, the return flow of a fountain may go back to the level of the source or it may mix sufficiently with the second layer so that it goes back to the interface. In some circumstances it may do both. Here only snapshots for a situation leading to interfacial intrusions alone are shown.

Figures 3.4a-e show snapshots taken of a two-layer experiment 2, 5, 10, 20 and 25 seconds after the experiment was started. In this experiment, the density difference between the fountain and the ambient fluid at the source was $|\rho_o - \rho_1| = 0.001\,\mathrm{g/cm^3}$. The density difference between the two layers was $|\rho_1 - \rho_2| = 0.0012\,\mathrm{g/cm^3}$. The initial velocity was $w_o = 23.9\,\mathrm{cm/s}$ and

$H = 5\,\text{cm}$. When the experiment begins, the fountain again increases in width as it entrains fluid from the surrounding ambient. It impinges upon the interface at $z = 5\,\text{cm}$ and penetrates through without noticeable change in structure (figure 3.4a).

After reaching the maximum height, the front of the fountain starts to broaden as more fluid is supplied from the source (figure 3.4b). It then returns downward, due to its buoyancy excess, and collapses around the incident flow, similar to its behaviour in the one-layer case.

In this circumstance, however, the return flow gets trapped at the interface and does not return to the source (figure 3.4c). At first the return flow overshoots the height of the interface around the axis of the fountain before rising back to spread radially along the interface. The degree of overshoot is more or less pronounced, depending upon the experimental conditions. The process continues in a quasi-steady state (figure 3.4d). The spreading layer is observed to be thicker around the axis of the fountain and gradually reduces in thickness away from the axis (figure 3.4e).

Horizontal and vertical time series from this experiment are shown in figures 3.5a and 3.5b respectively. The former shows an intrusion moving with almost uniform radial speed toward the side walls of the tank. The time series is also observed to be symmetric about the source (situated at $x = 0\,\text{cm}$). The measured positions of the maximum and steady-state heights are indicated on the vertical time series. Compared to the one-layer case, the average steady-state height is almost equal to the maximum height. This occurs because the return flow of the fountain intruded on the interface. So the distance over which the incident and return flows interact is reduced, thereby increasing the steady-state height.

3.3 Quantitative analyses

In this section, we quantitatively analyse the experimental results and compare them with theoretical predictions. The main aim is to characterize the various

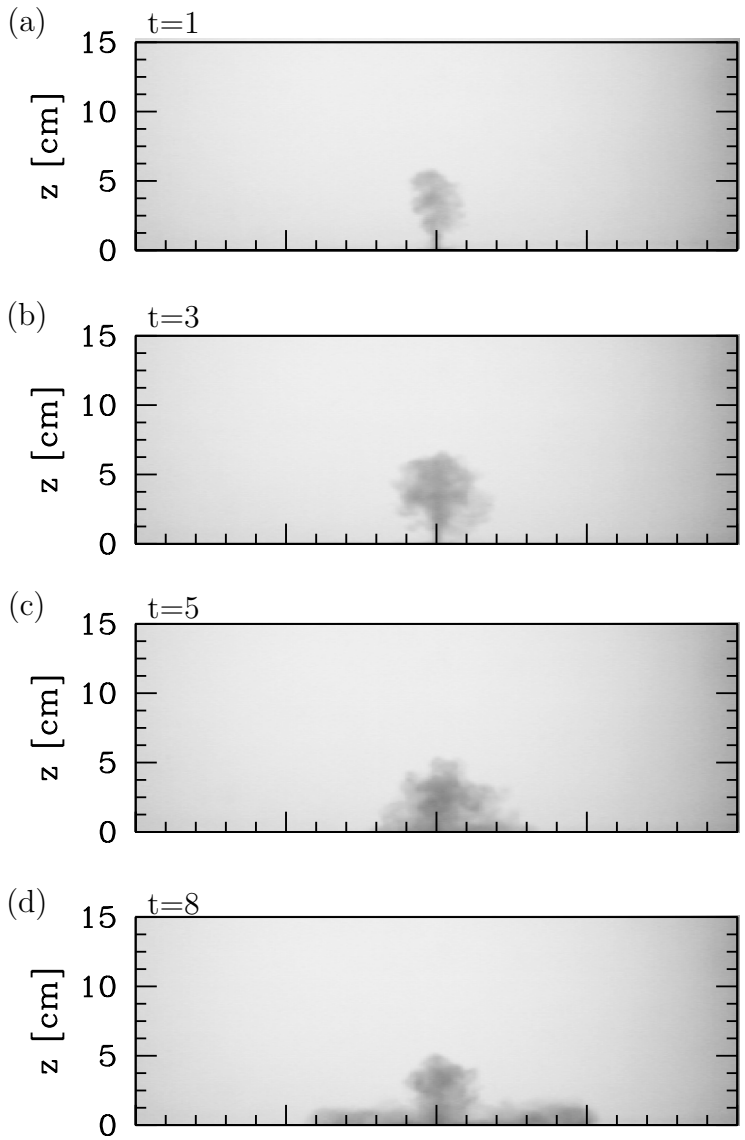

Figure 3.2: Snapshots of the one-layer experiment taken at (*a*) $t = 1\,\mathrm{s}$; (*b*) $3\,\mathrm{s}$; (*c*) $5\,\mathrm{s}$; (*d*) $8\,\mathrm{s}$. The images have been flipped vertically for conceptual convenience.

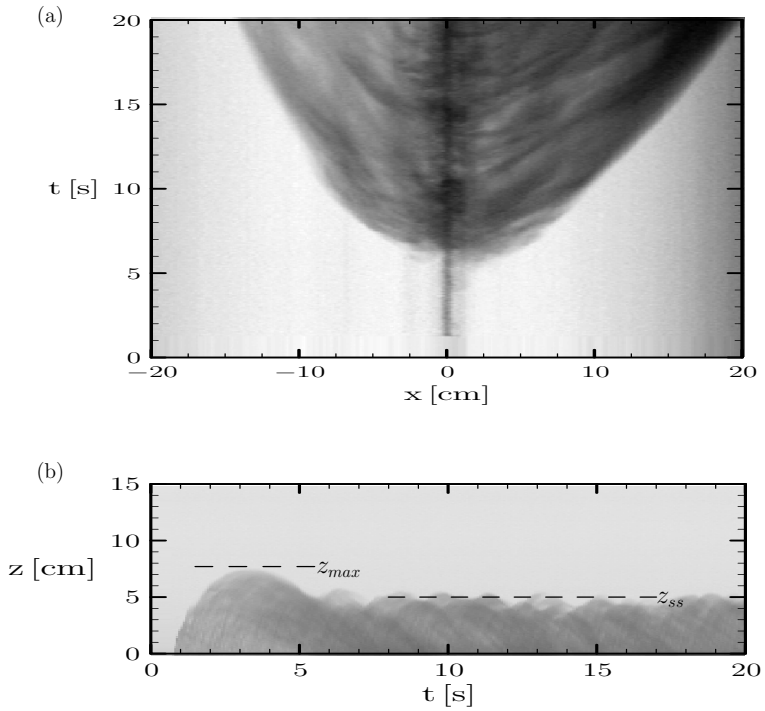

Figure 3.3: (a) Horizontal and (b) vertical time series for a 1-layer experiment. The horizontal time series is constructed from a slice taken at $z = 0\,\mathrm{cm}$. The vertical time series is taken from a vertical slice through the source at $x = 0\,\mathrm{cm}$.

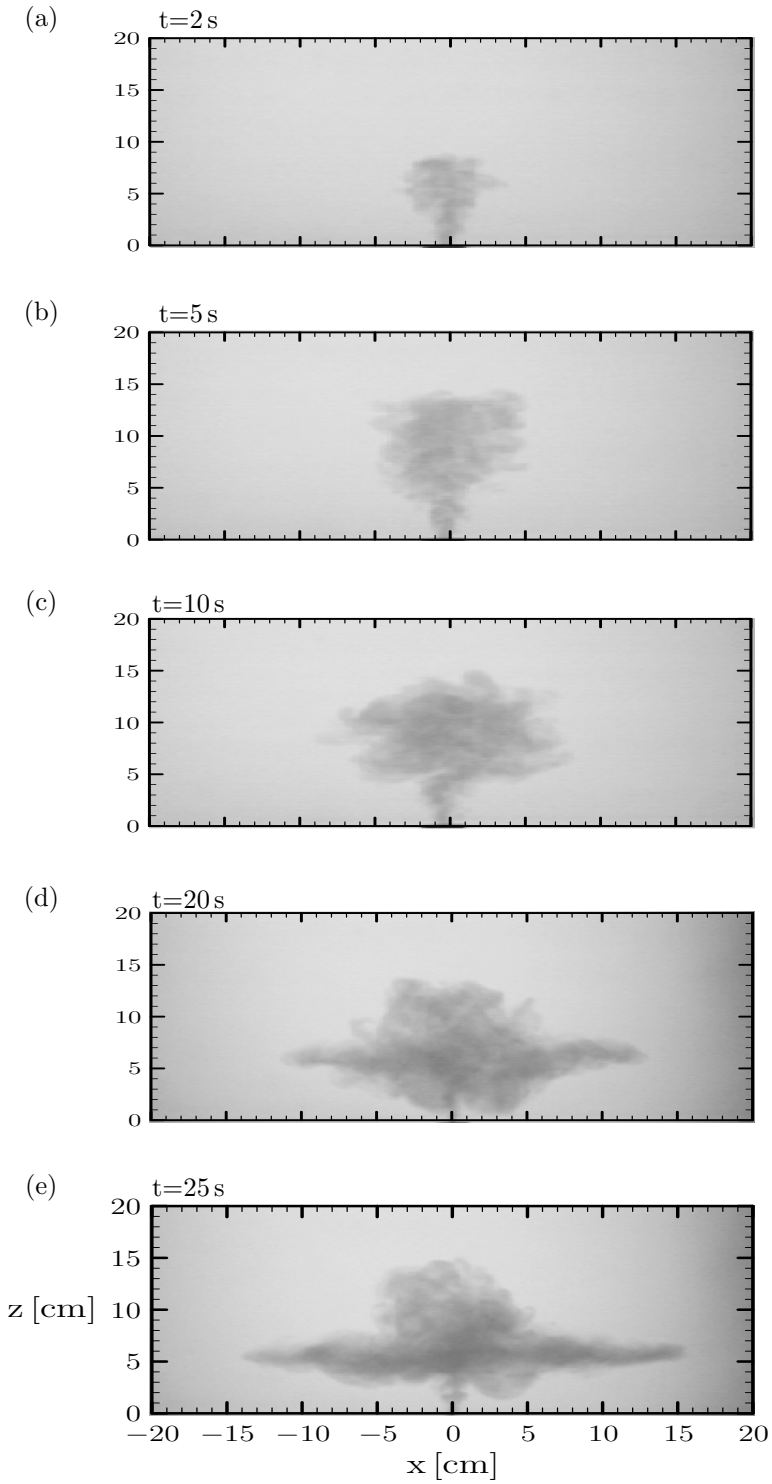

Figure 3.4: As in figure 3.2 but for snapshots of a two-layer experiment.

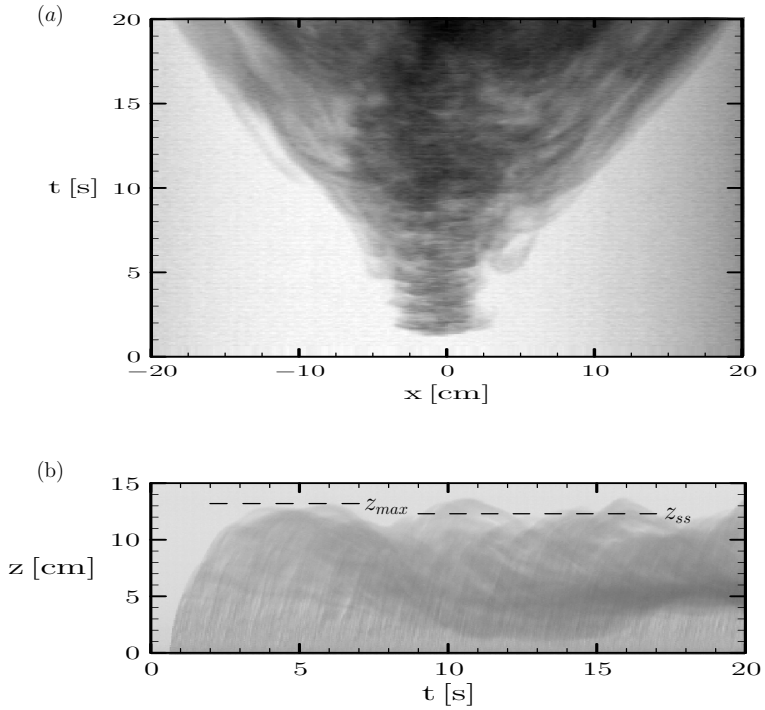

Figure 3.5: As in figure 3.3 but for (a) horizontal and (b) vertical time series for a 2-layer experiment.

regimes of flow, to quantify the maximum penetration height in the two-layer ambient flow and to analyse the radial velocity of the resulting axisymmetric currents and intrusions.

3.3.1 Regime characterization

The three regimes of flow observed in the experiments: in regime S, the return flow penetrates the interface but returns downward to the source; in regime I, the return flow intrudes at the interface; in regime B, a combination of both occurs.

To classify the regimes of flow, we first considered an approach used by Bloomfield & Kerr (1998) to determine whether a fountain in a linearly stratified environment will spread at an intermediate level or spread at the source. In their method, the density of the fountain at the maximum height was first calculated and the height in the environment where fluid with this density would intrude was used as an estimate of the spreading height. To compare our results to those of Bloomfield & Kerr (1998), we calculated the density of the fountain at the maximum height, ρ_{max}, and compared it to the density in the first layer. In figure 3.6a we have plotted ρ_{max} against the density ρ_1. If ρ_{max} is larger (smaller, for fountains directed downward) than ρ_1, it is expected that the fountain will spread at the source. The experimental results show that this approach only gives a moderate classification of the regimes in the two-layer stratified case. About 28% of the intrusions fell below the solid line in figure 3.6a, predominantly for $H = 10\,\text{cm}$ cases. This suggests that it is possible to have sufficient mixing in the return flow by the time it gets to the interface, leading to interfacial intrusions. So a straightforward application of the diagnostic of Bloomfield & Kerr (1998) is inappropriate for two layer fluids because it does not account for the height of the interface, H.

A second classification of the regimes is shown in figure 3.6b where we have plotted the relative density differences $\theta = (\rho_2 - \rho_1)/(\rho_2 - \rho_o)$ against the relative maximum height z_{max}/H.

If $\theta \gtrsim 0.15$, figure 3.6b shows that intrusions form if $z_{max} \gtrsim 2H$. In which case the return flow entrains substantially less dense fluid from beyond the interface, making it lighter than the lower layer fluid.

If $\theta \lesssim 0.15$, the return flow reaches the source independent of the relative maximum height. In this case the return flow also entrains less dense fluid from beyond the interface but it is still heavier than the lower layer fluid by the time it gets to the interface. Likewise if $z_{max} \lesssim 2H$ the return flow always reaches the source because it is not sufficiently diluted by the ambient beyond the interface.

There were two experiments which resulted in regime B. They occurred for experiments with $z_{max} \approx 2H$. In these cases, the outer part of the return flow entrains more of the less dense fluid from beyond the interface than the inner part. The lighter outer part then begins to spread radially at the interface while the heavier inner part continues to fall to the source. The amount of fluid that intrudes at the interface may sometimes be smaller than the fluid that continues to the source.

The empirical function used to separate the intrusion and source outflow regimes is given by

$$\theta = 0.15 + \frac{1}{50(z_{max}/H - 1.5)^3}. \tag{3.1}$$

This is plotted as the dashed line in figure 3.6b.

The second method of classification is therefore better for two-layer stratified fluids as clearly shown in figure 3.6b. We note that all parameters in (3.1), including z_{max} are determined from the source conditions (see equation 2.78). Conversely, ρ_{max} in the first method requires calculation of the axial parameters at the interface.

3.3.2 Maximum height

Figure 3.7a plots the experimentally measured values of $z_{max,2}$ and compares them with the theoretical prediction given by equation (2.85). There is good

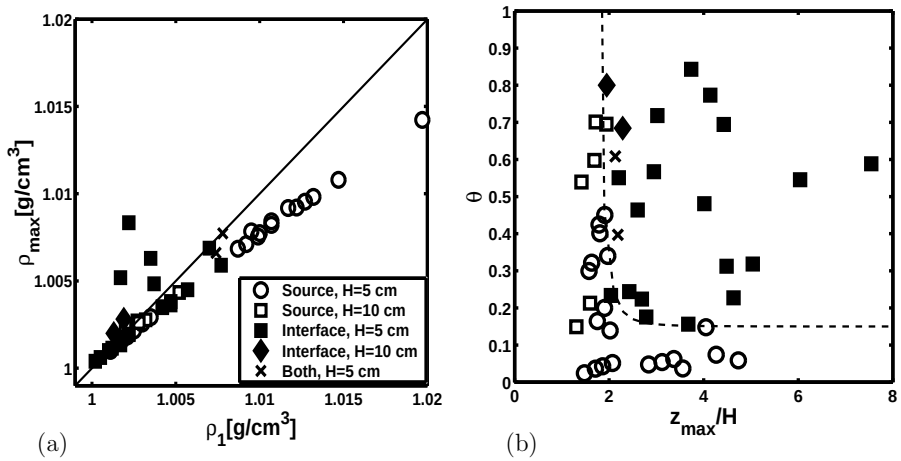

Figure 3.6: (a) Regime diagram following the method of Bloomfield & Kerr (1998); showing circumstances under which the return flow of a fountain spreads at the level of the source (open symbols), at the interface (closed symbols) or both. The solid line is expected to separate the open symbols from the closed symbols. (b) Regime diagram following our approach; the symbols are as in figure 3.6a. The dotted line represents an empirical formula that separates the two regimes and given by equation (3.1).

agreement in the data with a correlation of about 96%. The results also compare well with the theoretical prediction of Abraham (1963) (see equation (2.86)).

Figure 3.7b plots the ratio $z_{ss,2}/z_{max,2}$ against the source Froude number Fr_o. If $\theta < 0.15$, the average value of the ratio was found to be 0.74, which is comparable to the one-layer case. For the experiments with $\theta > 0.15$ and $z_{max} > 2H$ in which case the return flow intruded along the interface, the average value was 0.88. This occurs because the return flow penetrates little beyond the interface and so there is less interaction between the return and incident flows. If $\theta > 0.15$ and $z_{max} < 2H$, the average value was found to be 0.80, in this case the fountain penetrated little into the second layer.

Results of the ratio $z_{ss,2}/z_{max,2}$ are comparable to the findings of Bloomfield & Kerr (1998) for a fountain in a linearly stratified fluid where the average value of the ratio was found to be 0.93, also larger than the value 0.70 for a fountain in a uniform ambient. This value is a moderately higher than

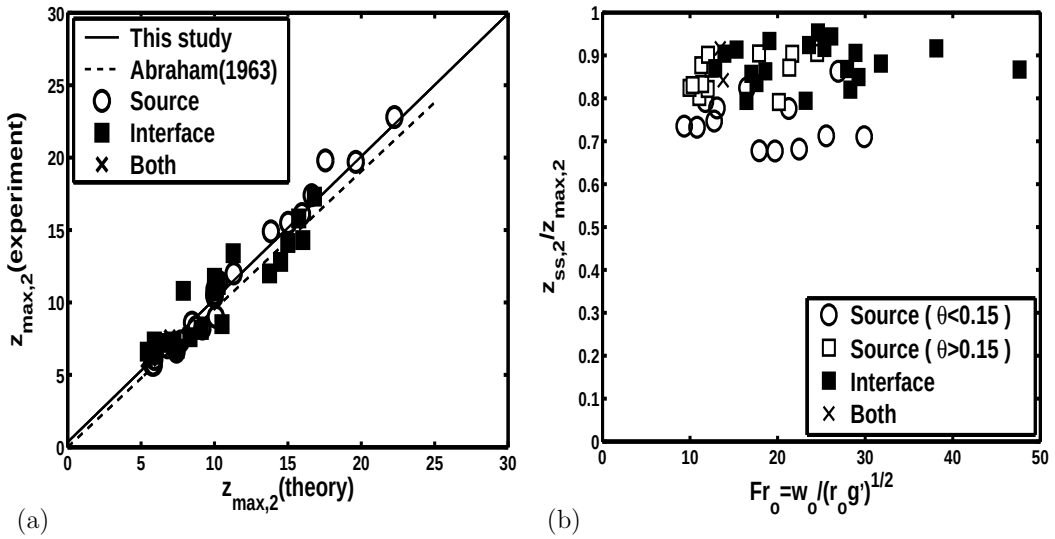

(a) (b)

Figure 3.7: (a) The maximum penetration height and (b) the ratio of the steady-state height to the maximum height

our value of 0.88 for interfacial intrusions. This is probably because in the case of linearly stratified fluids, the fountain could intrude at intermediate heights which are higher than the equivalent heights of the two-layer interface. This means that, effectively, the distance over which the upflow and downflow interact is even shorter in a linearly stratified ambient, leading to a higher value of the ratio.

3.3.3 Radial source and intrusion speeds

We measured the initial velocity of the radially spreading currents by taking the slope near $x \approx R_f$ of horizontal time series as shown, for example, in figure 3.8.

Measurements of the time and distance from the horizontal time series determined how the position of the front scales with time near $x = R_f$. Figure 3.9 shows some typical log-log plots of distance against time used to determine the scaling relationship. The experiments showed steady state ($R \sim t$) and inertia-buoyancy ($R \sim t^{3/4}$) regimes in the flow.

To gain a better understanding of the starting flow regimes, we defined a critical Froude number to characterize the competing effects of momentum and buoyancy in the return flow at the point of entry of the current into the ambient. In the case of the flows that returned to the source, the Froude number is defined by

$$\mathrm{Fr}_s = w_{ret}/(g'_{ret} z_{max,2})^{1/2}, \tag{3.2}$$

where $g'_{ret} = (F_o + F_i)/Q_{st}$ is the reduced gravity defined in 2.102. In the case of the interfacial flows, the Froude number is similarly defined by

$$\mathrm{Fr}_i = w_{ret,i}/(g'_{ret,i} z_{max,2})^{1/2}, \tag{3.3}$$

where $g'_{ret,i}$ is the reduced gravity of the return flow at the interface. Figure (3.10) gives an approximate classification of these regimes. It shows that the power law relation $R \sim t^{\kappa}$ with $\kappa \approx 0.75$ occurs for smaller values of the Froude number ($\mathrm{Fr}_s < 0.25$ and $\mathrm{Fr}_i < 0.4$). In this case, the initial flow is purely driven by buoyancy forces while for larger values of the Froude number ($\mathrm{Fr}_s > 0.25$ and $\mathrm{Fr}_i > 0.4$), both momentum and buoyancy play a role in the initial flow, giving rise to a power law exponent $\kappa \approx 1.0$.

If instabilities develop in the flow to cause the fountain to tilt initially to one side of its vertical axis, then these scaling relationships may be violated. This was also observed to occur if, in the case of the intrusions, there was a very strong overshoot of the return flow before rising back to spread along the interface. The velocity data that were used to determine the experimental constants in the theory do not include those experiments.

Source-spreading speeds

Figures 3.11a and 3.11b plots the measured speeds of the radially propagating currents at the source compared with the theoretical estimates of equations (2.103) and (2.105). We see that there is fairly good agreement between the

theory and the measurement. The theoretical equations for these two regimes then become

$$V_{t\approx t_{MF}} = (4.10 \pm 0.14)\left(\frac{M_{ret}}{Q_{st}}\right), \tag{3.4}$$

and

$$V_{t\gg t_{MF}} = (0.84 \pm 0.14)\left(\frac{F_o + F_i}{z_{ss,2}}\right)^{1/3}. \tag{3.5}$$

The regimes of flow in this case are the constant-velocity regime ($R \sim t^{\kappa}$ with $\kappa = 1.0 \pm 0.10$) and the inertia-buoyancy regime ($\kappa = 0.75 \pm 0.04$).

Intrusion speeds

Figure 3.12 plots the measured intrusion speeds against the theoretical estimates of equations (2.107) and (2.109). The theoretical equations for these two regimes then become

$$V_{t\approx t_{MF}} = (0.77 \pm 0.15)\left(\frac{M_{ret,i}}{Q_T}\right), \tag{3.6}$$

and

$$V_{t\gg t_{MF}} = (0.17 \pm 0.09)\left(\frac{F_o + F_i}{z_{ss,2}}\right)^{1/3}. \tag{3.7}$$

The regimes of flow in this case are the constant-velocity regime ($\kappa = 1.0 \pm 0.09$) and the inertia-buoyancy regime ($\kappa = 0.75 \pm 0.07$).

3.4 Conclusions

This chapter classified the regimes of flow that result when an axisymmetric turbulent fountain is discharged into a two-layer ambient. The classification was done using the empirically determined parameter, $\theta = (\rho_2 - \rho_1)/(\rho_2 - \rho_o)$, and the relative maximum height, z_{max}/H. The results show that if $z_{max} \lesssim$

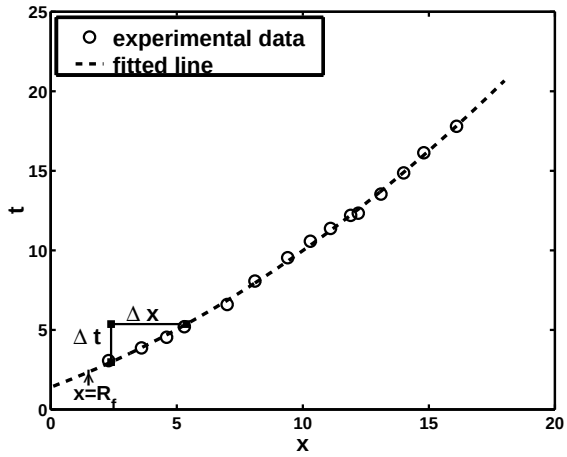

Figure 3.8: Typical approach of calculating the initial spreading speeds with $\Delta x \approx R_f$ (experiment with $|\rho_1 - \rho_o| = 0.0202$, $|\rho_2 - \rho_1| = 0.0005$, $H = 5\,\mathrm{cm}$, $w_o = 26.26\,\mathrm{cm/s}$).

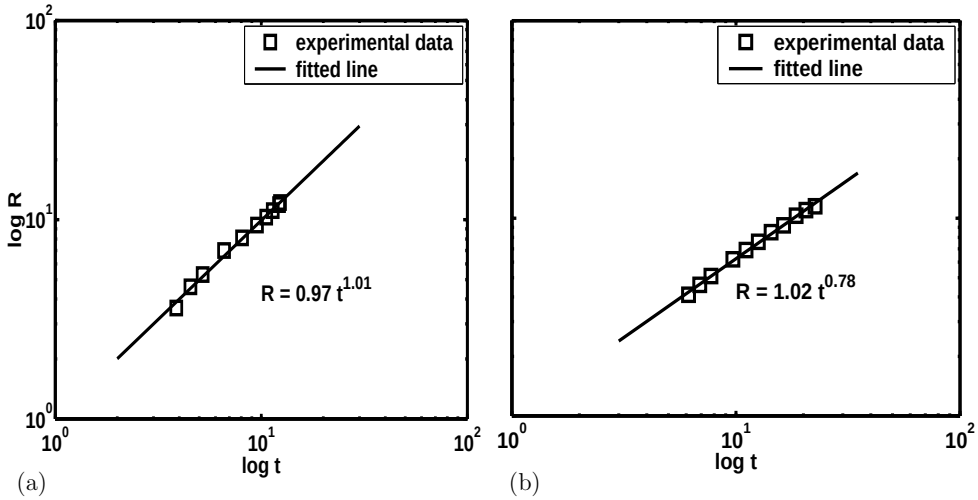

Figure 3.9: Typical initial growth relationships between the radial distance and time, indicating (a) $R \sim t$ (experiment with $|\rho_1 - \rho_o| = 0.0022$, $|\rho_2 - \rho_1| = 0.005$, $H = 5\,\mathrm{cm}$, $w_o = 25.95\,\mathrm{cm/s}$), and (b) $R \sim t^{3/4}$ (experiment with $|\rho_1 - \rho_o| = 0.0202$, $|\rho_2 - \rho_1| = 0.0005$, $H = 5\,\mathrm{cm}$, and $w_o = 26.26\,\mathrm{cm/s}$)

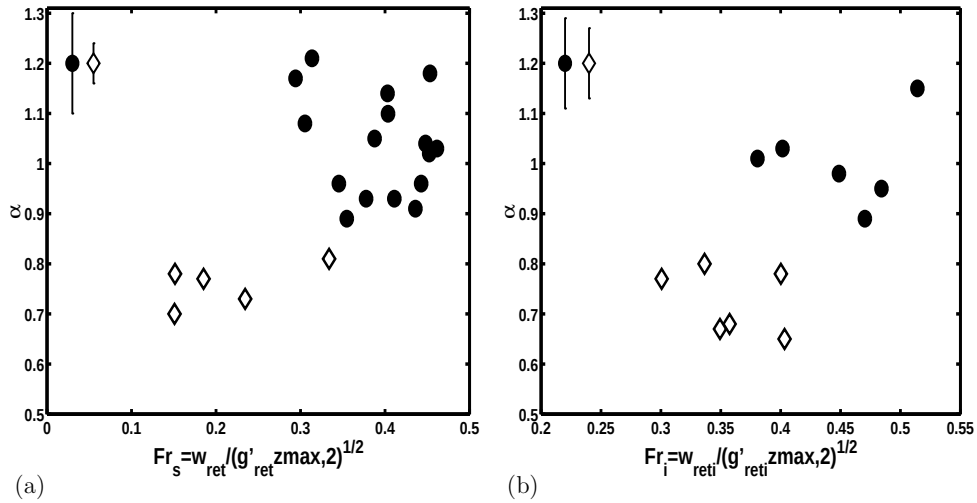

(a) (b)

Figure 3.10: Characterizing the initial power law behaviour, $R \sim t^{\kappa}$, using a defined radial Froude number for the (a) surface flows, and (b) interfacial flows. The open diamond ($\Diamond$) refers to $\kappa \approx 0.75$ and the closed circles ($\bullet$) refers to $\kappa \approx 1$. Typical errors are indicated in the top left corner of both plots.

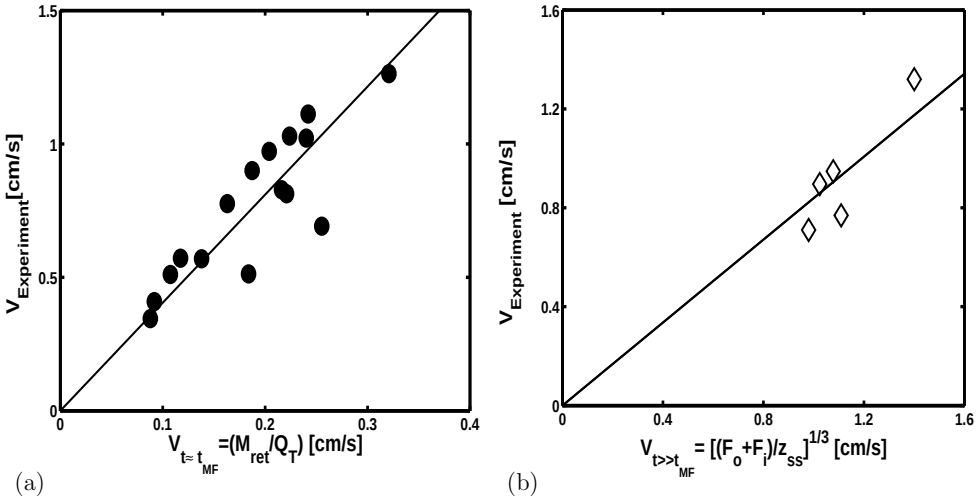

(a) (b)

Figure 3.11: Radial initial surface spreading velocities for (a) $R \sim t$, and (b) $R \sim t^{3/4}$

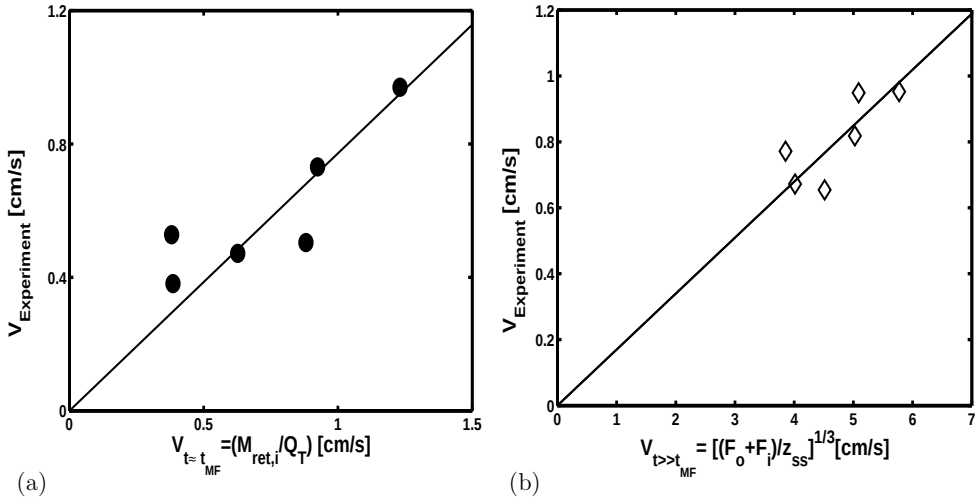

Figure 3.12: Radial initial intrusion velocities for (a) $R \sim t$, and (b) $R \sim t^{3/4}$

$2H$, the return flow will go back to the source irrespective of the value of θ. However, if $z_{max} \gtrsim 2H$, the return flow will collapse and spread radially at the interface if $\theta \gtrsim 0.15$.

There was good agreement between theory and experiment for the maximum vertical penetration height. In the case of flows that returned to the source, the ratio of the quasi-steady state height to the maximum height, $z_{ss,2}/z_{max,2}$, was found to depend on whether the return flow went back to the source or collapsed at the interface. The ratio is closer to unity ($z_{ss,2}/z_{max,2} \approx 1.0$) for intrusions because the return flow does not so effectively retard the incident flow near the source.

Radial currents that result from the return flow of a fountain spreading at the source or interface either at constant-velocity (being driven by both the radial components of momentum and buoyancy) or spreading as $R \sim t^{3/4}$ (being driven by buoyancy forces alone). These regimes are distinguished by a critical Froude number $\mathrm{Fr}_s \approx 0.25$ or $\mathrm{Fr}_i \approx 0.4$.

Chapter 4

Internal gravity waves generated by convective plumes: Experimental results

4.1 Introduction

This chapter examines the axisymmetric internal gravity waves generated by turbulent buoyant plumes in linearly stratified environments. The principal goal is to determine the fraction of the energy flux associated with the plume at the neutral buoyancy level that is extracted by the waves.

One of the first experimental studies designed to investigate the nature of internal gravity waves generated by a thermal (an instantaneous release of a buoyant volume of fluid) was by McLaren *et al.* (1973). The wave field was analysed by studying the trajectories of buoyant marker particles placed in the linearly stratified ambient. It was observed that the waves generated by buoyantly rising fluid at its neutral buoyancy level were transient in nature and had a band of frequencies unlike the waves generated in their experiments using an oscillating solid sphere which had a single frequency. The study did not however investigate the energy extracted by the waves from the buoyant element at its stabilizing level.

An experimental study of the energy lost to waves from a thermal was undertaken by Cerasoli (1978). The energy of the internal gravity waves propagating away from the collapse region was estimated by comparing the difference between the initial and final potential energy of the mean state. The energy estimated in this way was found to be 20 to 25% of the change in potential energy of the whole system.

A recent numerical study has also investigated the generation of gravity waves by thermals via the mechanical oscillator mechanism (Lane (2008)). The study concluded that in a stable ambient fluid, the deceleration and subsequent collapse of a thermal after reaching its neutral buoyancy level is due to a vortical response of the ambient to the overshooting thermal which induces an opposing circulation that inhibits further ascent of the thermal. The response of the ambient vorticity was proposed as being responsible for the thermal acting like a damped mechanical oscillator thereby resulting in the generation of the gravity waves.

A theoretical investigation to understand the significance of the energy extracted from a convective element by gravity waves was undertaken by Stull (1976). He modeled penetrative convection as an idealized Gaussian disturbance at the base of a temperature inversion and found that penetrative convection overshooting into a stable temperature inversion from a turbulent mixed layer can excite vertically propagating internal gravity waves in the stable air above the inversion base. He concluded that the amount of energy lost in this way was small if the inversion was strong. However, if the inversion was weak and the convective mixing vigorous, a significant fraction of the energy of the overshooting elements was lost. The inclusion of the inversion layer in the model permitted the propagation of interfacial waves. In the absence of a temperature jump, the theory estimates the maximum amount of energy lost to waves to be about 68 %.

Other studies have examined the internal waves generated due to the motions in a convective layer underlying a stable layer of fluid (Townsend (1964, 1965, 1966); Michaelian *et al.* (2002)). In particular, Townsend (1964) per-

formed experiments in which fresh water in a tank was cooled to freezing point from below and gently heated from above. The nonlinear relationship between the density of water and temperature resulted in convective motions in the lower layer and the excitation of transient internal gravity waves in the stratified layer above. The rising convective motions were observed to be plume-like rather than spherical thermals and the internal waves were generated due to the penetration of these columnar motions into the stable layer. Michaelian *et al.* (2002) studied the coupling between internal waves and the convective motions in a mixed layer. The convective plumes were initially observed to be vertical and resulted in the generation of high frequency waves, but as the mixed layer grew low frequency waves were generated giving rise to a weak mean flow which in turn modified the plumes from being vertical to being horizontal.

Previous experimental studies on the generation of internal gravity waves by oscillating bodies used rigid sources such as cylinders and spheres (Mowbray & Rarity (1967a); Sutherland *et al.* (1999); Sutherland & Linden (2002); Flynn *et al.* (2003)). In these experiments, a linearly salt-stratified fluid was mechanically forced at a fixed frequency. This resulted in the generation of purely monochromatic waves with phases at a fixed angle to the vertical propagating away from the source region. These idealized experiments helped in the interpretation of the theoretical morphology of the waves.

In this study, we generate axisymmetric internal gravity waves using turbulent buoyant plumes instead of solid objects. This is because the source is fluidic and the vertical fluctuations at the top of the plume may be used to roughly mimic the vertical excursions of updrafts and downdrafts within a convective storm.

In Section 4.2, we discuss the experimental procedure and provide qualitative results. Quantitative results are presented in Section 4.3. In Section 4.4 we discuss how the results may be extended to geophysical circumstances and summarize our results in Section 4.5.

4.2 Experimental set-up and analyses

4.2.1 Experimental set-up

Experiments were performed in an acrylic tank measuring 39.5 cm long by 39.5 cm wide by 39.5 cm high (see figure 4.1). These were conducted by injecting dense fluid downward into an initially less dense ambient fluid. The results are dynamically equivalent to injecting light fluid upward from the bottom because the system is Boussinesq. The qualitative results are presented in this section for experiments with and without a uniform-density surface layer. For conceptual convenience and for consistency with the theory presented in Section 2.2, the snapshots from the experiments are flipped upside down so that the plume appears to rise upward.

In all experiments, the total depth of fluid within the tank was $H_T = 38$ cm. In the absence of a uniform-density layer, a linear stratification is set up using the double-bucket technique (Oster (1965)). In the presence of a mixed-layer of depth $z = H$, the tank was first filled to a depth $H_T - H$ with fluid whose density increases linearly with depth. Once this height was attained, the flow of fresh water into the salt-water bucket was stopped while the flow from the salt-water bucket into the tank was allowed to continue at the same flow rate. This approach ensured that no density jump was created between the linearly-stratified layer and the uniform-density layer. The variations in density were created using sodium chloride solutions and density samples were measured using the Anton Paar DMA 4500 density meter. The density profile in the environment was determined by withdrawing samples from different vertical levels in the tank and by using a vertically traversing conductivity probe (Precision Measurement Engineering). The depth of the mixed layer was varied such that $H \approx 5$, 10 or 15 cm. Figure 4.1(a) shows a schematic of the density variation in the ambient for the case with a mixed layer with $\rho_1 < \rho_2$ where ρ_1 is the density of the mixed layer and ρ_2 is the density at the bottom of the stratified layer.

After the ambient fluid in the tank was established, a reservoir of salt

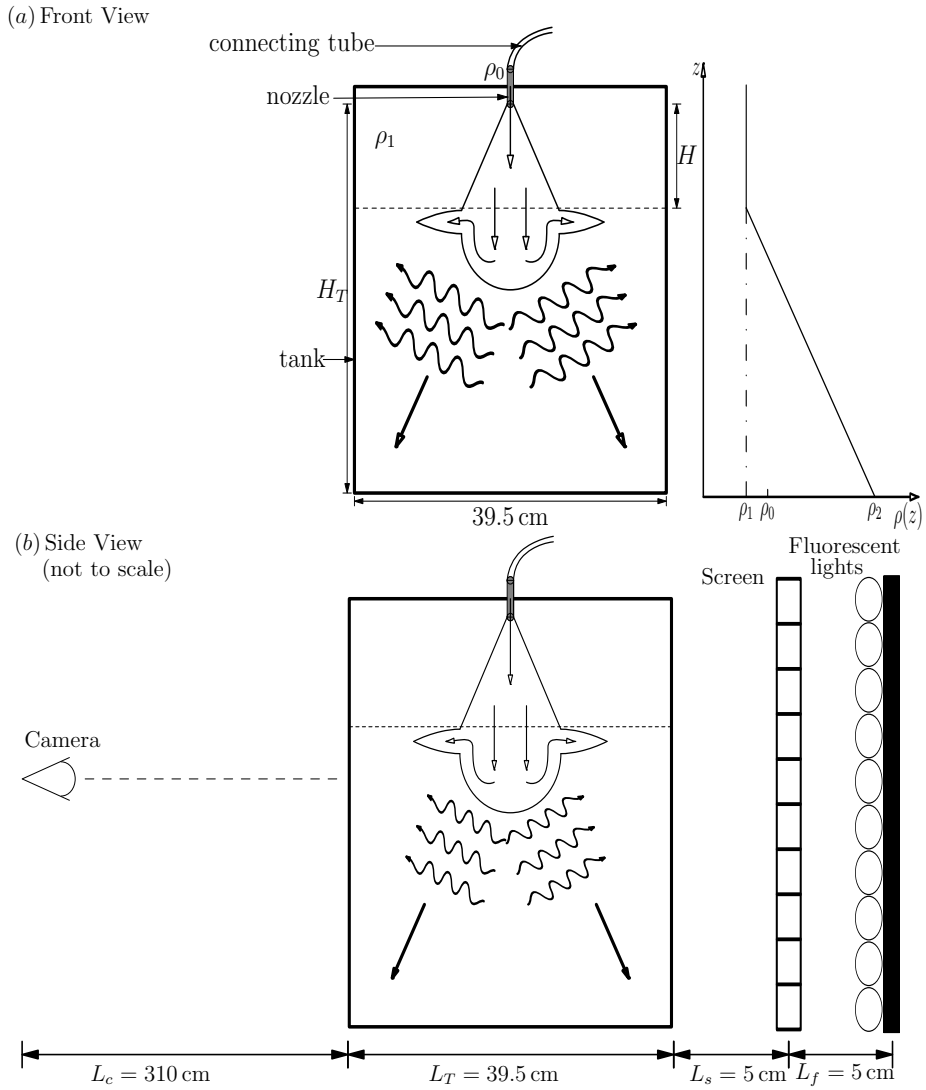

Figure 4.1: (a) Front view of the experimental set-up with background density profile and (b) side view showing set-up used for Synthetic Schlieren.

water of density ρ_0 ($\rho_1 < \rho_0 < \rho_2$) was dyed with blue food colouring and then allowed to drain into the tank through a round nozzle of radius 0.2 cm. To ensure the flow turbulently leaves the nozzle, it was specially designed and fitted with a mesh having openings of extent 0.05 cm. The flow rates for the experiments were recorded by measuring the total volume released during an experiment. Flow rates ranged from 1.7 to 3.3 cm^3/s.

Experiments were recorded using a single digital camera situated 310 cm from the front of the tank. The camera was situated at a level parallel to the mid-depth of the tank and the entire tank was in its field of view. Fluorescent lighting was placed 10 cm behind the tank to illuminate the set-up (see figure 4.1*b*). A grid made of horizontal black and white lines was placed between the lighting apparatus and the tank for post-experiment analyses using the Synthetic Schlieren method.

Using "DigImage" software, the maximum penetration depth of the plume and the initial velocity, w_0, were determined by taking vertical time-series constructed from vertical slices of movie images at the position of the nozzle. The temporal resolution was as small as 1/30 s and the spatial resolution was about 0.1 cm.

Horizontal time series were used to determine the radial velocity of intrusively spreading gravity currents. They were taken at the vertical position of the neutral buoyancy level.

The generated internal waves were visualized using axisymmetric Synthetic Schlieren (Onu *et al.* (2003); Decamp *et al.* (2008)). Apparent distortions of the image of black and white lines were recorded by the camera and the time derivative of their vertical displacement, Δz_t, was estimated by comparing two images taken within a short time interval. Using the Δz_t field, the time derivative of the squared buoyancy frequency, $N_t^2(r, z, t)$, is obtained. The N_t^2 field is useful since it can be used to remove noise by filtering out long time-scale disturbances. The field is also in phase with the vertical displacement field. The amplitude of the vertical displacement field, $A_{\xi nm}$, for waves with frequency ω_m and radial wavenumber k is calculated from the amplitude of

the N_t^2 field, $A_{N_t^2 nm}$, using (see Table 2.1):

$$A_{\xi nm} = -\frac{A_{N_t^2 nm}}{k_z \omega_m N^2}, \tag{4.1}$$

in which k_z is determined using (2.116).

4.2.2 Qualitative analyses

Experiments with a uniform-density layer

Figure 4.2 presents series of spatial snapshots showing the evolution of a plume and the generation of vertically and radially propagating waves. The images on the left of figure 4.2 are snapshots of the evolving plume and the black and white lines in the images are those of the screen placed behind the tank. The middle column of images are the Δz_t fields revealing the vertical and horizontal structure of distortions resulting from the waves. These depend upon the horizontal x and vertical z coordinates. The images on the right are Schlieren-processed images also showing the structure of the internal waves themselves as they depend upon the radial R and vertical z coordinates.

As is typical of turbulent forced plumes, when the experiment starts, the plume rises due to its positive buoyancy and source momentum, linearly increasing in width as it rises due to entrainment from the ambient. It reaches the interface in a time of about $t \sim 1.5\,\mathrm{s}$ and penetrates beyond the interface to a maximum height of $z \sim 17\,\mathrm{cm}$ in about $t \sim 4.0\,\mathrm{s}$ (not shown). During the initial evolution of the plume as it rises to its maximum height internal gravity waves are not observed. The waves begin to emanate away from the cap of the plume when it started to fall back upon itself. After collapsing upon itself the plume then spread radially outward as an intrusive gravity current at the neutral buoyancy level.

Figure 4.3(a) shows a horizontal time series taken at the neutral buoyancy level ($z \approx 13\,\mathrm{cm}$) of the experiment shown in figure 4.2. The level of neutral buoyancy is usually located by inspecting spatial snapshots of the experiments.

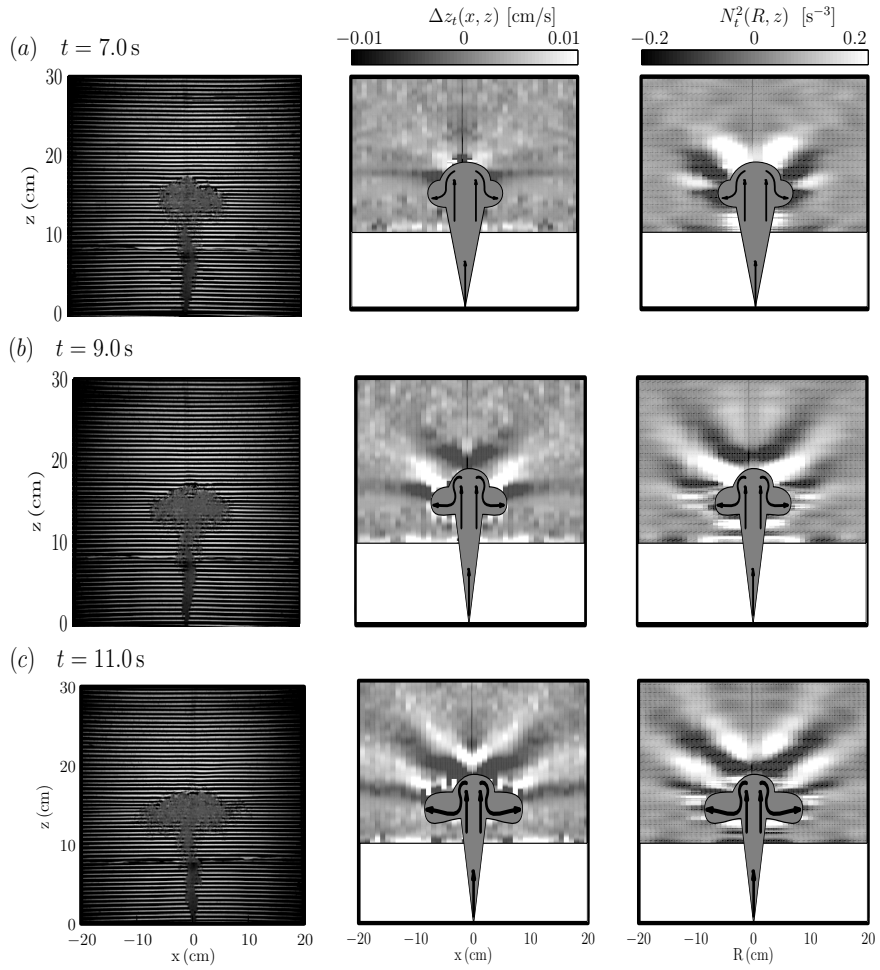

Figure 4.2: Snapshots of plume (flipped upside down and shown on the left), the Δz_t field (shown in the middle) and the N_t^2 field of the waves (shown on the right) at (a) $t \sim 7.0\,\mathrm{s}$, (b) $t \sim 9.0\,\mathrm{s}$ and (c) $t \sim 11.0\,\mathrm{s}$. For the figures in the middle and on the right, the mixed layer region is covered with a white background to highlight the waves and schematics of the plume are superimposed to approximately show its position. The experiment is performed with $\rho_0 = 1.0734\,\mathrm{g/cm^3}$, $\rho_1 = 1.0363\,\mathrm{g/cm^3}$, $N = 1.75\,\mathrm{s^{-1}}$, $H \approx 10\,\mathrm{cm}$, $Q_0 = 3.3\,\mathrm{cm^3 s^{-1}}$.

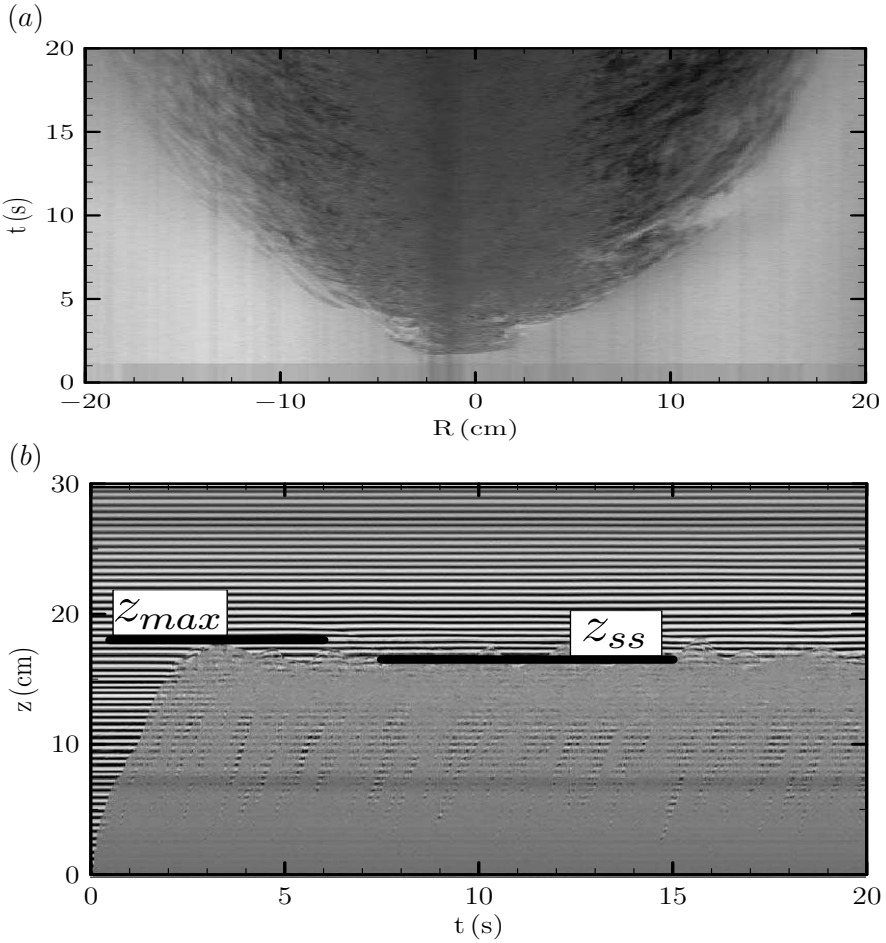

Figure 4.3: (a) Horizontal and (b) vertical time series of the experiment in figure (4.2). The horizontal time series is constructed from a slice taken at the neutral buoyancy level, $z \approx 13\,\mathrm{cm}$. The vertical time series is taken from a vertical slice through the source at $R = 0\,\mathrm{cm}$.

A well-established intrusion usually produces a pointed nose and the vertical location of the nose is used to locate the neutral buoyancy level. The radial propagation of the front of the intruding current can be seen. The parabolic nature of the time series shows the change in speed of the front of the current as it spreads towards the tank sidewalls.

Figure 4.3(b) shows a vertical time series taken through the center of the plume ($R = 0\,\mathrm{cm}$) illustrating the initial ascension and later vertical oscillatory motion of the plume top with time. This is the same experiment shown in figure 4.2 in which the plume penetrated to a maximum height $z_{\max} \approx 17\,\mathrm{cm}$. Upon reaching the maximum height, the plume reverses direction due to negative buoyancy and collapses upon itself. The collapsing of the fluid decreases the consequent maximum height of the plume. However, due to the continuous release of fluid from the source, new fluid penetrates the collapsing fluid so as to maintain the plume fluctuating about a quasi-steady-state height z_{ss}. The maximum and steady state heights are indicated in figure 4.3(b).

At time $t \sim 7.0\,\mathrm{s}$, the rightmost image in figure 4.2(a) shows the waves beginning to emanate from the plume cap. The black and white bands correspond to the troughs and crests respectively of the wave beams. The waves propagate upward and outward toward the tank walls at the same time. A new wave trough appears at $t \sim 9.0\,\mathrm{s}$ (figure 4.2b) above the plume head with approximately the same amplitude as the first trough. At $t \sim 11.0\,\mathrm{s}$, figure 4.2c shows the region above the spreading current completely covered with the wave beams. All this while, the radial current continues to spread toward the walls of the tank. Nevertheless, the wave beams can still be traced back to the region around the plume cap. This indicates, qualitatively, that the waves are generated by the bulge of fluid at the plume top and not by the spreading currents at the neutral buoyancy level. A quantitative argument supporting this assertion is made by taking the initial spreading speeds of the currents and comparing them with the horizontal phase and group speeds of the waves (see Section 4.3.2).

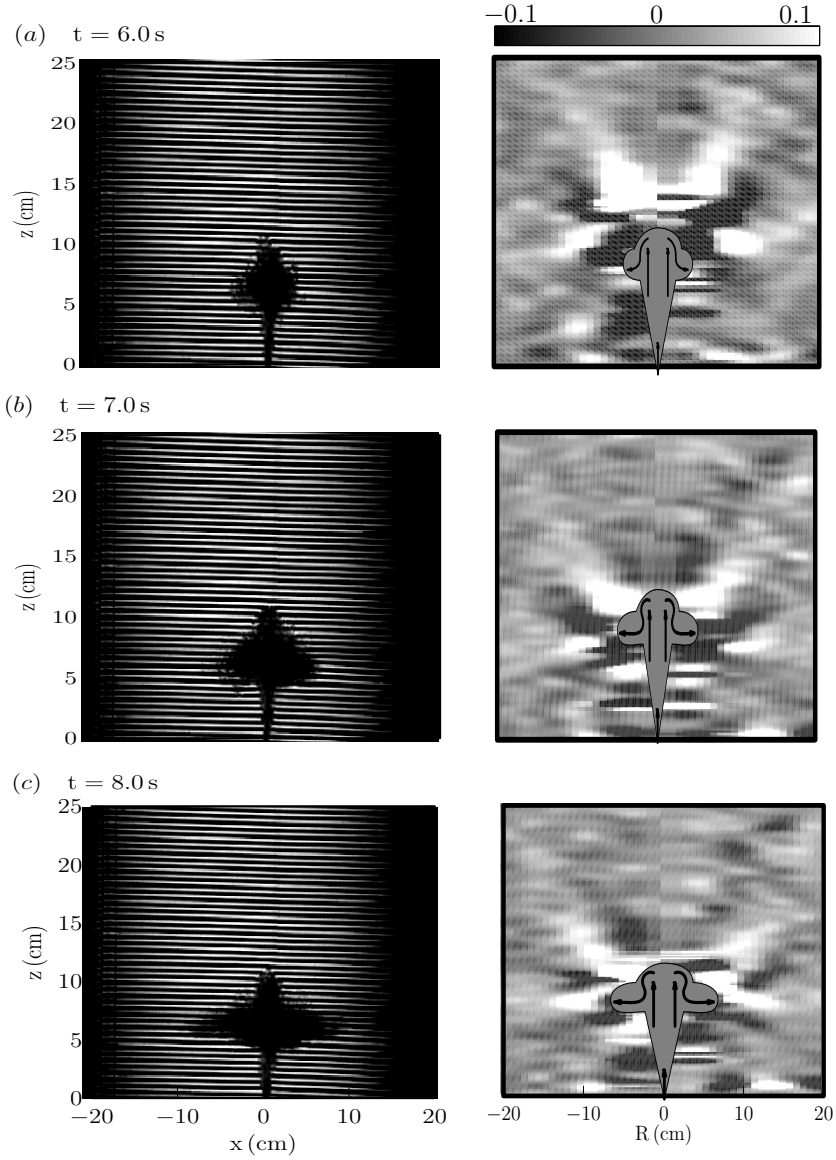

Figure 4.4: Snapshots of plume (flipped upside down and shown on the left) and the N_t^2 field of the waves (shown on the right contours in s^{-3}) at (a) $t \sim 6.0\,\mathrm{s}$, (b) $t \sim 7.0\,\mathrm{s}$ and (c) $t \sim 8.0\,\mathrm{s}$. For the figures on the right, schematics of the plume are superimposed to approximately show its position. (Experiment with $\rho_0 = 1.0720\,\mathrm{g/cm^3}$, $\rho_1 = 1.0310\,\mathrm{g/cm^3}$, $N = 1.43\,\mathrm{s}^{-1}$, $Q_0 = 3.2\,\mathrm{cm^3 s}^{-1}$, $H = 0\,\mathrm{cm}$)

Experiments without a uniform-density layer

Experiments were also conducted for the case when there was no mixed layer but with a linearly stratified fluid over the whole tank depth. This is the special case in which the uniform-density layer has depth $H = 0$. The evolution of plumes and fountains in linearly stratified environments have previously been studied (Morton *et al.* (1956), Bloomfield & Kerr (1998)) but the wave field was not analyzed. The wave field is more complex in this case and the linear stratification results in the generation of both upward and downward propagating wave cones by the turbulent plumes.

Figure (4.4) shows snapshots of a plume as well as the generated internal waves in an experiment with $H = 0\,\mathrm{cm}$. Similar to the experiment with $H = 10\,\mathrm{cm}$, waves are not observed until the plume reaches the maximum height and starts to fall upon itself. The plume in this case reaches its maximum height $z_{\max} \sim 10\,\mathrm{cm}$ in about $3\,\mathrm{s}$ (not shown). At about $6\,\mathrm{s}$ (figure 4.4a) we observe the appearance of wave beams around the plume head. Only upward propagating waves are prominent in the wave field at this time even though the appearance of a downward propagating crest and trough can be seen to emanate from around the plume cap. More wave beams are observed in figure 4.4(b) ($t = 7\,s$) with upward propagating waves still prominent. In both figures 4.4(b) and (c), we observe a cross-pattern of waves resembling the cross-pattern observed in waves generated by an oscillating sphere. The downward propagating waves appear to be generated by the resulting intrusions but nevertheless the phase lines still appear to be radiating from a localized source close to the region below the plume head. In this case the mean depth of the intrusion is about $6\,\mathrm{cm}$ from the source. We also note that, despite the different ambient stratifications, the radial scale of the waves is similar both in this case and in the $H > 0$ cases (see figures 4.2(c) and 4.4(c)).

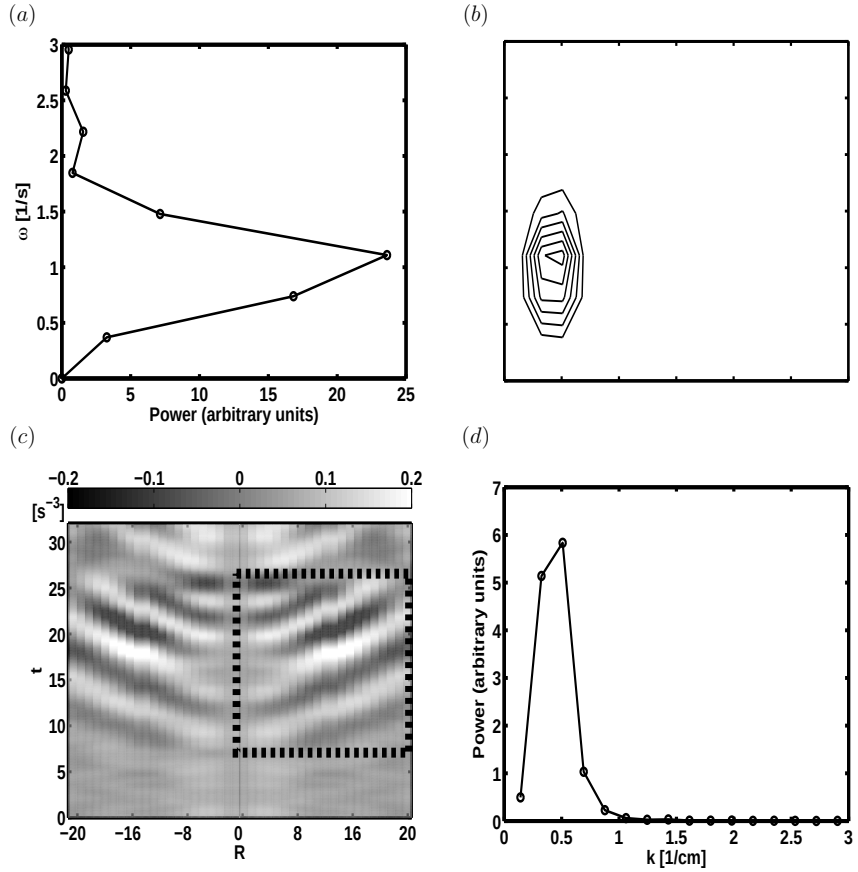

Figure 4.5: (a) Frequency spectrum obtained by averaging over all radial wave numbers in (b), where (b) shows the average power spectrum from different horizontal time series taken over the rectangular window shown in (c). (c) is a horizontal time series taken at $z = 22\,\mathrm{cm}$ of the experiment in figure 4.2. The horizontal slices are taken in the range $19.0\,\mathrm{cm} \leq z \leq 25\,\mathrm{cm}$ and $7.0\,\mathrm{s} \leq t \leq 25\,\mathrm{s}$ (rectangle with dashed lines). (d) Radial spectrum obtained by averaging over all frequencies in (b). Experimental parameters are the same as in figure 4.2.

4.2.3 Bessel-Fourier analyses

Figure 4.5 plots the time series and power spectra used to obtain the characteristic frequency and radial wavenumber of the waves.

In figure 4.5(c), the horizontal time series is taken at a vertical position $z = 20\,\text{cm}$ of the experiment shown in figure 4.2. The plume in this case penetrated to a maximum height $z \approx 17\,\text{cm}$. Thus, the position $z = 20\,\text{cm}$ is about 3 cm above the maximum penetration height which means that the bulge of fluid from the plume is not captured in the time series; only the radially propagating waves moving up and away from the plume cap are captured.

The horizontal time series shows the radial propagation of the waves with time, and from this we measure the radial and temporal characteristics of the waves. To obtain the characteristic radial wavenumber k_c and frequency ω_c of the waves, we first compute Bessel-Fourier spectra over a specifically chosen window in radial space and time ($0\,\text{cm} \lesssim R \lesssim 20\,\text{cm}$, $1.5 \lesssim t/T_b \lesssim 4.5$) from several horizontal time series taken above the maximum penetration height. Here $T_b = 2\pi/N$ is the buoyancy period. These spectra are then averaged to obtain a characteristic power spectrum of the waves. For example, the average power spectrum shown in figure 4.5(b) was obtained by Fourier-transforming in time and Bessel-transforming in the radial direction over several rectangular windows such as the one shown on figure 4.5(c) extracted from images of the experiment shown in figure 4.2. In this case, the horizontal slices are taken in the range $20\,\text{cm} \leq z \leq 25\,\text{cm}$ and the time interval is $7\,\text{s} \leq t \leq 25\,\text{s}$. Choosing a window avoids the inclusion of the reflected wave beams from the sidewalls of the tank. From the power spectrum, we observe that the waves are quasi-monochromatic. Averaging over all radial wavenumbers gives the frequency spectrum in figure 4.5(a). This shows a peak frequency $\omega \approx 1.1\,\text{s}^{-1}$. However, there is non-negligible power in neighbouring frequency components and so a characteristic frequency of the waves is found by calculating a power-weighted

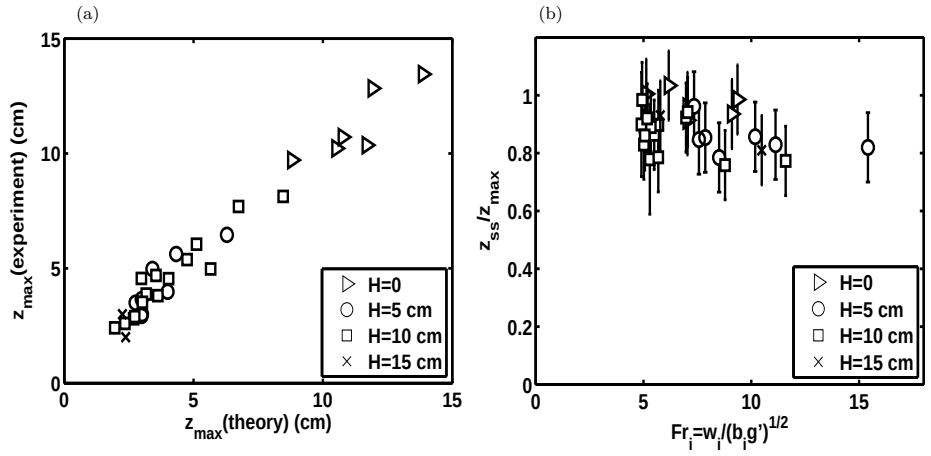

Figure 4.6: (a) The maximum penetration height above the interface and (b) the ratio of the steady-state height to the maximum height.

average:

$$\omega_c = \frac{\sum_m \omega_m |A_{\xi m}|^2}{\sum_m |A_{\xi m}|^2}.$$

Computed in this way, the characteristic frequency of the waves in this case is found to be $\omega_c = 1.0\,\mathrm{s}^{-1}$.

Averaging over all frequencies gives the radial spectrum shown in figure 4.5(d) with a peak radial wavenumber $k \approx 0.5\,\mathrm{cm}^{-1}$. The figure also shows that most of the radial power lies in the second and third modes. A characteristic radial wavenumber is obtained by calculating a power-weighted average to get $k_c = 0.4\,\mathrm{cm}^{-1}$.

4.3 Quantitative analyses

In this section, we give a quantitative analyses of the results and compare them with theory. In the experiments without a uniform layer of fluid ($H = 0$), only the upward propagating waves have been included in the analyses.

4.3.1 Maximum penetration height

Figure 4.6(a) plots the experimentally measured values of the maximum penetration height above the interface compared with the theoretical prediction of Morton (1959a). The maximum plume height $z_{\max}$ is computed by numerically solving equations (2.42)-(2.44) using values of M, F and Q evaluated at the interface. There is good agreement in the data with a correlation of about 90 %. Figure 4.6(b) plots the ratio $z_{\rm ss}/z_{\max}$ against the interfacial Froude number, Fr_i. The average value of this ratio was found to be 0.90 ± 0.1. Morton *et al.* (1956) did not measure the quasi-steady-state height in their experiments of a plume in a linearly-stratified ambient, however we find that this ratio compares well with the case of a fountain in a linearly-stratified environment measured by Bloomfield & Kerr (1998) to be 0.93. This value is slightly greater than the ratio obtained for a fountain in a two-layer density-stratified ambient in which the ratio is about 0.88 (see Section 3.3.2). Although within errors, the ratio may also be due to the greater interaction of the descending annular plume with the main upflow in the case of a fountain in a two-layer ambient as compared to a plume in a stratified environment in which the distance of interaction is between the maximum height and the neutral buoyancy level.

4.3.2 Radial intrusion speeds

The main goal of measuring the initial speeds of the axisymmetric currents is to show that the measured waves are those generated by the vertical fluctuations of the plume and not the radially spreading currents.

Figure 4.7 plots the experimentally measured values of the level of neutral buoyancy, z_n (see figure 4.11), compared with the theoretical prediction of equations (2.42)-(2.44) using values of M, F and Q evaluated at the interface. Theoretically, the level of neutral buoyancy is taken as the height where the buoyancy flux first vanishes. In the experiments, the neutral level is visually determined from spatial snapshots after the intrusion is established. There is good agreement in the data with a correlation of about 95 %. Only experiments

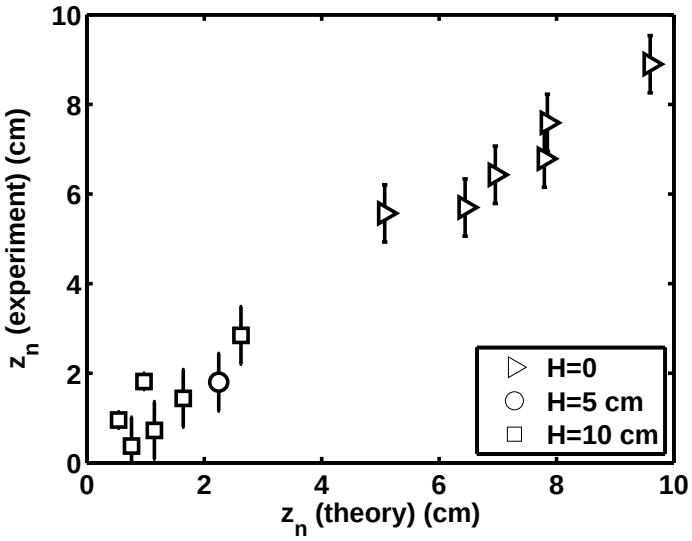

Figure 4.7: Intrusion height, z_n, of the radial currents for experiments with $z_n > 0.5\,\mathrm{cm}$.

with the neutral buoyancy level greater than 0.5 cm from the interface are plotted. This is because the neutral buoyancy level is usually indistinguishable from the interface for $z_n < 0.5\,\mathrm{cm}$ and besides the error involved in measuring the position of the interface is about 0.3 cm.

The relationship between theory and experiment is surprisingly good considering the fact that the theory, as applied here, assumes that there is no mixing of ambient fluid between the neutral level and the maximum height. This is probably due to the fact that the axial velocity of the plume continues to decrease from the neutral buoyancy level until it finally comes to rest at the maximum height. Therefore the assumption that entrainment is proportional to the axial velocity implies that there is less entrainment in this part of the plume motion (Morton *et al.* (1956)). A similar assumption was used by Abraham (1963) to model the topmost part of turbulent fountains where it was assumed that there is detrainment rather than entrainment of ambient fluid.

The initial speeds of the axisymmetric currents were measured by taking the slope near $R \approx R_n$ of horizontal time series as shown, for example, in figure

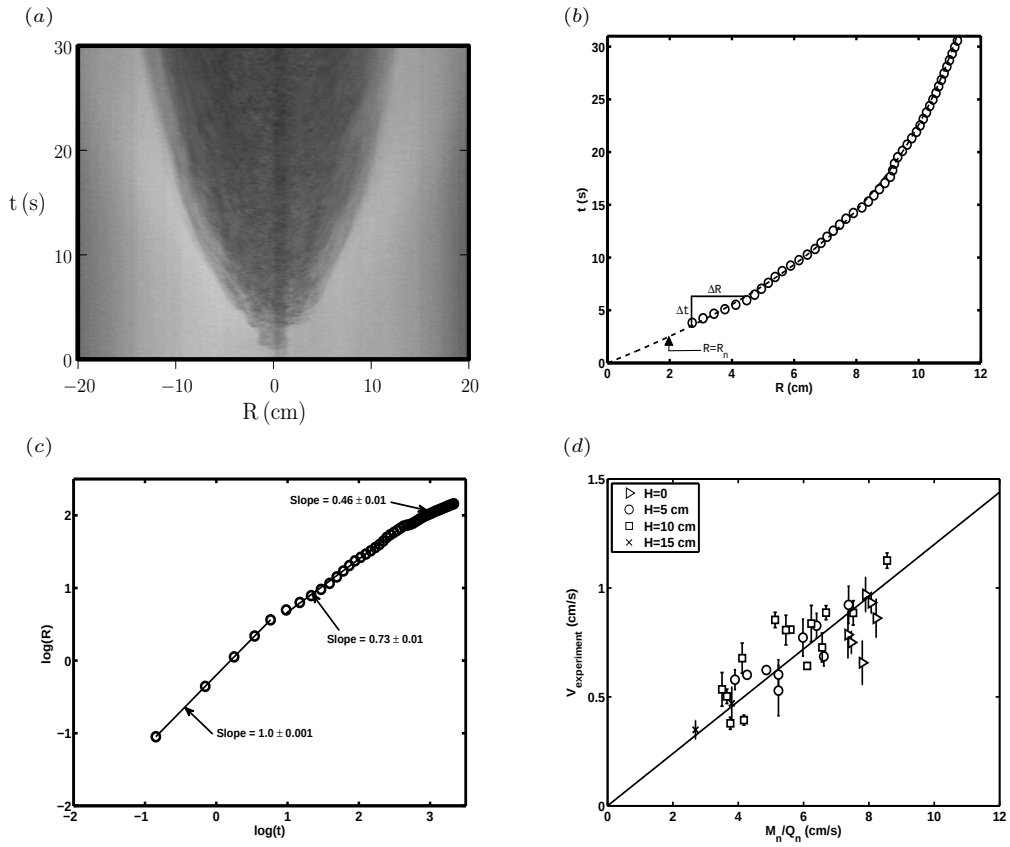

Figure 4.8: (a) Horizontal time series for an experiment with $N = 1.62\,\mathrm{s}^{-1}$, $H = 5\,\mathrm{cm}$, $\rho_0 = 1.0544\,\mathrm{g/cm}^3$, $\rho_1 = 1.0511\,\mathrm{g/cm}^3$. The time series was constructed from a slice taken at the neutral buoyancy level ($z \approx 5.2\,\mathrm{cm}$). ($b$) Typical approach of calculating the initial spreading speeds with $\Delta R \approx R_n$. ◯, experimental data; ..., fitted line. (c) The log-log plot of the horizontal time-series showing the different spreading regimes. (d) Plot of the initial spreading speeds for all experiments.

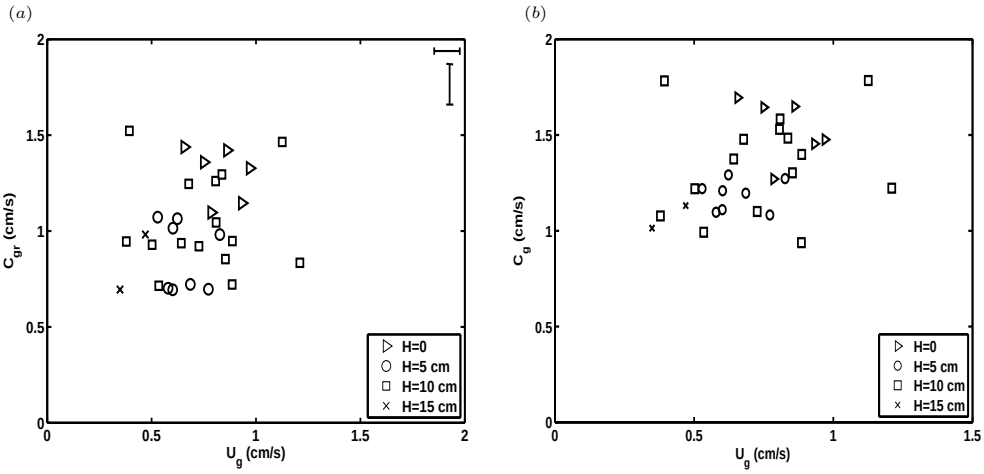

Figure 4.9: Radial intrusion speed, U_g, versus the (a) radial phase speed, c_{gr}, and (b) group speed, c_g, of the waves. Characteristic error bars are shown at the top right corner in (a).

4.8(b). R_n is the width of the plume at the neutral buoyancy level which is determined from horizontal time series such as figure 4.8(a). Both the left and right-moving current speeds are measured and the average used to estimate the initial speeds.

Figure 4.8(c) shows a typical log-log plot of distance against time taken from figure 4.8(b). This is used to determine the appropriate initial scaling relationship between distance and time for the intrusions. All the experiments were found to spread initially as $R \sim t^{\kappa}$ with $\kappa = 1.0 \pm 0.1$. Figure 4.8(d) plots the initial spreading speeds of the intrusion compared with equation (2.111) with the initial radial momentum and volume fluxes replaced by those of the plume at the neutral buoyancy level. The plot shows a relationship of the form

$$V = (0.12 \pm 0.02) \left(\frac{M_n}{Q_n} \right). \tag{4.2}$$

Figures 4.9(a) and 4.9(b) plot the initial speed of the intrusion against the radial phase speeds and group velocities of the waves respectively. Both plots show a poor relationship between the respective parameters. This provides further support to the assertion that the waves are generated by a localized

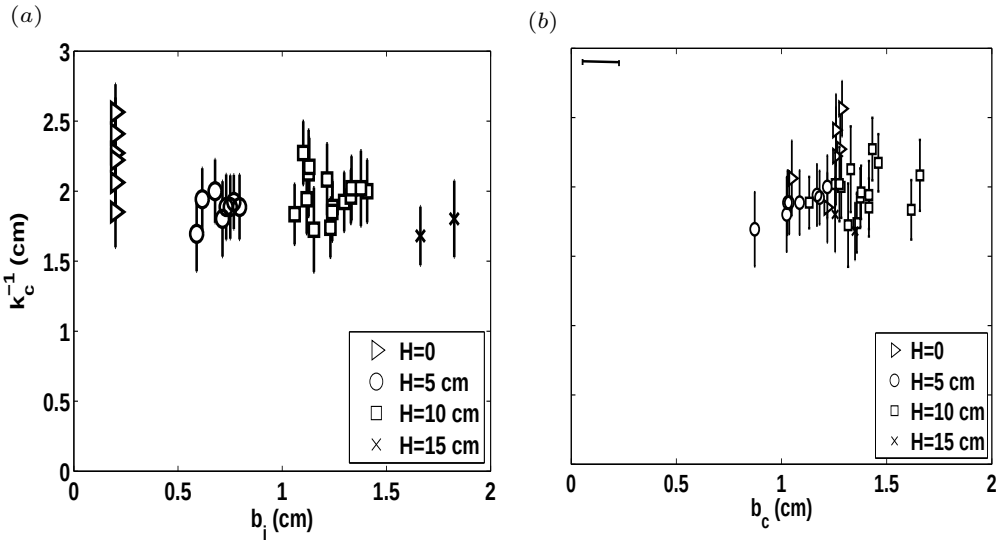

Figure 4.10: The inverse characteristic radial wavenumber as a function of the (a) radius of plume at the interface for the uniform-density layer case (the source radius is used on the $x-$axis in the case $H = 0\,\text{cm}$), (b) mean radius of the plume cap. Characteristic error bar for b_c is shown at the top left corner.

source around the plume cap and not by the intrusion currents. Although the intrusions may also generate waves, these are not the dominant waves measured in the experiments above the maximum penetration height. Moreover, the waves were observed to be generated long before the intrusion is well established.

4.3.3 Radial wavenumber

Since the most obvious horizontal scale of the generating source is the width of the plume at the density interface, one might expect that the radial scale of the waves is set by this parameter. To investigate this, experiments with varying mixed layer depths were conducted.

Figure 4.10(a) plots the inverse of the characteristic radial wavenumber against the radius of the plume at the interface, b_i, for all the experiments. We observe that $k_c^{-1} \approx 2.0\,\text{cm}$ is almost constant for experiments with different mixed layer depths ($H \approx 0$, 5, 10, 15 cm) and therefore for different plume

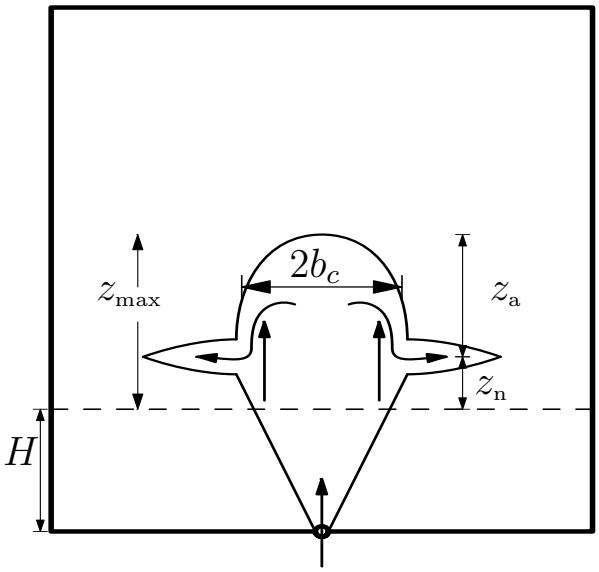

Figure 4.11: Schematic showing the position where the radius of the plume cap, b_c, the maximum penetration height, $z_{\max}$ and neutral buoyancy level, z_n are measured. z_a is the distance above the neutral buoyancy level.

radii at the interface. The source radius is used in the case $H = 0$ and has also been plotted on figure 4.10(a). The lack of correlation in the experiments show that the radial scale of the waves is not set by the width of the plume at the density interface. This is unlikely to be caused by the effects of the tank size since the radial scale of the waves is set before the waves reach the sidewalls of the tank (e.g. see figure 4.2).

Because we start observing the waves when the plume begins to fall upon itself, we hypothesize the scale of the waves is set by the radius of the plume cap just after the plume reached the maximum height. For each experiment, three measurements of the plume cap radius were taken within one second of each other after the plume reached the maximum height. The measurements were taken at a vertical level midway between the maximum height and the neutral buoyancy level (see figure 4.11). The average of these radii was used as the radius of the cap, b_c. Figure 4.10(b) plots the inverse of the characteristic radial wavenumber against the mean radius of the cap. We find that the radius of the cap generally lies between values of 1.0 cm and 1.7 cm comparable to

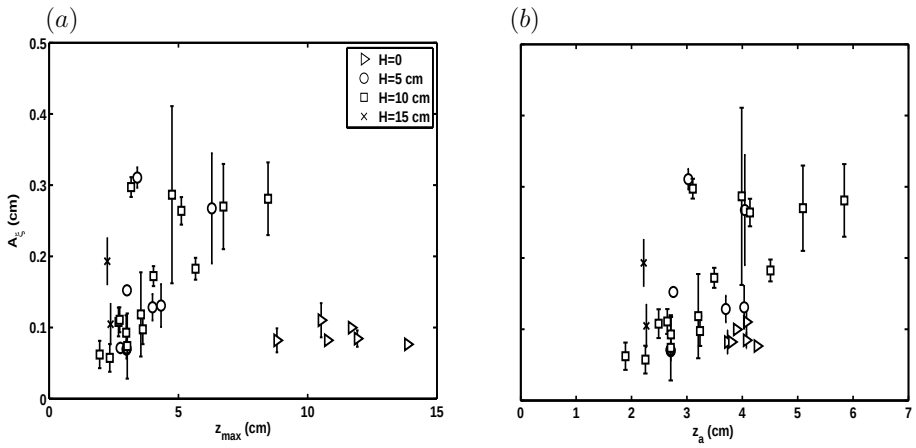

Figure 4.12: Vertical displacement amplitude of waves, A_ξ, versus the (a) maximum penetration height; (b) penetration above the neutral buoyancy level.

k_c^{-1} for different values of H. It therefore appears that the characteristic radial wavenumber is set by the mean radius of the plume cap after it collapses upon itself and not upon the radius of the incident plume at the interface height. What determines the horizontal extent of the plume cap, as it depends upon Q, M and F, is not yet well-established in theory. Indeed, numerical and theoretical attempts to model the dynamics of the plume cap rely on heuristic methods (McDougall (1981); Bloomfield & Kerr (2000)).

4.3.4 Vertical displacement amplitude

One might expect that the amplitude of the waves would depend upon the maximum penetration height of the plume into the stratified layer. This is because the greater the penetration of the plume into the linearly stratified layer the greater the displacement of the isopycnals above the plume cap.

Figure 4.12(a) plots the theoretical maximum penetration of the plume against the maximum vertical displacement amplitude, A_ξ, that is measured in the wave field. The amplitudes are obtained from horizontal time series taken about 3 cm above the maximum penetration height. This enables us to measure the near-maximum amplitudes of the waves without corruption of the signal by the plume itself that would occur by taking measurements too close

to the plume. For the $H > 0$ cases, the trend in the plot suggests a strong linear dependence of the amplitude upon the maximum penetration depth within the limits of the experimental parameters. Even though the $H = 0$ cases penetrated further into the stratified ambient, their amplitudes are not as large. They have an almost constant amplitude around 0.1 cm. This means that the maximum penetration height does not properly characterize the amplitude of the waves. In figure 4.12(b), we have plotted the vertical displacement amplitude against the penetration of the plume beyond its neutral buoyancy level, z_a (see figure 4.11). The trend indeed shows a linear relationship for all cases even though there is less variation in z_a for the $H = 0$ cases. The linear trend in figure 4.12(a) for the $H > 0$ cases may also be due to the fact that most of those experiments had their neutral buoyancy levels close to the interface height so that $z_{\max}$ is approximately equal to z_a as explained in Section 4.3.2.

Caution needs to be taken in interpreting this result since the amplitudes of the waves are not expected to increase to infinity with increasing maximum penetration. Experiments with larger penetration depths could not be examined because we needed to ensure that there was sufficient vertical and horizontal space for analysing the waves in the limited domain of the tank.

It is also important to recognize the different dynamics involved in the $H > 0$ and $H = 0$ cases. In the $H > 0$ case, the plume is largely controlled by buoyancy forces as it enters the stratified layer since its initial momentum is mostly used up by the time the plume impinges the interface. Calculation of the jet length at the interface (see equation 2.55) shows that $\zeta > 1$ for the $H = 10$ cm cases and about 1.0 for the $H = 5$ cm cases. So its dynamics within the stratified layer is not jet-like but lies in the transition region. On the other hand, in the $H = 0$ case, the plume enters the stratified layer as a forced plume, being controlled initially by the momentum at the source and later by buoyancy forces. Thus, even though the plume in the $H = 0$ case travelled farther in the stratified layer, it does not necessarily have a higher overshooting distance. In general, the overshooting distance largely depends on the excess momentum at the neutral buoyancy level which in turn depends upon the

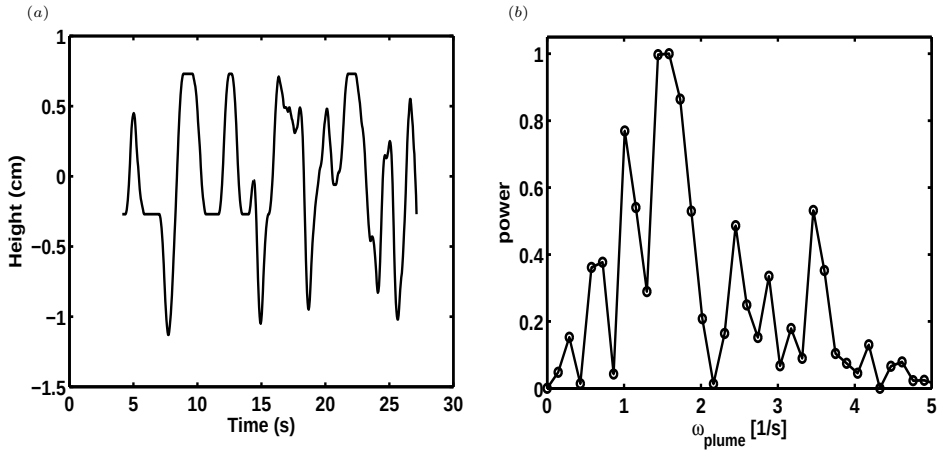

Figure 4.13: (a) Vertical time series through the center of a plume with parameters: $\rho_0 = 1.0400\,\mathrm{g/cm^3}$, $\rho_1 = 1.0230\,\mathrm{g/cm^3}$, $N = 1.17\,\mathrm{s^{-1}}$, $Q_0 = 2.15\,\mathrm{cm^3 s^{-1}}$, $H \approx 5\,\mathrm{cm}$. The vertical fluctuations are subtracted from their mean value to get the vertical axis. (b) The frequency spectrum of the signal in (a) with the power normalized by the maximum power.

strength of the stratification and the fluxes of buoyancy and momentum at the source.

4.3.5 Wave frequency versus forcing frequency

When the plume reaches the initial maximum height, it falls upon itself because of its negative buoyancy and subsequently it oscillates about a quasi-steady-state depth. Though these oscillations appear random, to our knowledge, they have not before been analyzed to determine their spectral characteristics. Turner (1966) observed that the quasi-steady fluctuations of salt water fountains in one-layer fresh water environments were small and random. On the contrary, the fluctuations from 'evaporating' plumes (composed of various mixtures of alcohol and ethylene glycol) were observed to be more dramatic in that they were more regular and with larger amplitudes. The amplitudes decreased with time but eventually achieved the same mean height as the salt water fountains (see figure 3 of Turner (1966)).

In figure 4.13(a) we plot the fluctuations from an experiment with buoyancy frequency $N = 1.17\,\mathrm{s^{-1}}$. These were determined by taking a vertical

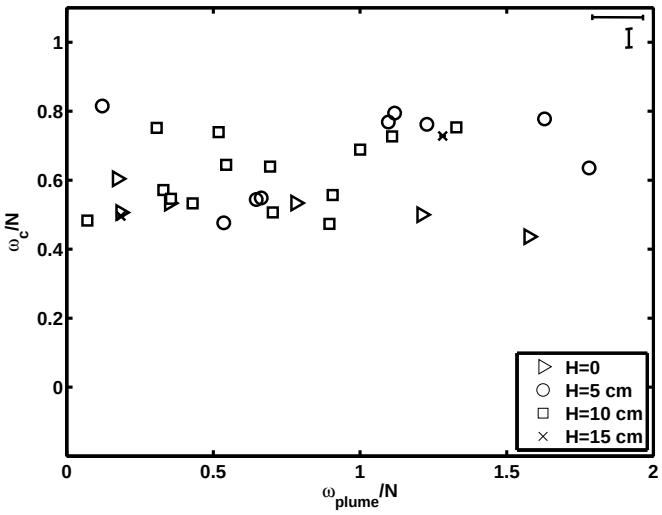

Figure 4.14: Peak forcing frequency of the plume, ω_{plume}, versus the frequency of the waves both normalized by the buoyancy frequency. Characteristic error bars are shown at the top right corner.

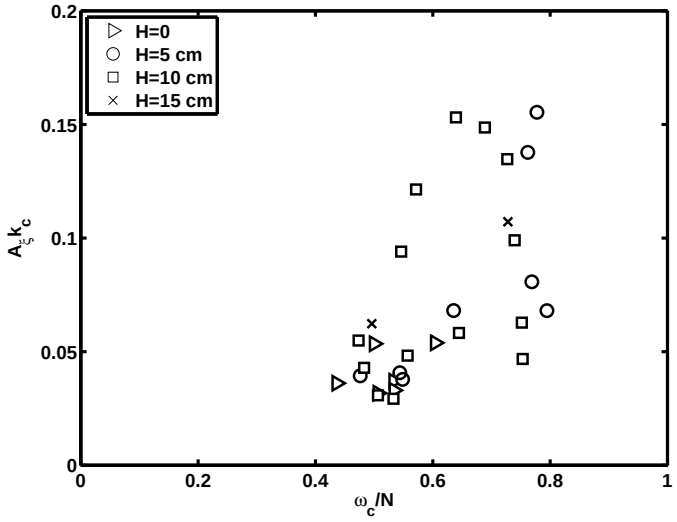

Figure 4.15: Relative frequency of the waves versus the normalized amplitude.

time series through the center of the plume and the extent of the vertical fluctuations were subtracted from their mean values. The figure shows a quasi-regular pattern of oscillations. A Fourier decomposition of the signal gives the frequency spectrum shown in figure 4.13(b). The spectrum exhibits a wide range of frequencies with a peak frequency around $1.6\,\mathrm{s}^{-1}$, greater than the buoyancy frequency of the stratified layer and greater than the characteristic frequency of the generated waves ($\omega_c \approx 1.0\,\mathrm{s}^{-1}$ in this case). Figure 4.14 shows a plot of the peak frequency of the plume, ω_{plume}, versus the frequency of the waves illustrating that there is no direct linear relationship between the two parameters. Thus, unlike internal gravity waves generated by solid objects (such as spheres and cylinders) undergoing small amplitude oscillations (see Mowbray & Rarity (1967a); Sutherland *et al.* (1999); Sutherland & Linden (2002); Flynn *et al.* (2003)), waves generated by turbulent forced plumes have peak frequencies which do not directly relate to the observed fluctuations of the plume cap itself.

Both figures 4.14 and 4.15 further show that the characteristic frequency of the waves generated by the turbulent plumes lie in a narrow frequency range ($0.45 \leq \omega_c/N \leq 0.85$). This is consistent with the findings of Dohan & Sutherland (2003) in which the waves generated by turbulence were found to lie in a narrow frequency range ($0.5 \leq \omega/N \leq 0.75$). They hypothesized that turbulent eddies generating internal gravity waves interact resonantly with the waves in a manner that most strongly excites those waves that vertically transport the most horizontal momentum (Sutherland & Dohan (2004)). Such waves exert the most drag on the source and so are most efficient at modifying the structure of eddies that excite them.

4.3.6 Energy extraction by waves

The rate of working owing to buoyancy forces of the plume at the neutral buoyancy level was calculated from equation (2.71) by replacing the radius and velocity at the interface with those at the neutral level. The average

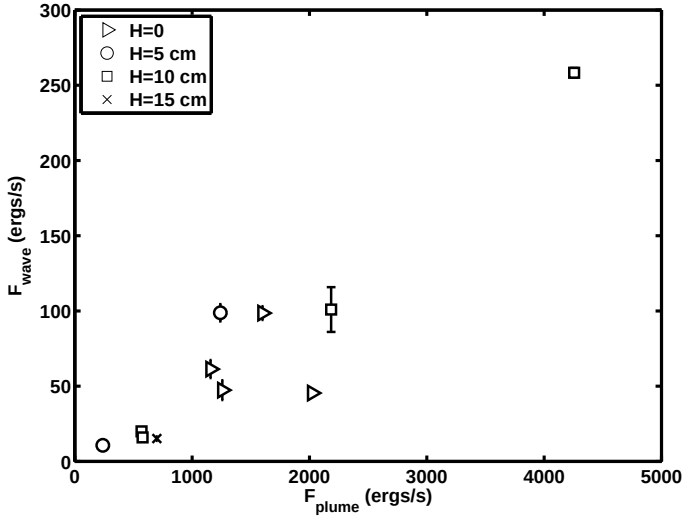

Figure 4.16: The energy flux of the plume at its neutral buoyancy level versus the energy flux of the waves.

wave energy flux was calculated using equation (2.118). This was derived by assuming that the waves generated were symmetric about the center of the tank. To verify this, energy fluxes from the left and right sides of the tank were independently determined and the average energy flux calculated. Separately, the N_t^2 fields from the left and right sides of the tank were first averaged and the mean energy flux calculated. The difference in the energy fluxes between the two approaches approximately give the error involved in the assumption of axisymmetry. The asymmetry in the wave field is usually caused by the tilting to one side of the plume cap from the centerline as the plume falls upon itself. This behaviour is difficult to control even if the initial injection of plume fluid is kept vertical.

Using the criteria mentioned above, if the difference between the two calculations is greater than 20%, the experiment is considered asymmetric and is not included in the analyses of the energy fluxes. We find that about 30% of the experiments had differences to within 20%.

Figure 4.16 plots the estimated energy flux of the plume at its neutral buoyancy level against the mean energy flux of the waves (calculated by taking the average of the energy fluxes from the left and right sides of the tank).

The average energy flux of the waves for each side of the tank is estimated by vertically averaging energy fluxes over a four-centimeter interval ($z_{\max}+3\,\mathrm{cm} \lesssim z \lesssim z_{\max}+7\,\mathrm{cm}$) in order to capture any vertical fluctuations in the energy flux due to the transient and turbulent nature of the source. This vertical range was also chosen to avoid reflected waves from the sidewalls and bottom of the tank. There appears to be a linear relationship between the two parameters. We find that $0.1-8\%$ of the energy flux of the plume at its neutral level is extracted by the waves. The average energy extracted is about 4% for the experiments considered. Although so small this should not influence the large-scale plume dynamics. This is plausibly large enough to influence the eddy dynamics at the boundary between the plume cap and ambient.

4.4 Application to convective storms

The percentage of energy extracted by waves from plumes may be substantial when compared with the enormous amount of energy released by thunderstorms.

The study by Pierce & Coroniti (1966) first proposed that gravity waves may be generated by severe thunderstorms via oscillations of the updrafts within the storm. They stated that the updraught extends throughout most of the cell and are generally of the order of 3 m/s but may locally exceed 30 m/s. Using observational data they were able to estimate the energy per unit volume to be on the order of 1.0 erg/cm^3. Assuming the oscillations extended over an area roughly 10 km by 10 km and over a height interval of 3 km, they estimated the total energy of the oscillation to be 3×10^{10} J.

Curry & Murty (1974) showed through field observations that internal gravity waves are generated by thunderstorms through the transfer of kinetic energy from a rising column of air within the storm cell to a stable region aloft. In a case study, the amplitude spectra showed that the wave consisted essentially of a single component having a period of ~ 16 min and a buoyancy period of 25.0 min ($N\approx 0.004\,\mathrm{s}^{-1}$) which is larger than the observed period

of the waves.

They proposed a simple model for the generation of gravity waves by thunderstorms based on energy considerations. The top of the developing thunderstorm cell was assumed to be a hemispherical cap of radius $\tilde{R}$ and rising with velocity U. It was assumed to interact with waves at its position of stability where it oscillates at a characteristic frequency. The kinetic energy (KE) carried into the source was then calculated as

$$\mathrm{KE} = \frac{\pi}{3}\tilde{R}^3 U^2 \rho_a, \tag{4.3}$$

where ρ_a is the density of the air. An order of magnitude calculation was carried out to find the value $\mathrm{KE} \approx 5 \times 10^9$ J where ρ_a was taken as $0.5\,\mathrm{kg\,m^{-3}}$, the value of $\tilde{R}$ was 500 m and $U = 10\,\mathrm{m\,s^{-1}}$ were used. The rough estimate of the kinetic energy from their model was found to agree well with an estimate from their case study where the kinetic energy was found to be 6×10^9 J.

We recast equation (4.3) in terms of the energy flux at the source to get

$$F_{\mathrm{storm}} = \frac{1}{2}\pi \tilde{R}^2 U^3 \rho_a. \tag{4.4}$$

Using the values of Curry & Murty (1974) results in $F_{\mathrm{storm}} \approx 1.3 \times 10^{15}\,\mathrm{ergs/s}$.

Other observational studies of gravity waves generated by thunderstorms include Balachandran (1980); Larsen *et al.* (1982); Lu *et al.* (1984); Gedzelman (1983); Pfister *et al.* (1993*b*,*a*); Alexander & Pfister (1995); Grachev *et al.* (1995); Karoly *et al.* (1996); Dewan & Coauthors (1998). In particular, Larsen *et al.* (1982) observed that waves are generated only when the vertical extent of the developing clouds approach the level of the tropopause. However, like other observational studies of thunderstorm-generated waves, the details of the horizontal scale of the storm as well as the speeds of the updrafts could not be obtained. One of the difficulties is the fact that the storms themselves are not stationary but vary in both space and time. Another problem is that the observational techniques are unable to provide this information on the storms (Lu *et al.* (1984); Fritts & Alexander (2003)). Aircraft measurements

and satellite imagery usually provide information on the horizontal scale of the storms and limited information on updraft speeds (Pfister *et al.* (1993*b*,*a*); Dewan & Coauthors (1998)). Nevertheless the information provided by aircraft measurements about the characteristics of the generated waves is not enough to help make a concrete quantitative link between the energy flux of the waves and the storms. Some observational studies show that the horizontal scale of the waves are comparable to the horizontal scale of the storms (Pfister *et al.* (1993*a*); Tsuda *et al.* (1994)). The periods of the waves have been reported by some observations to be close to the local buoyancy period (Pierce & Coroniti (1966); Curry & Murty (1974); Larsen *et al.* (1982)) whiles others observe thunderstorm-generated waves to have periods longer than the buoyancy period (Lu *et al.* (1984)). The results of the laboratory experiments presented here show that depending upon the strength of convection, the mechanical oscillator mechanism could contribute on average 4% of the energy flux of the thunderstorm to the waves.

The waves generated by thunderstorms have been reported to have horizontal wavelengths in the range $5 - 110\,\mathrm{km}$, vertical scales in the range $2 - 7\,\mathrm{km}$, periods ranging between 5 min and 3 h and with phase speeds in the range $12 - 30\,\mathrm{m/s}$ (Larsen *et al.* (1982); Lu *et al.* (1984); Pfister *et al.* (1993*b*,*a*); Karoly *et al.* (1996); Vincent & Alexander (2000)). Thus, in general, convective sources generate waves with a broader spectrum than topographically generated waves (Fritts & Alexander (2003)). The study by Fritts & Nastrom (1992) compared the contribution of different gravity wave sources (specifically topography, convection, frontal systems and jet stream) on the momentum budget of the middle atmosphere and concluded that convectively generated waves played a significant role though their influence is not as much as topographically generated waves.

The experimental results from this study suggest that, in the absence of a background mean flow, the horizontal scale of thunderstorm-generated waves is set by the horizontal scale of the top of the clouds in a well-developed storm. Thus, the horizontal scale could be between 5 and 100 km. However,

even though the oscillations of updrafts and downdrafts within a storm are responsible for generating the waves and have broad frequency spectra, their dominant frequency do not necessarily correspond to the dominant frequency of the waves generated. We find that the frequency of waves generated via the mechanical oscillator mechanism lie in a narrow range relative to the local buoyancy frequency, N. The wave frequency may range between $0.45N$ and $0.85N$ where N lies between 10^{-2} and $10^{-3}\,\mathrm{s}^{-1}$. The experiments show that the vertical displacement amplitudes of waves generated via the mechanical oscillator effect depends upon the distance updrafts overshoot their neutral buoyancy level and not upon the vertical scale of the whole storm as in the deep heating effect. From the experimental results, the vertical displacement amplitudes may range between $1 - 5\%$ of the overshooting distance. Based upon observational studies this is about $30 - 150\,\mathrm{m}$. The experiments also reveal that the average energy flux of thunderstorm-generated waves could be as large as 10^{13} ergs/s based upon the rough estimates of energy flux in a single storm cell.

4.5 Conclusions

This chapter presented the results obtained when axisymmetric internal gravity waves are generated by turbulent buoyant plumes.

The results show that the radial wavelength of the waves is not set by the width of the plume at the density interface. Rather the characteristic radial wavenumber is set by the mean radius of the plume cap. Even though the large scale fluctuations at the top of the plume were quasi-regular with some identifiable characteristic peaks in their spectra, these frequency peaks did not match the observed frequency of the waves. Instead, the frequency of the waves relative to the buoyancy frequency was found to lie in a narrow frequency range $\sim 0.7N$. The vertical displacement amplitude of the waves show a strong dependence on the maximum penetration of the plume beyond its neutral buoyancy level for the experiments considered.

The principal goal was to determine the percentage of the energy of the plume at the neutral buoyancy level that is extracted by the upward propagating waves. We found that, on average, four percent of the plume energy is realized as the energy of the waves. Compared with the energy of a single storm cell we estimate the energy flux to be 10^{13} ergs/s.

Chapter 5

Summary and conclusions

This study presented the characteristics of turbulent buoyant plumes in stratified environments. Specifically, I have examined the behaviour of turbulent fountains in two-layer stratified environments. The motivation for this study was to acquire a preliminary understanding of the behaviour of pollutants released into the atmosphere in the form of flares in the presence of atmospheric inversions. I have also analyzed the nature of the internal gravity waves generated when a turbulent plume evolves in both a uniformly and a non-uniformly stratified ambient fluid. This study helped to quantify the contribution of the mechanical oscillator effect to the energy budget of waves generated by convective sources in the atmosphere.

As part of this research I have extended the Lagrangian theory for a fountain in a one-layer fluid to the case of a fountain in a two-layer environment. In particular, two methods were presented which may be used to predict the maximum penetration height of a turbulent fountain in a two-layer fluid.

For fountains in a two-layer fluid, I have, in particular, classified the regimes of flow that result when an axisymmetric turbulent fountain is discharged into a two-layer ambient. The classification was done using the empirically determined parameter, $\theta = (\rho_2 - \rho_1)/(\rho_2 - \rho_o)$, and the relative maximum height, z_{max}/H. The results show that if the maximum penetration height is less than twice the interface height, the return flow will go back to the source

irrespective of the value of θ. However, if the relative density difference is large ($\theta \gtrsim 0.15$) and the maximum penetration height is greater than twice the interface height, the return flow will collapse and spread radially at the interface. I found that such radial currents spread at the source or interface either at constant-velocity (being driven by both the radial components of momentum and buoyancy) or spreading as $R \sim t^{3/4}$ (being driven by buoyancy forces alone). These regimes were distinguished by a critical Froude number $\mathrm{Fr}_s \approx 0.25$ or $\mathrm{Fr}_i \approx 0.4$.

For axisymmetric internal gravity waves generated by turbulent buoyant plumes, I have found that the radial wavelength of the waves is not set by the width of the plume at the density interface. Rather the characteristic radial wavenumber is set by the mean radius of the plume cap. Even though the large scale fluctuations at the top of the plume were quasi-regular with some identifiable characteristic peaks in their spectra, these frequency peaks did not match the observed frequency of the waves. Instead, the frequency of the waves relative to the buoyancy frequency was found to lie in a narrow frequency range $\sim 0.7N$. The vertical displacement amplitude of the waves show a strong dependence on the maximum penetration of the plume beyond its neutral buoyancy level for the experiments considered. The principal goal was to determine the percentage of the energy of the plume at the neutral buoyancy level that is extracted by the upward propagating waves. I found that, on average, four percent of the plume energy is realized as the energy of the waves. Compared with the energy of a single storm cell I estimate the energy flux to be 10^{13} ergs/s.

5.1 Future Work

In the following, we consider possible future extensions of this research. These topics are summarized below and discussed later:

1. Double diffusive plumes

2. Relation between plume cap and fluxes

3. Numerical simulation of plumes generating axisymmetric waves

4. The obstacle effect

5.1.1 Double diffusive plumes

The first problem considered in this research has application to the dispersion of pollutants from flares in the presence of atmospheric inversions. The report by CASA (2002) defined flaring as the act of burning off natural gas as a waste product when it is uneconomic to conserve or in emergency situations when accumulations of gas become a safety concern. On the other hand venting is defined as the direct release of natural gas into the atmosphere and has typically been used as a low-cost option to manage small quantities of waste natural gas that are not sufficient to be conserved or to support combustion in a flare (CASA (2002)). The processing of sour gas separates the highly toxic hydrogen sulphide (H_2S) from natural gas and a small fraction of the H_2S extracted is then burned in flares to convert it to water and sulfur dioxide. Hydrogen sulphide is about 18 % denser than air at room temperature so burning it also decreases the density of the unconverted H_2S. The subsequent turbulent plume released mixes with the environment thereby decreasing it concentration. If the burning process is not efficient enough the heavy gas can fall back as a fountain to concentrate at ground levels thereby posing a real health hazard to livestock and humans. In the presence of atmospheric inversions, the pollutants could be trapped within or spread along the inversion as a gravity current.

Application of the results of this research to flaring requires extension of this study to the case of double diffusive plumes in uniform and two-layer environments. Double diffusive plumes arise as a result of the diffusion of two diffusive components in the plume. For instance the diffusion of heat and salinity could be used to study plumes which rises due to heat and then collapses as a fountain as the fluid cools due to entrainment of ambient fluid.

The dynamics of such flows are more complicated and have not received greater attention in the literature. The experimental study of Zhang (1996) shows that the reversal of buoyancy which causes an initially positively buoyant thermal-saline plume to collapse at some height occurs within certain regimes of flow governed by the initial salinity, temperature and density differences (see figure 3.5 of Zhang (1996)). The study also shows that the dynamics of such double diffusive plumes are unsteady as compared to fountains and plumes with single diffusive components. For instance the maximum penetration heights of the reversible thermal-saline plumes in their experiments were found to oscillate up and down but the maximum heights increased with time.

Theoretical modeling of double diffusive plumes may require the use of the unsteady equations of motion of the type recently derived by Scase *et al.* (2006*b*) together with the theory of Bloomfield & Kerr (2000). Alternatively, modeling the complicated interaction between the upward and downward flows in a double diffusive plume could be avoided by considering inclined double diffusive plumes in which the source is oriented at a nonzero angle to the vertical (see for example Lane-Serff *et al.* (1993) and Bloomfield & Kerr (2002)). The latter approach not only simplifies the theory but may help make a close comparison with atmospheric plumes from flares which are practically observed to be curved due to the presence of winds.

5.1.2 Relation between plume cap and plume fluxes

The experimental results in chapter 4 show that it is important to study the relation between the cap of a plume in a linearly stratified environment and the fluxes of volume, momentum and buoyancy at the source or at the neutral buoyancy level. This will make comparison of the radial scale of the waves and plume cap much easier. This problem is one of two open questions also posed by Kaye (2008) in a recent review of the literature. It might be possible to split the flow field into two regimes and to treat the upper part as a fountain with its initial momentum and volume fluxes as those at the neutral buoyancy

level.

5.1.3 Numerical simulation of plumes generating axisymmetric waves

As mentioned in section 4.3.4, experiments with larger penetration depths could not be examined because we needed to ensure that there was sufficient vertical and horizontal space for analysing the waves in the limited domain of the tank. This problem may be addressed by conducting numerical simulations of plumes generating axisymmetric waves since larger domain sizes (compared to the maximum height of the plume) could be constructed. In addition, the reflection of waves from the sides and bottom of the tank could also be avoided by setting up appropriate numerical domains. One approach is to use direct numerical simulation (DNS) in which the Navier-Stokes equations are solved without averaging or approximation other than errors due to numerical discretizations (Ferziger & Peric (1997)). Some have used DNS to study the evolution of weak fountains (Lin (2000)). A second approach is to use Large Eddy Simulation (LES) since it is less costly than DNS of the same flow. Some studies have used LES to study the impingement of plane plumes at a thermocline (see figure 5.13 of Lee & Chu (2003)) and so LES could be employed for a further study of the problem.

5.1.4 The obstacle effect

The obstacle effect is another important wave generation mechanism for which laboratory experiments could be conducted to study. The presence of a mean horizontal flow in this mechanism means that a more complicated laboratory setup is needed. One approach is to horizontally tow a plume source across a stationary ambient fluid to mimic a mean horizontal flow.

Appendix A

Turbulent fountain from an area source: Lagrangian approach

In the following, we derive the Lagrangian equations governing the upward motion of a fountain from an area source of radius r_0 and use them to present an alternative method of calculating the maximum penetration height of a fountain in a two-layer environment.

As stated in Section 2.6, Newton's law is applied to a material volume such that the rate of change of the vertical momentum of the plume element is equal to the buoyancy force:

$$\frac{\mathrm{d}M}{\mathrm{d}t} = -F_0. \tag{A.1}$$

Because F_0 is constant, we have

$$M = M_0 - F_0 t. \tag{A.2}$$

The Lagrangian method employs the spreading hypothesis that the plume spreads linearly with height, $\frac{\mathrm{d}b}{\mathrm{d}z} = \beta$, hence

$$b = \beta z + r_0. \tag{A.3}$$

By the chain rule

$$\frac{\mathrm{d}b}{\mathrm{d}t} = \overline{w}\frac{\mathrm{d}b}{\mathrm{d}z} = \beta\overline{w}. \tag{A.4}$$

Multiplying through by b and using (A.2) give

$$\frac{\mathrm{d}}{\mathrm{d}t}\left(\frac{1}{2}b^2\right) = \pi^{-1/2}\beta(M_0 - F_0 t)^{1/2}.$$

Integrating both sides give

$$\frac{1}{2}b^2 = -\frac{2}{3}\pi^{-1/2}\beta F_0^{-1}(M_0 - F_0 t)^{3/2} + C,$$

where C is a constant of integration. At $t = 0$, $b = r_0$ so we have

$$C = \frac{1}{2}r_0^2 + \frac{2}{3}\pi^{-1/2}\beta F_0^{-1} M_0^{3/2}.$$

Thus,

$$\frac{1}{2}b^2 = \frac{1}{2}r_0^2 + \frac{2\beta}{3\sqrt{\pi}}\frac{M_0^{3/2}}{F_0}\left[1 - \left(1 - \frac{F_0 t}{M_0}\right)^{3/2}\right], \tag{A.5}$$

from which it follows that

$$b = \left\{r_0^2 + \frac{4\beta}{3\sqrt{\pi}}\frac{M_0^{3/2}}{F_0}\left[1 - \left(1 - \frac{F_0 t}{M_0}\right)^{3/2}\right]\right\}^{1/2}. \tag{A.6}$$

The relation between z and t can be obtained from (A.6) and the equation

$$z = \frac{1}{\beta}(b - r_0). \tag{A.7}$$

At the maximum penetration height, $z_{\max}$, the momentum flux goes to zero

($M = 0$) and so from (A.2) and (A.7), we get

$$t_{\max} = \frac{M_0}{F_0}, \tag{A.8}$$

$$z_{\max} = \left\{ \left[\left(\frac{r_0}{\beta} \right)^2 + \frac{4}{3\beta\sqrt{\pi}} \frac{M_0^{3/2}}{F_0} \right]^{1/2} - \left(\frac{r_0}{\beta} \right) \right\}, \tag{A.9}$$

where $t_{\max}$ is the time taken to reach the maximum height. From (A.4) we have

$$\overline{w} = \frac{1}{\beta} \frac{\mathrm{d}b}{\mathrm{d}t},$$

and differentiating (A.6) with respective to t we get after some algebra

$$\overline{w} = \pi^{-1/2} M_0^{1/2} \left(1 - \frac{F_0 t}{M_0} \right)^{1/2} \left\{ r_0^2 + \frac{4\beta}{3\sqrt{\pi}} \frac{M_0^{3/2}}{F_0} \left[1 - \left(1 - \frac{F_0 t}{M_0} \right)^{3/2} \right] \right\}^{-1/2} \tag{A.10}$$

From equations (A.6) and (A.10), the volume flux, $Q = \pi b^2 \overline{w}$, is given by

$$Q = \pi^{1/2} M_0^{1/2} \left(1 - \frac{F_0 t}{M_0} \right)^{1/2} \left\{ r_0^2 + \frac{4\beta}{3\sqrt{\pi}} \frac{M_0^{3/2}}{F_0} \left[1 - \left(1 - \frac{F_0 t}{M_0} \right)^{3/2} \right] \right\}^{1/2}. \tag{A.11}$$

As expected, (A.11) predicts that the volume flux decreases toward zero at the maximum height, indicating a negative entrainment at the region where the fountain fluid begins to fall toward the source. This also means that there is a critical time when the volume flux is maximum. This critical time, t_c, can be explicitly calculated by differentiating (A.11) with respect to t and setting the resulting expression to zero.

Let $\tau = 1 - \frac{F_0 t}{M_0}$ and $l_s = \frac{4\beta}{3\sqrt{\pi}} \frac{M_0^{3/2}}{F_0}$. Then

$$Q = \pi^{1/2} M_0^{1/2} \tau^{1/2} \left\{ r_0^2 + l_s \left[1 - \tau^{3/2} \right] \right\}^{1/2}. \tag{A.12}$$

Differentiating give

$$\frac{\mathrm{d}Q}{\mathrm{d}\tau} = \frac{1}{2}\sqrt{\pi}M_0^{1/2}\tau^{-1/2}\left[r_0^2 + l_s\left(1-\tau^{3/2}\right)\right]^{1/2} - \frac{3}{4}\sqrt{\pi}M_0^{1/2}l_s\tau\left[r_0^2 + l_s\left(1-\tau^{3/2}\right)\right]^{-1/2}.$$

At the critical time, t_c, $\mathrm{d}Q/\mathrm{d}\tau = 0$, and we get the nondimensional critical time, τ_c, as

$$\tau_c = \left(\frac{2}{5}\right)^{2/3}\left(1+\frac{r_0^2}{l_s}\right)^{2/3}.$$

But $t_c = \frac{M_0}{F_0}(1-\tau_c)$, so

$$t_c = \frac{M_0}{F_0}\left\{1-\left(\frac{2}{5}\right)^{2/3}\left[1+\frac{3\sqrt{\pi}}{4\beta}\frac{F_0 r_0^2}{M_0^{3/2}}\right]^{2/3}\right\}. \tag{A.13}$$

Substituting t_c into (A.11) gives the maximum volume flux:

$$Q_{\max} = \pi^{1/2}M_0^{1/2}\left(1-\frac{F_0 t_c}{M_0}\right)^{1/2}\left\{r_0^2 + \frac{4\beta}{3\sqrt{\pi}}\frac{M_0^{3/2}}{F_0}\left[1-\left(1-\frac{F_0 t_c}{M_0}\right)^{3/2}\right]\right\}^{1/2} \tag{A.14}$$

The relations derived for a fountain from a point source of flow in Section 2.6.2 are retrieved by setting $r_0 \to 0$ in the equations above.

The relations above may also be written in terms of z using equations (A.6) and (A.7) to get

$$b = \beta z + r_0 = \left[r_0^2 + l_s\left(1-\tau^{3/2}\right)\right]^{1/2},$$

and hence

$$\tau = \left\{1-\left(\frac{3\sqrt{\pi}}{4}\right)\left(\frac{F_0}{M_0^{3/2}}\right)\left[\beta z^2 + 2r_0 z\right]\right\}^{2/3}. \tag{A.15}$$

So from (A.12) we get the volume flux in terms of z:

$$Q(z) = \pi^{1/2} M_0^{1/2} (\beta z + r_0) \left\{ 1 - \left(\frac{3\sqrt{\pi}}{4} \right) \left(\frac{F_0}{M_0^{3/2}} \right) \left[\beta z^2 + 2 r_0 z \right] \right\}^{1/3} . \quad \text{(A.16)}$$

Using $M = M_0(1 - F_0 t/M_0) = M_0 \tau$ and equation (A.15) we get the momentum flux in terms of z:

$$M(z) = M_0 \left\{ 1 - \left(\frac{3\sqrt{\pi}}{4} \right) \left(\frac{F_0}{M_0^{3/2}} \right) \left[\beta z^2 + 2 r_0 z \right] \right\}^{2/3} . \quad \text{(A.17)}$$

The maximum penetration height and maximum volume flux remain the same since they are in terms of the source variables.

A.1 The maximum height in a two-layer ambient: Method 2

In the following, we outline a second method of calculating the maximum penetration height of a fountain in a two-layer ambient without making a virtual origin correction at the interface.

The mean properties of the fountain beyond the interface may be determined by using the equations for a fountain from an area source derived above and replacing the source quantities by those at the interface. In particular the maximum penetration height of the fountain beyond the interface can be found from equation (A.9) by replacing the source radius and fluxes by those at the interface to get (for an interface at a height $z = H$)

$$z_{\max,i} = \left[\left(\frac{b_i}{\beta} \right)^2 + \frac{4}{3\beta\sqrt{\pi}} \frac{M_i^{3/2}}{F_i} \right]^{1/2} - \left(\frac{b_i}{\beta} \right) \quad \text{(A.18)}$$

where F_i is given by equation (2.83) and

$$b_i = \beta H + r_0, \tag{A.19}$$

$$Q_i = \pi^{1/2} M_0^{1/2} (\beta H + r_0) \left\{ 1 - \left(\frac{3\sqrt{\pi}}{4} \right) \left(\frac{F_0}{M_0^{3/2}} \right) \left[\beta H^2 + 2 r_0 H \right] \right\}^{1/3} \tag{A.20}$$

$$M_i = M_0 \left\{ 1 - \left(\frac{3\sqrt{\pi}}{4} \right) \left(\frac{F_0}{M_0^{3/2}} \right) \left[\beta H^2 + 2 r_0 H \right] \right\}^{2/3}. \tag{A.21}$$

Substituting these expressions into (A.18) gives the height in terms of the source parameters:

$$z_{\max,i} = \left[\left(H + \frac{r_0}{\beta} \right)^2 + z_0 \right]^{1/2} - \left(H + \frac{r_0}{\beta} \right), \tag{A.22}$$

where

$$z_0 = \frac{4}{3\beta\sqrt{\pi}} \frac{M_0^{3/2} Q_0}{F_0} \frac{L_0}{\left[Q_0 - \tilde{\varepsilon} \pi^{1/2} M_0^{1/2} (\beta H + r_0) L_0^{1/3} \right]},$$

and

$$L_0 = \left[1 - \frac{3\sqrt{\pi} F_0}{4 M_0^{3/2}} (\beta H^2 + 2 r_0 H) \right].$$

We observe that for a fountain in a one layer fluid from an area source of radius r_0, equation (A.22) reduces to (A.9) since $\tilde{\varepsilon} = (\rho_1 - \rho_2)/(\rho_1 - \rho_0) \to 0$, $H \to 0$ and $L_0 \to 1$. Similarly, the expression for the maximum height for a fountain from a point source in a one layer fluid (equation (2.78)) is recovered since in addition $r_0 \to 0$.

Thus, the maximum penetration height of a fountain from an area source in a two-layer fluid with density interface at $z = H$ is given by

$$z_{\max,2} = z_{\max,i} + H = \left[\left(H + \frac{r_0}{\beta} \right)^2 + z_0 \right]^{1/2} - \left(\frac{r_0}{\beta} \right). \tag{A.23}$$

Appendix B

Scaling analyses: Radial intrusion in a two-layer environment

Consider an axisymmetric intrusion of density ρ_{in} from a source of constant volume flux Q_{in} into a two-layer environment with a top layer of density ρ_1 and a lower layer of density ρ_2. Let h be the height of the intrusion at time t and H be the distance of the interface from the surface as shown in figure B.1. We assume small density differences between the intrusion and the ambient and neglect surface tension effects.

The conservation of volume relation is given by

$$Q_{in}t \sim R^2 h, \tag{B.1}$$

where R is the position of the front at time t. The pressure distribution within the intrusion can be obtained from the hydrostatic equation ($\mathrm{d}p/\mathrm{d}z = -\rho_{in}g$) such that

$$p = \rho_1 g H - \rho_{in} g z + g(\rho_{in} - \rho_1) h_1. \tag{B.2}$$

A relation between h_1 and h is obtained via a hydrostatic balance (Timothy (1977)):

$$h_1 = \left(\frac{\rho_2 - \rho_{in}}{\rho_2 - \rho_1}\right) h. \tag{B.3}$$

Thus, from equation (B.2) we get the pressure distribution

$$p = \rho_1 g H - \rho_{in} g z + \rho_{in} \varepsilon g'_{in} h \tag{B.4}$$

where $\varepsilon = (\rho_2 - \rho_{in})/(\rho_2 - \rho_1)$ and $g'_{in} = g(\rho_{in} - \rho_1)/\rho_{in}$. The radial pressure gradient is therefore given by

$$\frac{\partial p}{\partial r} = \rho_{in} \varepsilon g'_{in} \frac{\partial h}{\partial r}. \tag{B.5}$$

At the interface, $z = 0$, the pressure scales as $p \sim \rho_{in} \varepsilon g'_{in} h$ and so the horizontal driving pressure force should scale as the product of the pressure and the cross-sectional area:

$$F_p \sim \rho_{in} \varepsilon g'_{in} R h^2. \tag{B.6}$$

In the inertia-buoyancy regime, the opposing force is the inertia force, F_{in}, which scales as the product of the mass and acceleration:

$$F_{in} \sim \rho_{in} h R^3 / t^2. \tag{B.7}$$

Balancing equations (B.6) and (B.7) and using equation (B.1), we get

$$R(t) \sim (\varepsilon g'_{in} Q_{in})^{1/4} t^{3/4}. \tag{B.8}$$

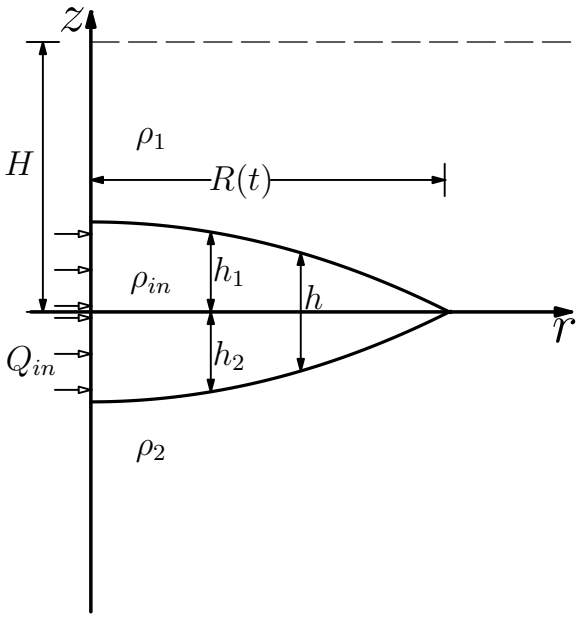

Figure B.1: Schematic of intrusion into a two-layer environment

Appendix C

Axisymmetric internal gravity waves

The equations governing the motion of axisymmetric flow of an inviscid incompressible fluid without rotation in cylindrical coordinates $(r, \bar{\theta}, z)$ and with velocity field $\mathbf{U} = (u, 0, w)$ are given by equations (2.1)-(2.4) (they are repeated here for convenience):

$$\rho\left(\frac{\partial u}{\partial t} + u\frac{\partial u}{\partial r} + w\frac{\partial u}{\partial z}\right) = -\frac{\partial p}{\partial r}, \tag{C.1}$$

$$\rho\left(\frac{\partial w}{\partial t} + u\frac{\partial w}{\partial r} + w\frac{\partial w}{\partial z}\right) = -g\rho - \frac{\partial p}{\partial z}, \tag{C.2}$$

$$\frac{\partial (ru)}{\partial r} + \frac{\partial (rw)}{\partial z} = 0, \tag{C.3}$$

$$\frac{\partial \rho}{\partial t} + u\frac{\partial \rho}{\partial r} + w\frac{\partial \rho}{\partial z} = 0. \tag{C.4}$$

For small amplitude internal gravity waves, the nonlinear advection terms can be neglected (Kundu (1990), page 234). Also using the Boussinesq approxi-

mation, the equations reduce to

$$\rho_{00}\frac{\partial u}{\partial t} = -\frac{\partial p}{\partial r}, \tag{C.5}$$

$$\rho_{00}\frac{\partial w}{\partial t} = -g\rho - \frac{\partial p}{\partial z}, \tag{C.6}$$

$$\frac{\partial (ru)}{\partial r} + \frac{\partial (rw)}{\partial z} = 0, \tag{C.7}$$

$$\frac{\partial \rho}{\partial t} + u\frac{\partial \rho}{\partial r} + w\frac{\partial \rho}{\partial z} = 0. \tag{C.8}$$

The pressure and density are decomposed into a background state (variables with overbars) and a fluctuating state such that

$$\rho = \overline{\rho}(z) + \rho' \quad \text{and} \quad \overline{p}(z) + p'. \tag{C.9}$$

Substituting these into the equations and neglecting the nonlinear terms in the density equation results in the equations governing the motion of inviscid and incompressible small amplitude axisymmetric internal gravity waves with no background flow:

$$\frac{\partial u}{\partial t} + \frac{1}{\rho_{00}}\frac{\partial p}{\partial r} = 0, \tag{C.10}$$

$$\rho_{00}\frac{\partial w}{\partial t} + \frac{\partial p}{\partial z} + \rho g = 0, \tag{C.11}$$

$$\frac{\partial \rho}{\partial t} + w\frac{\mathrm{d}\bar{\rho}}{\mathrm{d}z} = 0, \tag{C.12}$$

$$\frac{1}{r}\frac{\partial (ru)}{\partial r} + \frac{\partial w}{\partial z} = 0, \tag{C.13}$$

where we have dropped the primes on the fluctuating variables for convenience.

In the following, we will combine the above equations into a single equation in terms of the stream function, $\psi(r, z, t)$. Taking the derivative of (C.10) with

respect to z and the derivative of (C.11) with respect to r we get respectively

$$\rho_{00}\frac{\partial^2 u}{\partial z \partial t} + \frac{\partial^2 p}{\partial z \partial r} = 0, \tag{C.14}$$

$$\rho_{00}\frac{\partial^2 w}{\partial r \partial t} + \frac{\partial^2 p}{\partial z \partial r} + g\frac{\partial \rho}{\partial r} = 0. \tag{C.15}$$

Equation (C.14) minus (C.15) gives

$$\rho_{00}\left(\frac{\partial^2 u}{\partial z \partial t} - \frac{\partial^2 w}{\partial r \partial t}\right) - g\frac{\partial \rho}{\partial r} = 0. \tag{C.16}$$

Taking the derivative of (C.12) with respect to r and multiplying through by g we get

$$g\frac{\partial^2 \rho}{\partial r \partial t} + g\frac{\mathrm{d}\overline{\rho}}{\mathrm{d}z}\frac{\partial w}{\partial r} = 0. \tag{C.17}$$

Taking the derivative of (C.16) with respect to t and adding it to (C.17) we get

$$\rho_{00}\left(\frac{\partial^3 u}{\partial t^2 \partial z} - \frac{\partial^3 w}{\partial t^2 \partial r}\right) + g\frac{\mathrm{d}\overline{\rho}}{\mathrm{d}z}\frac{\partial w}{\partial r} = 0. \tag{C.18}$$

This is rewritten as

$$\frac{\partial^2}{\partial t^2}\left(\frac{\partial u}{\partial z} - \frac{\partial w}{\partial r}\right) - N^2\frac{\partial w}{\partial r} = 0, \tag{C.19}$$

where

$$N^2 = -\frac{g}{\rho_{00}}\frac{\mathrm{d}\overline{\rho}}{\mathrm{d}z}. \tag{C.20}$$

For an incompressible fluid, we have the continuity equation $\nabla \cdot \mathbf{U} = 0$. Implicitly defining the stream function as $\mathbf{U} = \nabla \times (\psi\hat{\bar{\theta}})$ satisfies the continuity equation, where $\hat{\bar{\theta}}$ is a unit vector in the direction of $\bar{\theta}$. The radial and vertical

velocity components are respectively given by

$$u = -\frac{\partial \psi}{\partial z}, \quad w = \frac{1}{r}\frac{\partial (r\psi)}{\partial r}. \tag{C.21}$$

Substituting (C.21) into (C.19) we get (2.113):

$$\frac{\partial^2}{\partial t^2}\left[\frac{\partial^2 \psi}{\partial z^2} + \frac{\partial}{\partial r}\left(\frac{1}{r}\frac{\partial (r\psi)}{\partial r}\right)\right] + N^2 \frac{\partial}{\partial r}\left(\frac{1}{r}\frac{\partial (r\psi)}{\partial r}\right) = 0. \tag{C.22}$$

C.1 Dispersion relation

We seek solutions of the form

$$\psi(r, z, t) = \hat{\psi}(r) e^{i(k_z z - \omega t)}, \tag{C.23}$$

and so (C.22) becomes

$$\begin{aligned} \frac{\mathrm{d}^2 \hat{\psi}}{\mathrm{d}r^2} + \frac{1}{r}\frac{\mathrm{d}\hat{\psi}}{\partial r} + \left(\frac{k_z^2 \omega^2}{N^2 - \omega^2} - \frac{1}{r^2}\right)\hat{\psi} = 0, \\ \implies r^2 \frac{\mathrm{d}^2 \hat{\psi}}{\mathrm{d}r^2} + r\frac{\mathrm{d}\hat{\psi}}{\mathrm{d}r} + \left(\frac{k_z^2 \omega^2}{N^2 - \omega^2} r^2 - 1\right)\hat{\psi} = 0, \\ \implies r^2 \frac{\mathrm{d}^2 \hat{\psi}}{\mathrm{d}r^2} + r\frac{\mathrm{d}\hat{\psi}}{\mathrm{d}r} + \left(k^2 r^2 - 1\right)\hat{\psi} = 0, \end{aligned} \tag{C.24}$$

where

$$\begin{aligned} k^2 = \frac{k_z^2 \omega^2}{N^2 - \omega^2} \\ \implies \omega^2 = N^2 \frac{k^2}{k_z^2 + k^2}, \end{aligned} \tag{C.25}$$

is the dispersion relation.

C.2 Polarization relations

We observe that equation (C.24) is the Bessel equation of the first kind and order one with argument kr; therefore

$$\hat{\psi}(r) = J_1(kr). \tag{C.26}$$

Thus, the stream function takes the form

$$\psi = A_\psi J_1(kr) e^{i(k_z z - \omega t)}, \tag{C.27}$$

so that from (C.21), we get

$$u = -ik_z A_\psi J_1(kr) e^{i(k_z z - \omega t)}.$$

Thus,

$$u = A_u J_1(kr) e^{i(k_z z - \omega t)}.$$

The amplitude of the horizontal velocity is related to the stream function amplitude by

$$A_u = -ik_z A_\psi. \tag{C.28}$$

Now

$$\frac{\partial(r\psi)}{\partial r} = A_\psi J_1(kr) e^{i(k_z z - \omega t)} + A_\psi e^{i(k_z z - \omega t)} \left[k J_0(kr) - \frac{J_1(kr)}{r} \right],$$

since by the properties of Bessel functions

$$\frac{\mathrm{d}J_1(kr)}{\mathrm{d}r} = J_0(kr) - \frac{J_1(kr)}{r}. \tag{C.29}$$

Thus

$$w = A_w J_0(kr) e^{i(k_z z - \omega t)}.$$

The amplitude of the vertical velocity is related to the stream function amplitude by

$$A_w = kA_\psi. \tag{C.30}$$

From (C.28) and (C.30) we get

$$A_u = -i\frac{k_z}{k} A_w. \tag{C.31}$$

We now rewrite the amplitudes in terms of the vertical displacement amplitude. The vertical displacement, ξ, is implicitly defined by $w = \frac{\partial \xi}{\partial t}$, so that

$$A_w = -i\omega A_\xi. \tag{C.32}$$

From the dispersion relation $\cos\Theta = \frac{\omega}{N}$, we get

$$A_w = -iN\cos(\Theta) A_\xi. \tag{C.33}$$

From (C.30) we get

$$A_\psi = -i\frac{\omega}{k} A_\xi, \tag{C.34}$$

or in terms of Θ

$$A_\psi = -i\frac{N}{k}\cos(\Theta) A_\xi. \tag{C.35}$$

From (C.31) we get

$$A_u = -i\frac{k_z}{k}(-i\omega A_\xi) = -\frac{k_z \omega}{k} A_\xi. \tag{C.36}$$

From the dispersion relation we have

$$\frac{\omega k_z}{k} = \sqrt{N^2 - \omega^2} = N \sin\Theta,$$

so

$$A_u = -N \sin(\Theta) A_\xi. \tag{C.37}$$

Let

$$p = A_p J_0(kr) e^{i(k_z z - \omega t)},$$

then from (C.10) we have

$$\frac{\partial}{\partial r}\left[A_p J_0(kr) e^{i(k_z z-\omega t)}\right] \;=\; -\rho_{00}\left[(-i\omega) A_u J_1(kr) e^{i(k_z z-\omega t)}\right].$$

From properties of Bessel functions

$$-\frac{\mathrm{d}J_0(kr)}{\mathrm{d}r} = kJ_1(kr), \tag{C.38}$$

therefore

$$A_p \;=\; -i\frac{\omega\rho_{00}}{k} A_u.$$

Using (C.36) we get

$$A_p = i\rho_{00}\frac{N^2}{k}\sin(\Theta)\cos(\Theta) A_\xi.$$

By definition, the perturbation density ρ is given by $\rho = -\frac{\mathrm{d}\overline{\rho}}{\mathrm{d}z}\xi$, so that

$$A_\rho = -\frac{\mathrm{d}\overline{\rho}}{\mathrm{d}z} A_\xi = \frac{\rho_{00}}{g} N^2 A_\xi. \tag{C.39}$$

By definition

$$\Delta N^2 = -\frac{\rho_{00}}{g}\frac{\partial \rho}{\partial z}, \tag{C.40}$$

and so from (C.11), we have

$$-\frac{\rho_{00}}{g}\frac{\partial \rho}{\partial z} = \frac{\partial^2 w}{\partial t \partial z} + \frac{1}{\rho_{00}}\frac{\partial^2 p}{\partial z^2},$$

hence

$$\Delta N^2 = \frac{\partial^2 w}{\partial t \partial z} + \frac{1}{\rho_{00}}\frac{\partial^2 p}{\partial z^2}. \tag{C.41}$$

The amplitude is

$$A_{\Delta N^2} = \left[\omega k_z A_w - \frac{k_z^2}{\rho_{00}} A_p\right] = -iN^2 k \tan(\Theta) A_\xi,$$

where we have used the fact that $\tan\Theta = k_z/k$. Now

$$N_t^2 = \frac{\partial \Delta N^2}{\partial t},$$

and so we get

$$A_{N_t^2} = -k_z \omega N^2 A_\xi = -kN^3 \sin(\Theta) A_\xi.$$

Appendix D

Average energy flux of waves

For a bounded domain of radius R, the energy flux over any circular area is given by

$$F_E = \int_0^{2\pi} \int_0^R (wp) r \mathrm{d}r \mathrm{d}\bar{\theta} = 2\pi \int_0^R (wp) r \mathrm{d}r \tag{D.1}$$

since both the vertical velocity w and perturbation pressure p are independent of the radial coordinate $\bar{\theta}$ for axisymmetric waves. Because the waves are assumed axisymmetric, we compute the average energy flux using Bessel series and define

$$w = \sum_n \sum_m \frac{1}{2} W_{nm} J_0(k_n r) e^{i(k_z z - \omega_m t)} + cc, \tag{D.2}$$

$$p = \sum_n \sum_m \frac{1}{2} P_{nm} J_0(k_n r) e^{i(k_z z - \omega_m t)} + cc, \tag{D.3}$$

where J_0 is the Bessel function of the first kind and order zero, W_{nm} and P_{nm} are the amplitudes of the w and p fields; k_z and ω_m are the vertical wavenumber and frequencies respectively. Substituting (D.2) and (D.3) into (D.1) and applying the orthogonality property of Bessel functions we get

$$F_E = 2\pi \sum_n \sum_m P_{nm} W_{nm} \cos^2(k_z z - \omega_m t) \int_0^R [J_0(\alpha_n r/R)]^2 r \mathrm{d}r. \tag{D.4}$$

Using the properties of Bessel functions, this simplifies to

$$F_E = \pi R^2 \sum_n \sum_m P_{nm} W_{nm} \cos^2(k_z z - \omega_m t) J_1^2(\alpha_n), \tag{D.5}$$

where J_1 is the Bessel function of the first kind and order one.

The polarization relations of linear wave theory for each n and m gives

$$P_{nm} W_{nm} = \frac{\rho_0 N^3 \cos\Theta_m \sin 2\Theta_m}{2k_n} |A_{\xi nm}|^2,$$

where $k_n = \alpha_n / R$, Θ_m are the angles of propagation of each wave beam about the vertical and $A_{\xi nm}$ are the vertical displacement amplitudes. Equation (D.5) becomes

$$F_E = \frac{1}{2} \pi R^2 \rho_0 N^3 \sum_n \sum_m \cos\Theta_m \sin 2\Theta_m \cos^2(k_z z - \omega_m t) \frac{|A_{\xi nm}|^2 J_1^2(\alpha_n)}{k_n}. \tag{D.6}$$

Averaging over one wave period we get (2.118):

$$F_{\text{wave}} = \frac{1}{4} \pi R^2 \rho_0 N^3 \sum_n \sum_m \cos\Theta_m \sin 2\Theta_m \frac{|A_{\xi nm}|^2 J_1^2(\alpha_n)}{k_n}. \tag{D.7}$$

Bibliography

Abraham, G. 1963 *Jet diffusion in stagnant ambient fluid,* Technical Report 29. Delft Hydraulics Lab.

Abraham, G. 1967 Jets with negative buoyancy in homogeneous fluids. *Journal of Hydraulic Research* **5, No. 4**, 235–248.

Albertson, M.L., Dai, Y.B., Jensen, R.A. & Hunter, R. 1950 Diffusion of submerged jets. *Trasanctions of ASCE* **No. 2409**, 639–697.

Alexander, M.J. & Barnet, C. 2007 Using satellite observations to constrain parameterizations of gravity wave effects for global models. *J. Atmos. Sci.* **64**, 1652–1665.

Alexander, M.J. & Pfister, L. 1995 Gravity wave momentum flux in the lower stratosphere over convection. *Geophys. Res. Lett.* **22**, 2029–2032.

Ansong, J.K., Kyba, P. & Sutherland, B.R. 2008 Fountains impinging on a density interface. *J. Fluid Mech.* **595**, 115–139.

Baines, W.D. & Chu, V.H. 1996 *"Jets and Plumes" in Environmental Hydraulics*. Kluwer Academic Publishers, Chapter 2.

Baines, W.D., Turner, J.S. & Campbell, I.H. 1990 Turbulent fountains in an open chamber. *Journal of Fluid Mechanics* **212**, 557–592.

Balachandran, N.K. 1980 Gravity waves from thunderstorms. *Monthly Weather Review* **108**, 804–816.

Batchelor, G.K. 1954 Heat convection and buoyancy effects in fluids. *Quart. J. R. Met. Soc.* **80**, 339–358.

Bloomfield, L.J. & Kerr, R.C. 1998 Turbulent fountains in a stratified fluid. *Journal of Fluid Mechanics* **358**, 335–356.

Bloomfield, L.J. & Kerr, R.C. 2000 A theoretical model of a turbulent fountain. *Journal of Fluid Mechanics* **424**, 197–216.

Bloomfield, L.J. & Kerr, R.C. 2002 Inclined turbulent fountains. *Journal of Fluid Mechanics* **451**, 283–294.

Britter, R.E. 1979 The spread of a negatively buoyant plume in a calm environment. *Atmospheric Environment* **13**, 1241–1247.

Britter, R.E. 1989 Atmospheric dispersion of dense gases. *Annual Reviews of Fluid Mechanics* **21**, 317–344.

CASA 2002 Gas flaring and venting in alberta. Report ISBN-1-896250-16-5. Clean Air Stratetic Alliance (CASA), Edmonton-CANADA, report and Recommendations for the Upstream Petroleum Industry by the Flaring/Venting Project Team.

Caulfield, C.P. & Woods, A.W. 1998 Turbulent gravitational convection from a point source in a non-uniformly stratified environment. *J. Fluid Mech.* **360**, 229–248.

Cerasoli, C.P. 1978 Experiments on buoyant-parcel motion and the generation of internal gravity waves. *J. Fluid Mech.* **86**, 247–271.

Chen, J.C. 1980 Studies on gravitational spreading currents. *PhD thesis, California Institute of Technology* .

Clark, T.L, Hauf, T. & Kuettner, J.P. 1986 Convectively forced internal gravity waves: Results from two-dimensional numerical experiments. *Quart. J. Roy. Meteor. Soc.* **112**, 899–925.

Crapper, P.F. & Baines, W.D. 1977 Non-boussinesq forced plumes. *Atmos. Env.* **11**, 415–420.

Crapper, P.F. & Baines, W.D. 1978 Some remarks on non-boussinesq forced plumes. *Atmos. Env.* **12**, 1939–1941.

Curry, M.J. & Murty, R.C. 1974 Thunderstorm-generated gravity waves. *Journal of Atmospheric Sciences* **31**, 1402–1408.

Daviero, G.J., Roberts, J.W. & Mile, K. 2001 Refractive index matching in large-scale experiments. *Experiments in Fluids* pp. 119–126.

Decamp, S., Kozack, C. & Sutherland, B.R. 2008 Three-dimensional schlieren measurements using inverse tomography. *Exps. Fluids* **44(5)**, 747–758.

Dewan, E.M. & Coauthors 1998 MSX satellite observations of thunderstorm-generated gravity waves in mid-wave infrared images of the upper stratosphere. *Geophysical Research Letter* **25**, 939–946.

Didden, N. & Maxworthy, T. 1982 The viscous spreading of plane and axisymmetric gravity currents. *J. Fluid Mech.* **121**, 27–42.

Dohan, K. & Sutherland, B.R 2003 Internal waves generated from a turbulent mixed region. *Physics of Fluids* **15**, 488–498.

Dunkerton, T 1997 The role of gravity waves in the quasi-biennial oscillation. *Journal of Geophysical Research* **102**, 26053–26076.

Ferziger, J.H. & Peric, M. 1997 *Computational methods for fluid dynamics*. Springer.

Fischer, H.B., List, E.J., Imberger, J.S. & Brooks, N.H. 1979 *Mixing in Inland and Coastal Waters*. Academic Press.

Flynn, M.R., Onu, K. & Sutherland, B.R. 2003 Internal wave excitation by a vertically oscillating sphere. *J. Fluid Mech.* **494**, 65–93.

Fovell, R., Durran, D. & Holton, J.R. 1992 Numerical simulations of convectively generated stratospheric gravity waves. *J. Atmos. Sci.* **49**, 1427–1442.

Friedman, P.D. & Katz, J. 2000 Rise height for negatively buoyant fountains and depth of penetration for negatively buoyant jets impinging an interface. *Journal of Fluids Engineering* **122**, 779–782.

Fritts, D.C. & Alexander, M.J. 2003 Gravity wave dynamics and effects in the middle atmosphere. *Reviews of Geophysics* **41(1)**, 3.1–3.64.

Fritts, D.C. & Nastrom, G.D. 1992 Sources of mesoscale variability of gravity waves, ii, frontal, convective, and jet stream excitation. *J. Atmos. Sci.* **49**, 111–127.

Gebhart, B. 1961 *Heat Transfer*. McGraw-Hill.

Gebhart, B., L., Pera & Schorr, A.W. 1970 Steady laminar natural convection plumes above a horizontal line heat source. *Int. J. Heat Mass Transfer* **13**, 161.

Gebhart, B. & Pera, L. 1971 The nature of vertical natural convection flows resulting from the combined buoyancy effects of thermal and mass diffusion. *Int. J. Heat Mass Transfer* **14**, 2025–2050.

Gedzelman, S.D. 1983 Short-period atmospheric gravity waves. *Monthly Weather Review* **111(6)**, 1293–1299.

Grachev, A.I., Danilov, S.D., Kulichkov, S.N. & Svertilov, A.I. 1995 Main characteristics of internal gravity waves from convective storms in the lower troposphere. *Atmospheric and oceanic physics* **30(6)**, 725–733.

Henderson-Sellers, B. 1981 Shape constants for plume models. *Boundary-Layer Meteorology* **21**, 105–114.

Hunt, G.R. & Kaye, N.B. 2001 Virtual origin correction for lazy turbulent plumes. *J. Fluid Mech.* **435**, 377–396.

Hunt, G.R. & Kaye, N.B. 2005 Lazy plumes. *J. Fluid Mech.* **533**, 329–338.

Ivey, G.N. & Blake, S. 1985 Axisymmetric withdrawal and inflow in a density-stratified container. *J. Fluid Mech.* **161**, 115–137.

Jaluria, Y. 1980 *Natural Convection. Heat and Mass Transfer*. Pergamon Press.

Kapoor, K & Jaluria, Y. 1993 Penetrative convection of a plane turbulent wall jet in a two-layer thermally stable environment: a problem in enclosure fires. *International Journal of Heat Mass Transfer* **36**, 155–167.

Karoly, D.J., Roff, G.L. & Reeder, M.J. 1996 Gravity wave activity associated with tropical convection detected in toga coare sounding data. *Geophys. Res. Lett.* **23(3)**, 261–264.

Kaye, N.B. 2008 Turbulent plumes in stratified environments: A review of recent work. *Atmosphere-Ocean* **46(4)**, 433–441.

Kotsovinos, N.E. 2000 Axisymmetric submerged intrusion in stratified fluid. *J. Hydraulic Engineering, ASCE* **126**, 446–456.

Kumar, K.K. 2007 VHF radar investigations on the role of mechanical oscillator effect in exciting convectively generated gravity waves. *Geophysical Research Letters, L01803, doi:10.1029/2006GL027404* **34**.

Kundu, P.K. 1990 *Fluid Mechanics*. Academic Press.

Lane, T.P. 2008 The vortical response to penetrative convection and the associated gravity-wave generation. *Atmos. Sci. Let.* **9**, 103–110.

Lane, T.P., Reeder, M.J. & Clark, T.L. 2001 Numerical modeling of gravity wave generation by deep tropical convection. *J. Atmos. Sci.* **58**, 1249–1274.

Lane-Serff, G.F., Linden, P.F. & Hillel, M. 1993 Forced, angled plumes. *Journal of Hazardous Materials* **33**, 75–99.

Larsen, M.F., Swartz, W.E. & Woodman, R.F. 1982 Gravity-wave generation by thunderstorms observed with a vertically-pointing 430 mhz radar. *Geophys. Res. Lett.* **9(5)**, 571–574.

Lee, J.H.W. & Chu, V.H. 2003 *Turbulent buoyant jets and plumes: A langrangian approach*. Kluwer Academic Publishers.

Lemkert, C.J. & Imberger, J. 1993 Axisymmetric intrusive gravity currents in linearly stratified fluids. *J. Hydraulic Engineering, ASCE* **119(6)**, 662–679.

Lin, W. 2000 Scaling analysis and direct simulation of unsteady weak fountains and natural convection flow. *Ph.D thesis, The university of Sydney, Australia* .

Lin, Y.J.P. & Linden, P.F. 2005 The entrainment due to a turbulent fountain at a density interface. *Journal of Fluid Mechanics* **542**, 25–52.

Linden, P.F. 2000 Convection in the environment. In *Perspectives in Fluid Mechanics. A collective introduction to current research* (eds. G.K. Batchelor, H.K. Moffat, M.G. Worster), pp. 289–345. Cambridge University Press.

List 1982 *Mechanics of turbulent buoyant jets and plumes.* Turbulent Buoyant Jets and Plumes. Pergamon.

Lister, J.R. & Kerr, R.C. 1989 The propagation of two-dimensional and axisymmetric gravity currents at a fluid interface. *J. Fluid Mech.* **203**, 215–249.

Loitsyanskii, L.G. 1966 *Mechanics of liquids and gases*. Pergamon Press.

Lu, D., VanZandt, T.E. & Clark, W.L. 1984 VHF doppler radar observations of buoyancy waves associated with thunderstorms. *J. Atmos. Sci.* **41(2)**, 272–282.

McDougall, T.J. 1981 Negatively buoyant vertical jets. *Tellus* **33**, 313–320.

McLandress, C. 1998 On the importance of gravity waves in the middle atmosphere and their parameterization in the general circulation models. *J. Atmos. and Sol.-Terr. Phys.* **60**, 1357–1383.

McLaren, T.I., Pierce, A.D., Fohl, T. & B.L., Murphy 1973 An investigation of internal gravity waves generated by a buoyantly rising fluid in a stratified medium. *J. Fluid Mech.* **57**, 229–241.

MEDOC Group 1970 Observations of formation of deep water in the mediterranean. *Nature* **277**, 1037–1040.

Mellor, G.L. 1996 *Introduction to physical oceanography*. Springer.

Michaelian, M.E., Maxworthy, T. & Redekopp, L.G. 2002 The coupling between turbulent, penetrative convection and internal waves. *Euro. J. Mech. B/Fluids* **21**, 1–28.

Middleton, J.H. 1975 The asymptotic behaviour of a starting plume. *Journal of Fluid Mechanics* **72**, 753–771.

Mizushina, T., Ogino, F., Takeuchi, H. & Ikawa, H. 1982 An experimental study of vertical turbulent jet with negative buoyancy. *Warme and Stoffubertragung (Thermo and Fluid Dynamics)* **16**, 15–21.

Mollendorf, J.C. & Gebhart, B. 1973 Thermal buoyancy in round laminar vertical jets. *Int. J. Heat Mass Transfer* **16**, 735.

Morton, B.R. 1959*a* The ascent of turbulent forced plumes in a calm atmosphere. *International Journal of Air Pollution* **1**, 184–197.

Morton, B.R. 1959*b* Forced plumes. *Journal of Fluid Mechanics* **5**, 151–163.

Morton, B.R. 1967 Entrainment models for laminar jets, plumes and wakes. *The Physics of Fluids* **10 No. 10**, 2120–2127.

Morton, B.R. 1971 The choice of conservation equations for plume models. *J. Geophys. Res.* **76 No. 30**, 7409–7416.

Morton, B.R. & Middleton, J. 1973 Scale diagrams for forced plumes. *Journal of Fluid Mechanics* **58**, 165–176.

Morton, B.R., Taylor, G. & Turner, J.S. 1956 Turbulent gravitational convection from maintained and instantaneous sources. *Proceedings of the Royal Society, Series A* **234**, 1–23.

Mowbray, D.E. & Rarity, B.S.H. 1967a A theoretical and experimental investigation of the phase configuration of internal waves of small amplitude in a density stratified liquid. *J. Fluid Mech.* **28**, 1–16.

Noutsopoulos, G. & Nanou, K. 1986 The round jet in a two-layer stratified ambient. *Proc. Intl Symp. on Buoyant Flows: Athens-Greece* **1-5**, 165–183.

Onu, K., Flynn, M.R. & Sutherland, B.R. 2003 Schlieren measurement of axisymmetric internal wave amplitudes. *Experiments in Fluids* **35**, 24–31.

Oster, G. 1965 Density gradients. *Scientific American* **213**, 70.

Paluszkiewcz, T. & Garwood, R.W. 1994 Deep convective plumes in the ocean. *Oceanography* **7**, 37–44.

Pandya, R.E. & Alexander, M.J. 1999 Linear stratospheric gravity waves above convective thermal forcing. *J. Atmos. Sci.* **56**, 2434–2446.

Papanicolaou, P.N. & List, E.J. 1988 Investigations of round vertical turbulent buoyant jets. *J. Fluid Mech.* **195**, 341–391.

Pfister, L., Chan, K.R., Bui, T.P., Bowen, S., Legg, M., Gary, B., Kelly, K., Proffitt, M. & Starr, W. 1993*a* Gravity waves generated by a tropical cyclone during the step tropical field program: A case study. *J. Geophys. Res.* **98, No. D5**, 8611–8638.

Pfister, L., Scott, S. & Loewenstein, M. 1993*b* Mesoscale disturbances in the tropical stratosphere excited by convection: observations and effects

on the stratospheric momentum budget. *J. Atmos. Sci.* **50, No. 8**, 1058–1075.

Pierce, A.D. & Coroniti, S.C. 1966 A mechanism for the generation of acoustic-gravity waves during thunderstorm formation. *Nature* **210**, 1209–1210.

Priestley, C.H.B. & Ball, F.K. 1955 Continuous convection from an isolated source of heat. *Quarterly Journal of Royal Meteorological Society* **81, No.384**, 144–156.

Rajaratnam, N. 1976 *Turbulent jets*. Elsevier.

Rawn, A.M., Bowerman, F.R. & Brooks, N.H. 1960 Diffusers for disposal of sewage in sea water. *Journal of the sanitary engineering division:Proceedings of the ASCE* pp. 65–105.

Rodi, W. 1982 *Turbulent buoyant jets and plumes*. Pergamon Press.

Rooney, G.G. & Linden, P.F. 1996 Similarity considerations for non-boussinesq plumes in an unstratified environment. *J. Fluid Mech.* **318**, 237–250.

Rouse, H., Yih, C.S. & Humphreys, H.W. 1952 Gravitational convection from a boundary source. *Tellus* **4**, 201.

Scase, M.M., Caulfield, C.P. & Dalziel, S.B. 2006*a* Boussinesq plumes and jets with decreasing source strengths in stratified environments. *J. Fluid Mech.* **563**, 463–472.

Scase, M.M., Caulfield, C.P., Dalziel, S.B. & Hunt, J.C.R. 2006*b* Time-dependent plumes and jets with decreasing source strengths. *J. Fluid Mech.* **563**, 443–461.

Scase, M.M., Caulfield, C.P., Linden, P.F. & Dalziel, S.B. 2007 Local implications for self-similar turbulent plume models. *J. Fluid Mech.* **575**, 257–265.

Schlichting, H. 1968 *Boundary-Layer Theory*. McGraw-Hill Book Company.

Schmidt, W. 1941 Turbulent propagation of a stream of air. *Z. Angew. Math. Mech.* **21**, 265,351.

Schott, F., Visbeck, M. & Fischer, J. 1993 Observations of vertical currents and convection in the central greenland sea during the winter of 1988/89. *J. Geophys. Res.* **98(C8)**, 14401–14421.

Scorer, R.S. 1957 Experiments on convection of isolated masses of buoyant fluid. *J. Fluid Mech.* **2**, 583–594.

Scorer, R.S. 1959 The behaviour of chimney plumes. *International Journal of Air Pollution* **1**, 198–220.

Seban, R.A., Behnia, M.M & Abreu, K.E. 1978 Temperatures in a heated air jet discharged downward. *International Journal of Heat Mass Transfer* **21**, 1453–1458.

Send, U. & Marshall, J. 1995 Integral effects of deep convection. *J. Phys. Oceanogr.* **25**, 855–872.

Shabbir, A. & George, W.K. 1994 Turbulent entrainment in jets with arbitrary buoyancy. *Journal of Fluid Mechanics* **275**, 1–32.

Shy, S.S. 1995 Mixing dynamics of jet interaction with a sharp density interface. *Experimental Thermal and Fluid Science* **10**, 355–369.

Song, I-S, Chun, H-Y & Lane, T.P. 2003 Generation mechanisms of convectively forced internal gravity waves and their propagation to the stratosphere. *J. Atmos. Sci.* **60**, 1960–1980.

Stull, R.B. 1976 Internal gravity waves generated by penetrative convection. *J. Atmos. Sci.* **33**, 1279–1286.

Sutherland, B.R., Dalziel, S.B., Hughes, G.O. & Linden, P.F. 1999 Visualization and measurement of internal waves by 'synthetic schlieren'. part 1. vertically oscillating cylinder. *J. Fluid Mech.* **390**, 93–126.

Sutherland, B.R. & Dohan, K. 2004 Internal wave excitation from a collapsing mixed region. *Deep-Sea Research II* **51**, 2889–2904.

Sutherland, B.R. & Linden, P.F. 2002 Internal wave excitation by a vertically oscillating elliptical cylinder. *Physics of Fluids* **14**, 721–731.

Tennekes, H. & Lumley, J.L. 1972 *A first course in turbulence*. The MIT Press.

Timothy, W.K. 1977 Density currents and their applications. *Journal of Hydraulic Division* **103, No. HY5**, 543–555.

Townsend, A.A. 1964 Natural convection in water over an ice surface. *Quart. J. Roy. Met. Soc.* **90**, 248–259.

Townsend, A.A. 1965 Excitation of internal waves by a turbulent boundary layer. *J. Fluid Mech.* **22**, 241–252.

Townsend, A.A. 1966 Internal waves produced by a convective layer. *J. Fluid Mech.* **24**, 307–319.

Tsuda, T., Murayama, Y., Wiryosumarto, H., Harijono, S.W.B. & Kato, S. 1994 Radiosonde observations of equatorial atmosphere dynamics over indonesia, 2, characteristics of gravity waves. *J. Geophys. Res.* **99(D5)**, 10507–10516.

Turner, J.S. 1966 Jets and plumes with negative or reversing buoyancy. *Journal of Fluid Mechanics* **26**, 779–792.

Turner, J.S. 1972 On the energy deficiency in self-preserving convective flows. *J. Fluid Mech.* **53**, 217–226.

Turner, J.S. 1973 *Buoyancy effects in fluids*. Cambridge University Press.

Vincent, R.A. & Alexander, M.J. 2000 Gravity waves in the tropical lower stratosphere: An observational study of seasonal and interannual variability. *J. Geophys. Res.* **105, No. D14**, 17971–17982.

Zatsepin, A.G. & Shapiro, G.I. 1982 A study of axisymmetric intrusions in a stratified fluid. *Izvestiya, Atmosph. and Ocean Phys.* **18**, 77–80.

Zeldovich, Y.B. 1937 The asymptotic laws of freely-ascending convective flows. In *Selected Works of Yakov Borisovich Zeldovich* Vol. 1, 1992 (ed. J.P. Ostriker), pp. 82–85. Princeton University Press.

Zhang, H. 1996 Saline, thermal and thermal-saline buoyant jets. *Ph.D. Thesis, University of Western Ontario, Canada* .